SANDIA REPORT
SAND2016-9520
Unlimited Release
September, 2016

Final Report for LDRD: The Effect of Proppant Placement on Closure of Fractured Shale Gas Wells

Mathew Duffy Ingraham, Dan Bolintineanu, Rekha R. Rao, Lisa A. Mondy, Jeremy B. Lechman, Enrico C. Quintana, Stephen J. Bauer

Prepared by
Sandia National Laboratories
Albuquerque, New Mexico 87185 and Livermore, California 94550

Sandia National Laboratories is a multi-mission laboratory managed and operated by Sandia Corporation, a wholly owned subsidiary of Lockheed Martin Corporation, for the U.S. Department of Energy's National Nuclear Security Administration under contract DE-AC04-94AL85000.

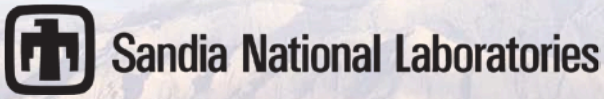

Issued by Sandia National Laboratories, operated for the United States Department of Energy by Sandia Corporation.

Available to DOE and DOE contractors from
U.S. Department of Energy
Office of Scientific and Technical Information
P.O. Box 62
Oak Ridge, TN 37831

Telephone: (865) 576-8401
Facsimile: (865) 576-5728
E-Mail: reports@osti.gov
Online ordering: http://www.osti.gov/scitech

Available to the public from
U.S. Department of Commerce
National Technical Information Service
5301 Shawnee Rd
Alexandria, VA 22312

Telephone: (800) 553-6847
Facsimile: (703) 605-6900
E-Mail: orders@ntis.gov
Online order: http://www.ntis.gov/search

SAND2016-9520
Unlimited Release
September, 2016

Final Report for LDRD: The Effect of Proppant Placement on Closure of Fractured Shale Gas Wells

M.D. Ingraham[1], D. Bolintineau[2], R.R. Rao[2], L.A. Mondy[2], J.B. Lechman[2], E.C. Quintana[3], S.J. Bauer[1]
Geomechanics Department[1], Fluid and Reactive Processes Department[2], X-Ray and NDE Department[3]
Sandia National Laboratories
P.O. Box 5800
Albuquerque, New Mexico 87185-MS1033

Abstract

The recent boom in the oil and natural gas industry of hydraulic fracture of source rocks has caused a new era in oil and gas production worldwide. However, there are many parts of this process that are poorly understood and thus hard to control. One of the few things that can be controlled is the process of injection to create the fractures in the subsurface and the subsequent injection of proppants to maintain the permeability of the fractured formation, allowing hydrocarbons to be extracted. The goal of this work was to better understand the injection process and resulting proppant distribution in the fracture through a combination of lab-scale experiments and computational models.

ACKNOWLEDGMENTS

The authors gratefully acknowledge Norm Warpinski and Jason Maxey of Halliburton Corp for insightful discussions, and supply of friction reducers used in hydraulic fracture. We would also like to thank the technologists of the Geomechanics department (Michael Hileman, Perry Barrow, Michelle Williams) for their assistance in specimen preparation and experimental setup for laboratory tests. Finally, we would like to thank Anne Grillet for her work characterizing the rheology of the guar and the proppant suspensions. The technologists of the X-Ray Non-Destructive Evaluation group, specifically Joe Romero, and Carl Jacques are gratefully acknowledged for their efforts in completing scans.

CONTENTS

FIGURES

TABLES

NOMENCLATURE

AlOx	Aluminum Oxide (alumina)
AM	Additive Manufacturing
CCD	Charge Coupled Device
CT	x-ray Computed Tomography
FEM	Finite Element Model
GPa	Gigapascal
LBB	Ladyzhenskaya-Babuska-Brezzi
LVDT	Linear Variable Differential Transformer
MPa	Megapascal
NMR	Nuclear Magnetic Resonance
NPT	National Pipe Thread
RTV	Room Temperature Vulcanizing
SiC	Silicon Carbide
SNL	Sandia National Laboratories
UV	Ultraviolet

1. INTRODUCTION

In recent years, the United States has become one of the largest producers of oil and natural gas, to the point where the country has become a net exporter of both commodities. This came about as a direct result of horizontal drilling technologies that has allowed direct exploitation of hydrocarbon source rocks (typically organic-rich shales) with large-scale multiple hydraulic fracture processes. This process, while no doubt effective, is poorly understood. Current estimates place recovered shale gas at 20-30% of technically recoverable gas, and shale oil recovery at 3-7 % of recoverable oil (EIA 2015). While these values are lower than we would like, when compared to the estimated total resources they are even worse. The current estimates of produced oil and gas from US shale is 1-3% (EIA 2011).

One reason for this is that production declines from hydraulically fractured wells are drastically lower than conventional wisdom predicts. Traditional reservoirs have highly predictable production declines based on the pore pressure in the reservoir and the time the reservoir has been produced. For shale gas wells, initial production is higher than expected with a much sharper decline, and long, nearly level, production after the initial transient. The reason for this change in decline is unknown, though there is much speculation but no certainty. It has been suggested that this is a result of closure of the hydraulic fractures, or that it is an issue of mass transfer through the shale to the fracture, and the initial production is from gas near the fracture surface, and the low production over time is controlled by diffusion of hydrocarbons through the shale. In either case, fracture closure or diffusion of gas, maintaining an open, highly permeable, fracture network connecting the formation to the borehole is of the utmost importance. Luckily, this is one of the few components of the hydraulic fracture process that we can control either by changing the proppant type or the proppant injection method.

Lab-scale experiments, particle-scale computational simulation, and continuum modeling has been undertaken to investigate how proppant packs inside of a fracture, the distribution within the fracture which helps to maintain permeability, permeability through a proppant pack, and the parameters necessary for hydraulic fracture and injection of proppant.

2. BACKGROUND

The conductivity, which is proportional to the permeability, of geologic fractures has been shown to scale with the cube of the fracture aperture. Models of fracture flow have been developed that can be scaled for surface roughness and can account for obstructions, which are modeled as a "bed of nails" (Walsh, 1981, Gangi, 1978). While these models may be useful, they cannot help us design a fracking and proppant placement process, only estimate the flowrate through the fractures. Therefore, a new approach must be taken including laboratory testing and computational modeling and simulation to extend our fundamental understanding.

Included in this need for further study are investigations into fracture-proppant interactions and their effect on permeability, which has been studied extensively in the field and in the lab. Field studies looking at the effectiveness of different types of proppant at maintaining permeability in a particular well are common, but qualitative, because there is insufficient information about the fate of the proppant to determine quantitative results. Laboratory and computational experiments tend to focus on ideal fractures that are easier to work with in both realms. The problem is that these investigations are oversimplifications of in situ conditions, and therefore provide results that are not as relevant as one would desire.

Field studies of proppant effectiveness usually center on either a particular field, such as the Marcellus shale in Pennsylvania (Arthur et al. 2008), or a particular metric for determining the effectiveness of the propping (Daneshy, 2005). It should also be noted that as time progresses production from subsequent wells in a particular field tends to increase due to improvements in the technology (Baihly et al. 2010). One such improvement is pulsed injection of proppants, which was designed to help improve heterogeneity of proppant distribution in a fracture. Many service companies now perform this type of injection and each have their own name for it. For instance, Schlumberger refers to it as HiWAY (ex. Samuelson et al. 2012, Morris and Chugunov 2014). The idea is that a pulsed injection process will result in a heterogeneous proppant distribution where there are "pillars" of proppant interspersed with open regions. The pillars are strong enough to maintain fracture aperture, while still having open channels for flow to improve the permeability of the formation. While qualitatively this has been shown to increase flow from a reservoir, and idealized lab tests (flow between parallel plates) has shown heterogeneous distributions, what is actually happening to the proppant in the formation is still unknown.

Simulations of proppant placement at the field scale are typically based on continuum-scale particle transport models that break down when particle size is of the same order as the length scale of the flow geometry (crack aperture). Common assumption puts fracture apertures at the borehole at 1-3 proppant particle diameters (hundredths to tenths of an inch), and potentially hundreds of feet long.

Experimentally, there have been a number of investigations into the loss of permeability in fractured shale. The effect of proppant density on host rock embedment was investigated by Wen et al. (2006), who found that, as expected, permeability was heavily dependent on proppant embedment. Proppant embedment in turn was dependent on both proppant density as well as host rock properties. Understanding this, and the closure pressure of the fracture closure over time could be relatively well predicted.

Other investigations have examined proppant density coupled with other effects. Fredd et al (2000), for example, combined shearing of the fractures with an investigation into the effect of proppant density on maintaining permeability. It was determined that the formation properties are increasingly less important as the strength of the proppant increases. It was also found that with sufficient shearing during the fracture process, permeability can be maintained without a large quantity of proppant due to the formation of asperities in the closed fracture after shear offset. It should be noted that stronger proppants in soft hosts still tend towards embedment regardless of the proppant strength.

The stress required to embed proppants and the permeability after embedment has also been examined experimentally (ex. Alramahi and Sundberg, 2012). It is agreed from experimental investigations of embedment that high clay content in the host shale allows for more proppant embedment, but clay type is nearly as important as clay quantity. Other important factors are the porosity of the shale host and its organic content.

3. LABORATORY TESTS

3.1 Materials

Two different materials were used in this study. The first, and most important, was Marcellus shale from an outcrop in West Virginia. The second was Westerly Granite, which was readily available and used to test the experimental approach prior to using shale. This was done because the response and failure of Westerly Granite is well documented and understood. This allowed us to develop a fracking test system and insure it was operating properly before performing tests on shale, since shale samples are much more difficult to obtain and shape.

3.2 Methods

A series of tests were performed for this project. Tests performed will be presented chronologically within this section. In some cases, tests were performed in parallel, in that case the testing that was begun first will be presented first.

3.2.1 Manual Fracture and Flow

The first tests performed were performed on 1-inch diameter by 2-inch-long core plugs. These core plugs were manually fractured subparallel to bedding, and proppant was manually distributed between the faces of the fracture. The samples were then reassembled as shown in Figure 1. After reassembly these samples were heated to 75° C then loaded to in situ conditions of 3000 psi confining, and 4000 psi axial loading. Once at representative in situ conditions, a flow of water was initiated across the sample, flowing from the bottom of the sample to the top, and the permeability of the fracture was measured by recording flowrate as well as upstream and downstream pressure applied to the sample. It was assumed that the permeability measured was the permeability of the fracture because the permeability of the solid shale is orders of magnitude lower than that of the fracture, therefore the shale permeability was negligible.

The measurements for these tests were performed over the period of a day or two in order to ensure that transient effects in the permeability were no longer significant. The specimen was then unloaded and removed from the loading system. It was then CT scanned to investigate the fracture/proppant condition and measure the aperture of the fracture. After scanning the specimen was reloaded and permeability was measured for another few days, this process was repeated three times. Figure 2 shows an example of the CT scan performed on one of these specimens.

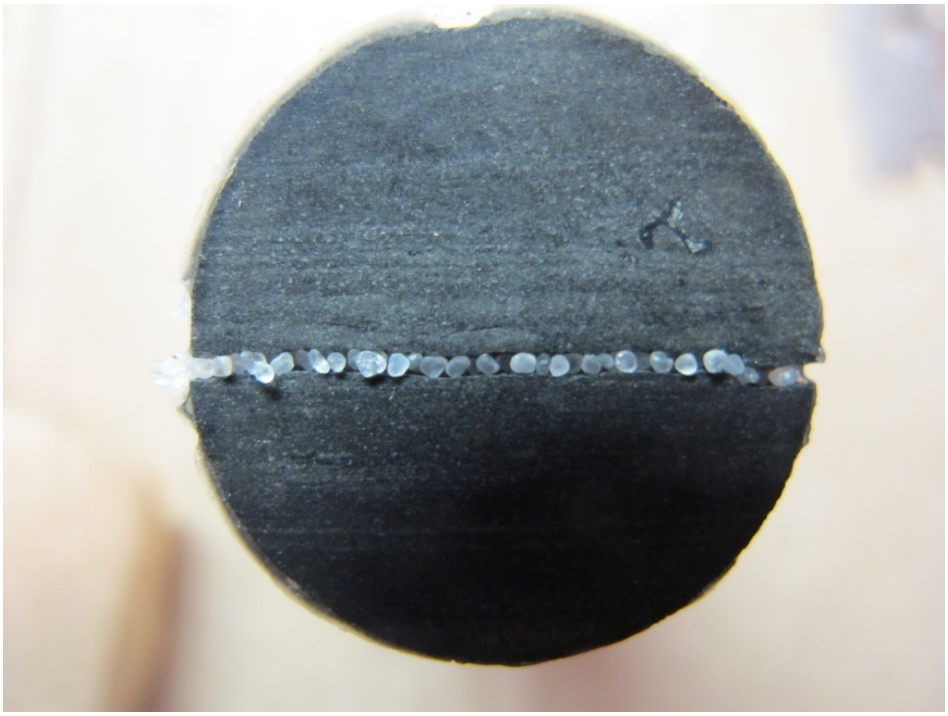

Figure 1. Images of assembled shale sample that was manually fractured.

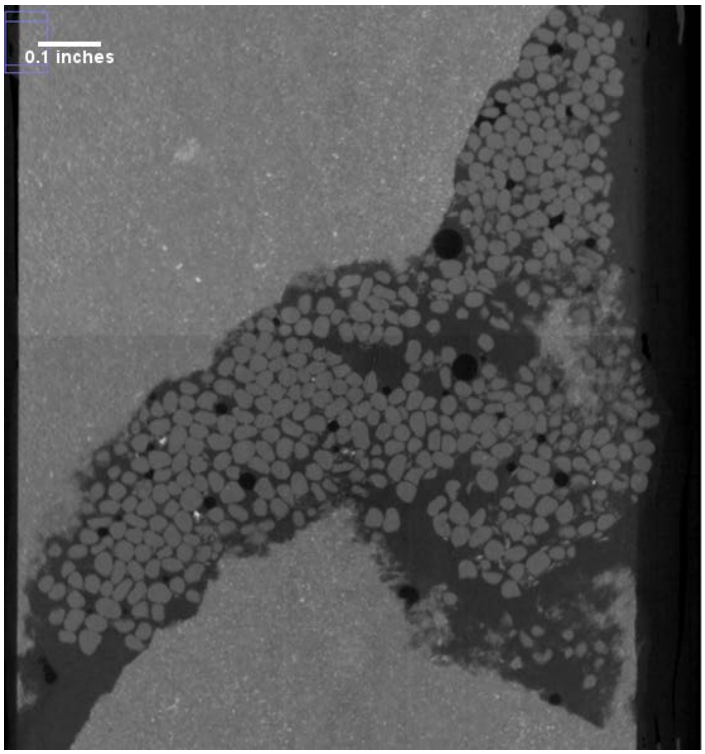

Figure 2. Example of the raw CT scan performed on the specimen. Dark spots are air bubbles

3.2.2 Mechanical Properties of Shale

Mechanical properties of the Mancos shale were determined by performing a pair of unconfined compressive strength tests on core plugs 1 inch in diameter by 2 inches long. Tests were performed according to ASTM C170 with the addition of unload reload loops during testing to determine the mechanical property evolution with loading (specifically Young's modulus and Poisson's ratio). Displacements were measured with both the machine stroke, as well as axial and radial LVDTs mounted on the specimen.

3.2.3 Rheology Measurements

Hydraulic fracturing proppant is a suspension of particles in a complex suspending fluid, which may include viscosity enhancing additives to keep particles in suspension such as polymer and surfactant. Guar is commonly used since it biodegradable and the viscosity of the solution can be broken after proppant placement using an acid solution.

The rheology of the proppant is critical to modeling the flow and transport within the fracture. In the field, fracturing proppant particles consist of sand, bauxite, or ceramic beads with sizes on the order of 0.02-0.08 inches in diameter. The proppant solution is injected through a drill pipe, typically between 3 - 5 inches in diameter depending on the drilling operation. Due to the scale down of both the rock being fractured and the fracturing system, the proppant particles also had to be scaled down. Sand, bauxite and ceramic beads were not available in the desired size, ~0.003 inches, or approximately one order of magnitude lower than proppants used in the field. This value was chosen because the injection line had an inner diameter of 0.125 inches, or approximately one order of magnitude lower than what was used in the field, and still readily available. These particles were smaller than their field-scale equivalent but still large enough that they were not colloidal and hydrodynamic forces dominate. The particles are heavier than the guar solution, so the viscoelastic normal forces and high flow rates are used to keep them from settling out. The density of bauxite is nominally 3.3 g/cm^3, Al_3O_2 is 3.95 g/cm^3.

At the outset of the project, the proppant particles chosen were alumina (AlOx, the microstructure of which is shown in Figure 3), since they were of the highest density, gave the best contrast for x-ray computed tomography, and were readily available. However, it was found that the alumina showed a large increase in the zero shear viscosity for alumina-guar suspensions as shown in Figure 4. Alumina particles are non-spherical and polydisperse having an average particle size of 104.3 µm. The density is assumed to be 3.95 g/cc.

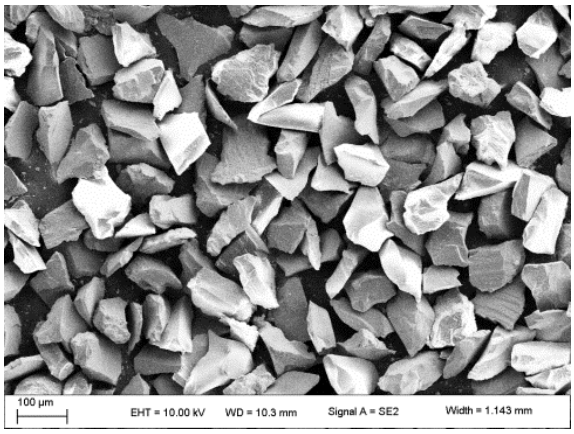

Figure 3. Alumina particles are non-spherical and polydisperse having an average particle size of 104.3 µm. The density is assumed to be 3.95 g/cc

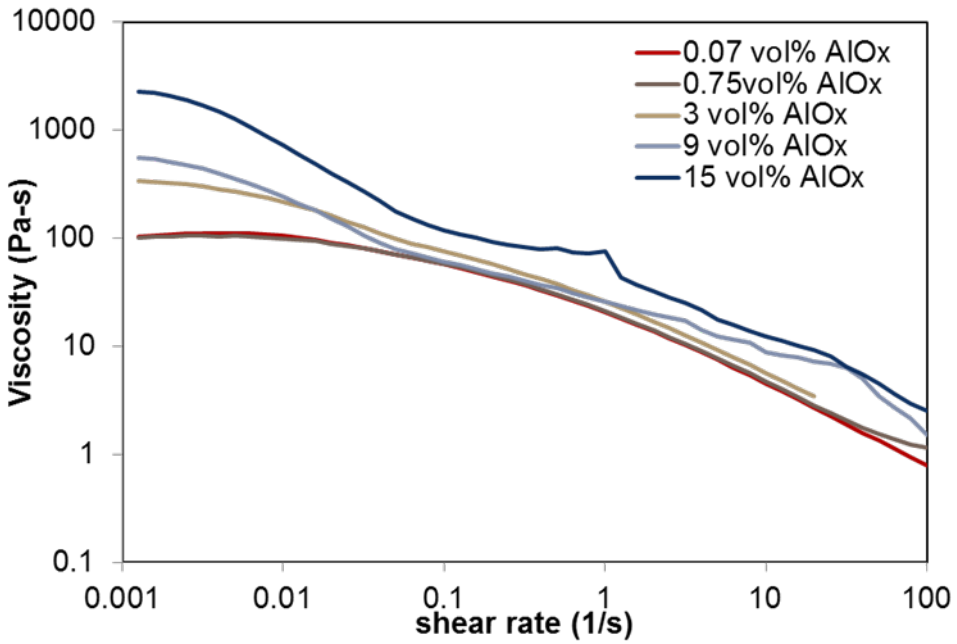

Figure 4. Shear rheology of AlOx suspension showing a dramatic increase in zero-shear rate viscosity even for low solid loading.

The aluminum oxide particles generated strange responses from the guar suspensions. At high AlOx volume fractions, the suspension would start rod climbing during the rheology tests and transient increases in viscosity would occur. We believe this is due to particle bridging increasing the suspension elasticity and causing hydro-clusters to form, which resulted in thixotropy. The alumina-guar interactions significantly modified the rheology, making the suspension significantly more viscoelastic than the suspending fluid, such that it would be difficult to pump without excessive pressures. For this reason, the alumina was replaced with silicon carbide (SiC) particles, shown in Figure 5. The SiC particles are non-spherical and polydisperse having an average particle size of 106.8µm. The density is assumed to be 3.21 g/cc.

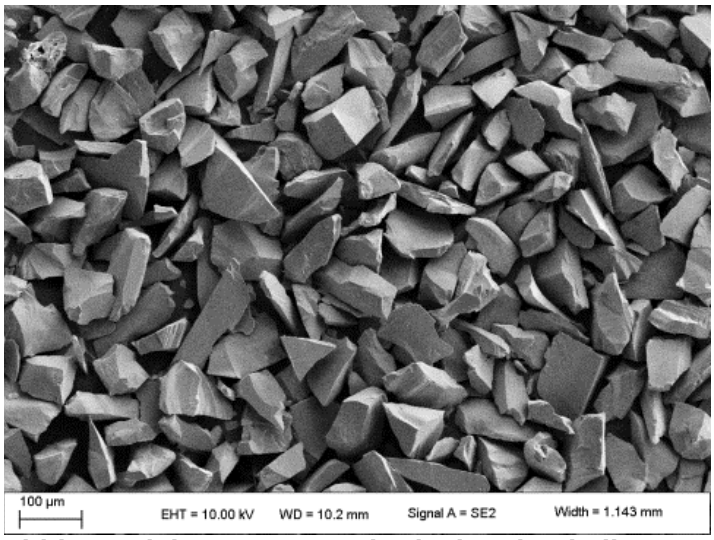

Figure 5. Silicon Carbide particles are non-spherical and polydisperse having an average particle size of 106.8µm. The density is assumed to be 3.21 g/cc.

The neat guar solution was composed of guar gum (1.48 wt%), boric acid (0.10 wt%) isopropanol (0.10 wt%), and water (98.32 wt%). The water, isopropanol, and boric acid were mixed in a small beaker until the boric acid crystals dissolved. Guar gum was then added and the mixture stirred until the mixture had begun to thicken significantly. The particles were then sprinkled on top while continuing to mix the solution.

The guar solution and particle-guar suspension rheology was measured by Anne Gillet. The rheology of the guar solutions were measured in a TA Instruments AR-G2 rheometer equipped with concentric cylinders. Figure 6 shows the results of two frequency sweeps in oscillatory tests, a longer test taking 10,000 s (2.8 hr), and a shorter one taking 300s. There was concern that the solution would begin to breakdown during the time needed to complete the flow experiment. The behavior, even in the long test, is typical of an uncrosslinked polymer, where viscous behavior is dominant at low frequencies, with elastic properties becoming dominant at higher frequencies. The longer test does not show signs of a decrease in average molar mass (an increase in the frequency of the crossover point), indicating that there should be no problem with the solution breaking as long as we completed the experiments within several hours, which all tests were. Figure 7 shows that the viscosity is also shear-rate dependent. However, when held at a constant shear rate of 0.01 s^{-1}, the viscosity remained steady for the duration of the hour-long test.

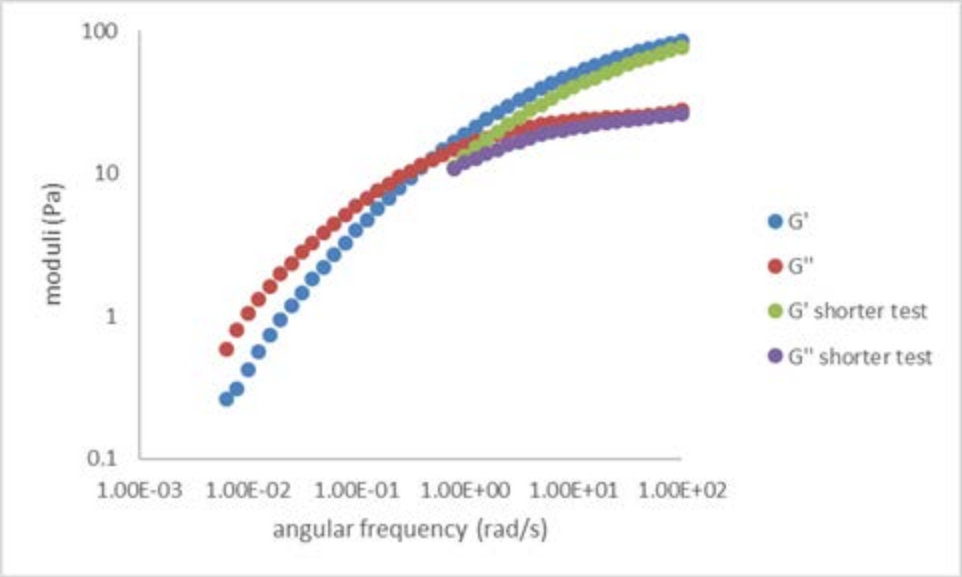

Figure 6. Oscillatory rheology of neat guar solution for two different test times

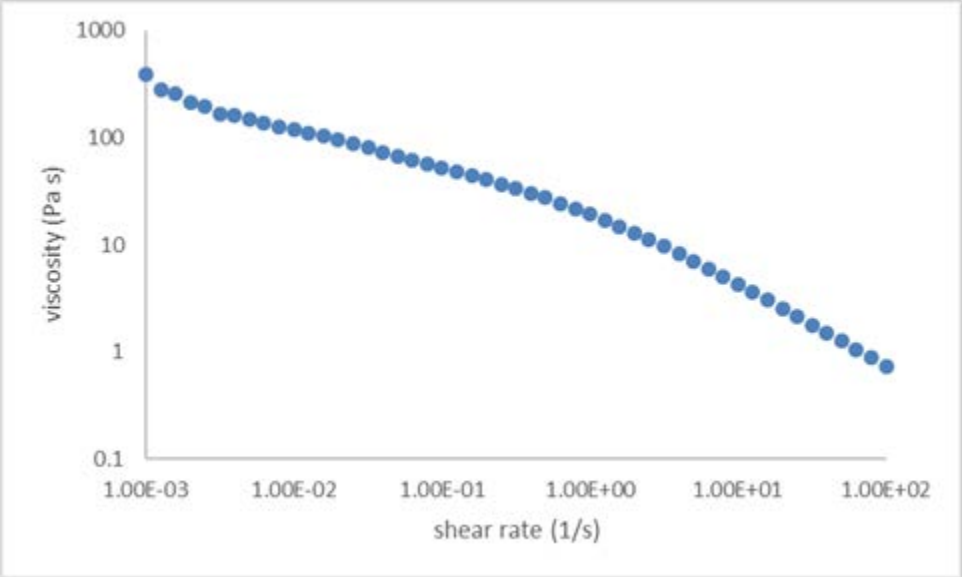

Figure 7. Viscosity as a function of shear-rate for the neat guar solution

Various mixtures of particles in the guar solution were tested in an attempt to determine the effect of the volume fraction of solids on the relative viscosity of the suspension. The viscosity of the suspensions was measured in shear rate sweeps and extrapolated back to a zero-shear rate viscosity. These comparisons showed that a shear rate of 0.001 s^{-1} usually approximated "zero shear" well for the suspensions. Therefore, the relative viscosity was taken as the zero-shear rate viscosity of the suspension normalized by the viscosity of the neat solution at 0.001 s^{-1}. Figure 8 shows the results of the measured relative viscosity for several suspensions. The SiC particles had little effect on the viscosity.

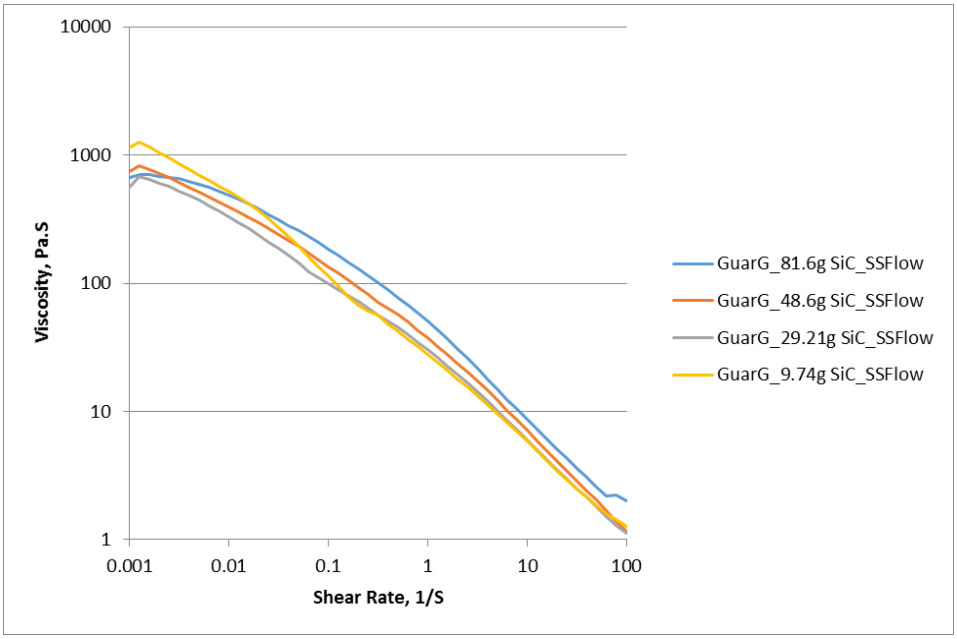

Figure 8. Viscosity response for different concentrations of SiC particles.

3.2.4 Hydraulic Fracture of Granite

Hydraulic fracture tests were performed on Westerly Granite specimens that were 4 inches in diameter and 8 inches long. The specimens had a 0.25-inch hole drilled in the center of the specimen to a depth of 4 inches. A steel pipe was inserted into the hole and glued in place. The pipe had and 0.25-inch outside diameter and a 0.125 inch inside diameter. The bottom 0.5 inches of the 0.25-inch hole was left open to the rock, and part of the pipe was left above the top of the specimen. This was so that the pipe could be sealed to the endcap, such that fluid could be injected into the rock to fracture it. The specimens were then wrapped in a piece of Feltmetal® that was used to allow the fracture fluid to escape the specimen without damaging the specimen jacket. Another piece of Feltmetal® was placed on the bottom of the specimen so the fluid could drain around the bottom of the specimen and flow out through the pressure port on the bottom of the specimen. After the specimen was wrapped in the Feltmetal® it was jacketed in a heat-shrink polyolefin jacket that was sealed to the specimen endcaps with an O-ring and tie wires. Figure 9 shows the test assembly for the specimen.

After assembly, the specimen was loaded into a pressure vessel and the vessel was placed into a loading frame. The specimen was loaded to a hydrostatic pressure of 10.4 MPa and a differential stress of 3.5 MPa. After loading, the injection pressure was increased to 25.9 MPa to fracture the rock. The maximum pump pressure was insufficient to fracture the rock, so the confining pressure was reduced to 6.9 MPa in order to initiate fracture. This resulted in stresses lower than desired to replicate in situ conditions. For subsequent tests (shale fracture tests) a 69 MPa injection pump was used. The fluid injected was first water, then the water was followed by the SiC laden guar mixture.

Figure 9. Westerly granite fracture specimen assembly

3.2.5 Millifluidic Flow Visualization Experiments

Our initial efforts to model suspension flow in the propped fracture led us to realize that the flow rate and the geometry were both poorly characterized. For this reason, three millifluidic transparent flow cells were created to allow for flow visualization and to investigate flow in a test cell with well-characterized geometry and flow rates. The fluids used in these tests were pure water, neat guar solution, and proppant-laden guar solution. In addition, food coloring was added to improve the contrast between the water and the suspension, allowing us to visualize the transition as the proppant mixture displaces the water. The food coloring is added in minute quantities and should not affect the solution rheology. The flow cell geometries were designed on the computer, where the finite element mesh for flow modeling was created at the same time as the solid model for additive manufacturing (AM). The solid model was sent to the Sandia AM laboratory, where it was manufactured with clear UV-cured photopolymers (PolyJet process). The flow cells were designed to be idealized branched fractures with different outlet sizes, a typical computer model for which is shown in Figure 10. The flow comes in a central pipe and then flows out through four different channels, which are designed to be narrow, but wide, ducts that could clog and prop. Each printed flow cell was covered with a 1/8 in piece of Polycarbonate. This was secured with 8 8-32 screws and RTV silicone to seal the cover to the flow cell base. These tests were imaged with both video cameras and CCD cameras that captured images at a given framerate, normally 1 or 2 frames per second.

Tests were performed with an ISCO 500D pump that was connected to the flow cell with a length of 0.25-inch stainless steel tubing with an internal diameter of 0.125 inches. This was connected to the flow cell with a $1/8^{th}$ inch NPT fitting, the flow cell was tapped for the $1/8^{th}$ NPT after it was assembled, so the threads were cut into both the flow cell and the Lexan cover plate. Fluids were typically injected at a constant flow rate of 10 ml/min. Although during early

testing these parameters were varied to determine appropriate pressures and flow rates to perform the tests.

Tests were run to either fill the space, or to displace previously existing fluids within the flow cell. In either case, the test was run until the operator determined that enough fluid had been pumped through the cell to provide sufficient data to validate the model. During some tests, the effluent was collected and periodically weighed in order to determine a time averaged flowrate for each channel. In this case, the tests were run for longer periods of time to ensure that transients in the initial flow did not skew the results.

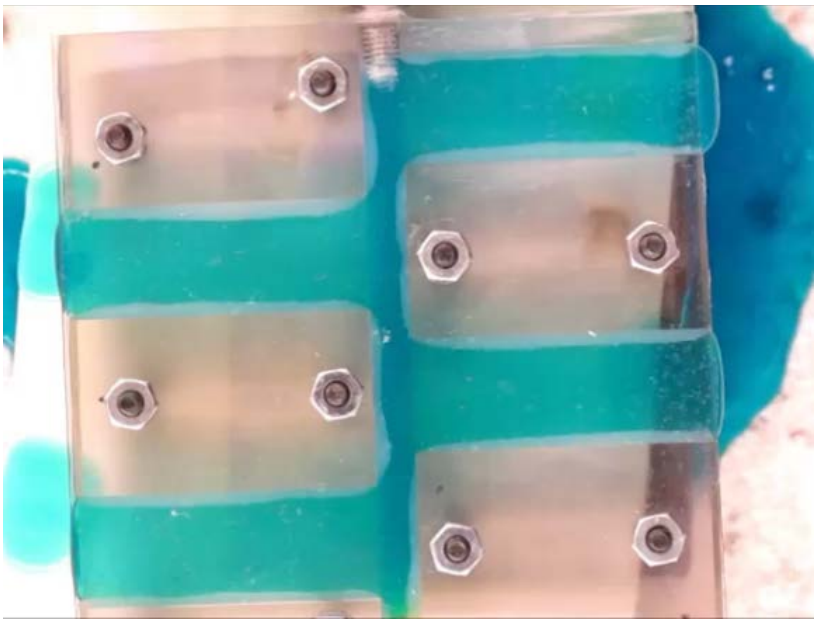

Figure 10. The millifluidic flow channel, designed for flow visualization, is first filled with blue water to improve contrast with the proppant solution. The flow comes in the fro the top of the figure and goes out the four thin channels, designed to mimic branching fractures.

3.2.6 Hydraulic Fracture of Shale

Shale specimens were fractured and prepared in the same manner as the Westerly Granite specimens, with minor modifications. The most noteworthy change is the specimen size. Marcellus Shale samples were cored at 3 inches in diameter and approximately 6 inches long. The smaller size was used because it was not possible to core 4 inch samples 8 inches long from the parent blocks of shale that were supplied by colleagues at National Energy Technology Laboratories (NETL). Thus the hole drilled into the specimen was drilled to 3 inches deep, instead of 4 inches for the granite. The steel pipe epoxied into the specimen was slightly shorter because of this, but was glued into place in the same manner. The specimen was then wrapped in Feltmetal and sealed with O-rings and polyolefin. For these specimens, the silicon carbide proppant was used since this had better rheology when combined with the guar solution. The shale test that generated a properly oriented fracture, the axial stress was 2 MPa, with a confining pressure of 6.9 MPa. The injection pressure was still 25.9 MPa.

3.3 Results and Discussion

3.3.1 Manual Fracture and Flow

The results of the manual fracture and flow tests are well summarized in the published paper by Ingraham et al. (2015), which was presented at the American Rock Mechanics Association Meeting and is included in Appendix 1. However, a brief summary will be presented here for reader convenience.

It was observed that there was a notable decrease in permeability with time, as the specimens were held at a constant load and temperature. The observed causes for this decrease in permeability were numerous. Fracture closure was one cause, and was effected by both proppant embedment in the shale host as well as deformation/fracture of the proppant particles. From X-ray CT, it was seen that the fractured proppants were not isolated, but were found in the middle of a proppant pillar, indicating that proppant failure can occur even in a stable, well-sorted, proppant pack.

Permeability was also affected by spalling of the fracture walls. The spalling of the shale coupled with the flow through the fracture caused rock fragments of both shale and quartz proppant to be transported within the proppant pack. These fragments often became trapped in the proppant pillars and partially blocked potential flow paths. Over a 60-day period of loading and unload (so the specimen could be removed for CT scanning), it was found that the permeability of the fracture decreased an order of magnitude. An image of the specimen showing the transported shale flakes is presented in Figure 11.

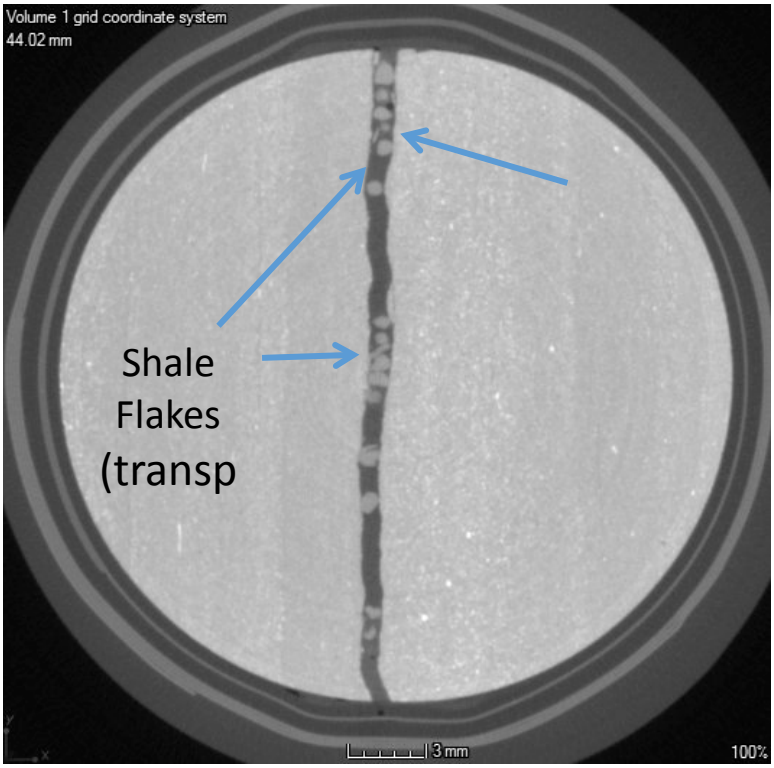

Figure 11. CT scan of manually fractured specimen with spalled shale flakes indicated.

3.3.2 Mechanical Properties of Shale

The response of the Marcellus shale used for hydraulic fracture testing is shown in Figure 12. It is evident from this plot that the response parallel to bedding is much stiffer than when loaded perpendicular to bedding, however it failed at a much lower peak stress. Both loading directions showed a softening of the modulus as the test progressed. The average Young's modulus, determined from unload reload loops, for the bedding parallel to the loading direction was determined to be 11.6 GPa, while the average for loading perpendicular to bedding was 8.5 GPa. Poisson's ratio parallel to bedding was found to be 0.36, while poisons ratio perpendicular to bedding was 0.24.

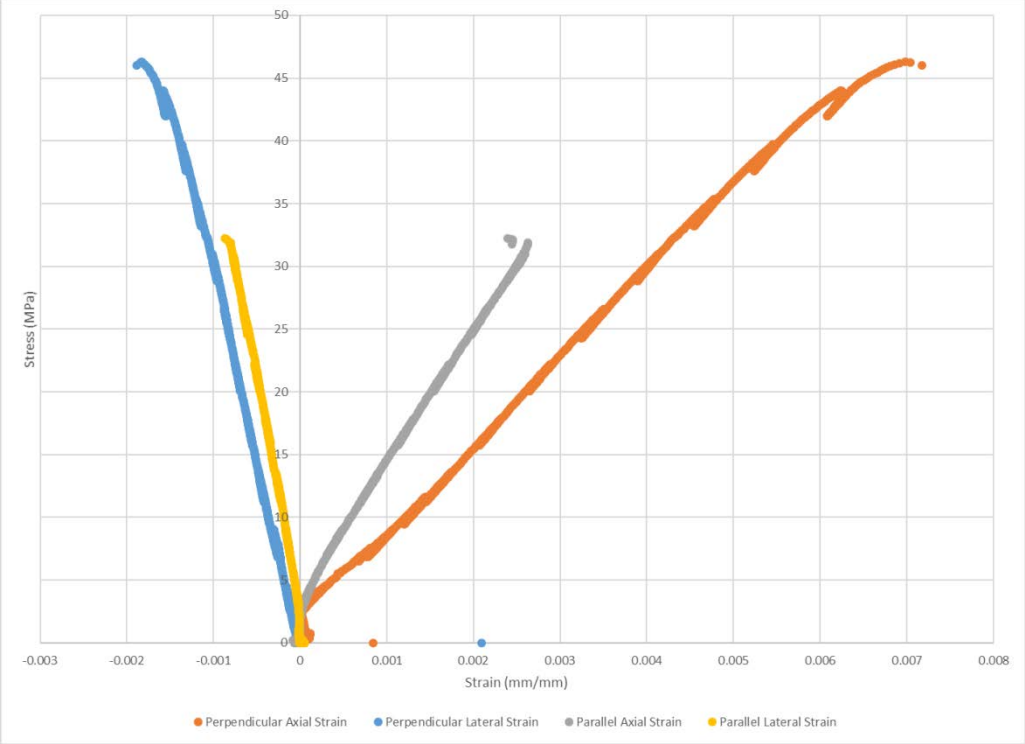

Figure 12. Mechanical response of Marcellus shale under uniaxial compression, for specimens loaded both parallel and perpendicular to bedding.

3.3.3 Hydraulic Fracture of Granite

Hydraulic fracture of the Westerly Granite specimens was performed under axisymmetric compression conditions, meaning that the fracture formation was oriented parallel to the borehole. Tests were performed in this orientation as a means of testing the experimental setup and to ensure that fractures could be formed before testing proceeded with the more expensive/difficult to machine shale specimens. Figure 13 shows the loading, injection pressure, and flowrate curves for a typical test.

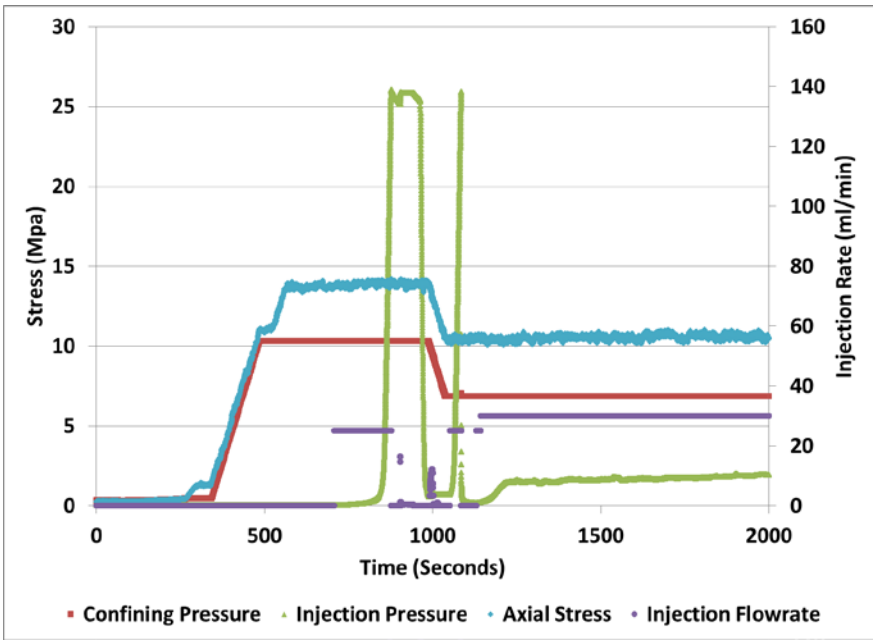

Figure 13. Results from a typical granite fracture test showing confining pressure, injection pressure, axial stress and injection flow rate.

This does not mimic the typical hydraulic fracture test observed in field testing because it is an open system, since once the specimen has fractured the injected fluid is free to leave the system through the frit material wrapped around the specimen. This was done to allow for injection of more proppant laden fluid. As a result, the shut in pressure (when pumping is stopped), drops to nearly zero because of injected proppant and shear offset in the fracture maintaining a relatively high level of permeability in the fracture; allowing fluid in the fracture to drain to atmosphere. This also means that the typical measurements of opening pressure, and shut in pressure cannot be made with this specimen configuration. But it makes it much easier to examine proppant motion because of the excess fluid that can be injected, meaning that this is a relatively good model of what occurs close to the borehole in a field fracture process.

Fractures, as predicted, were oriented axially along the borehole and protruded a few millimeters below the bottom of the borehole, meaning that the lower half of the specimen was still largely intact, with the fracture plane running through the borehole. Figure 14 shows a slice of a CT scan showing the entire specimen at a relatively coarse resolution. At this resolution the crack is readily visible, but nothing can be discerned within the fracture. A number of techniques were used to try to increase the resolution of the proppant pack within the specimen. However, they were unsuccessful in resolving individual particles when the whole specimen was scanned. Therefore, we resorted to subcoring the specimen to give us a smaller sample size. In order to subcore the sample, we had to epoxy impregnate propped fracture so that the microstructure would be undisturbed during the coring process. The subcore was 0.5 inch in diameter and approximately 2 inches long, which allowed for scans at the desired resolution. Figure 15 shows a full 3D render of a scan performed on one of the subcores, the islands of proppant can clearly be seen as the orange particles in the purple fracture. A slice of this image is shown in Figure 16 where the proppant and the channels can be clearly seen in the crack region.

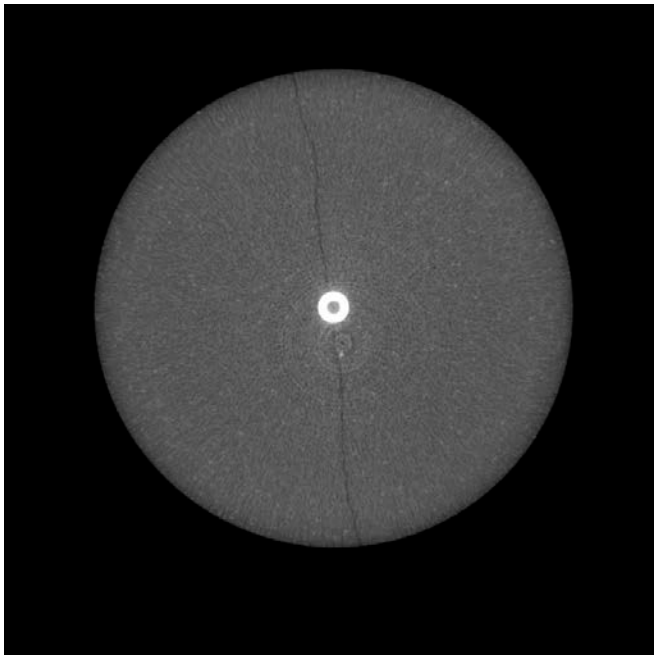

Figure 14. CT scan image of fractured borehole, the white region is the steel tube in the specimen used to inject fluid with.

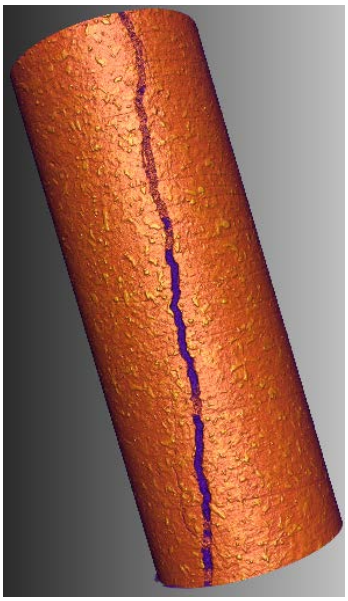

Figure 15. 3D render of a CT scan of a subcored piece of the propped granite.

These results suggest that proppant density in the field may be lower because in laboratory tests fractures were over packed by allowing fluids to drain from the fractures. This suggests that the heterogeneous ~3 layer proppant packs seen in Figure 16 which were typical of this work, contain more proppant than would be seen in a field system. In the field there is no open drain for fluids, meaning that while there is water loss to the surrounding rock, hydraulic fractures in the field are much closer to a closed system than what was tested herein. This also shows that a homogeneous injection process results in a heterogeneous proppant pack.

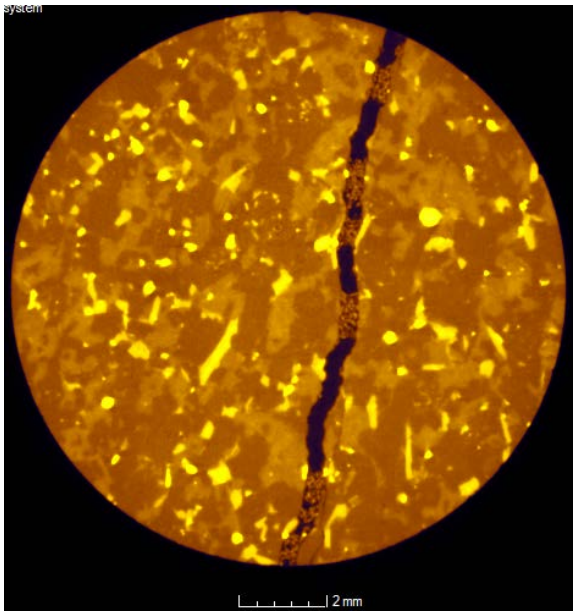

Figure 16. A slice of a CT scan of a granite subcore, islands of proppant and channels for open flow are clearly visible.

3.3.4 Hydraulic Fracture of Shale

Shale experiments were largely similar to the granite tests with the exceptions noted in the methods section, those being an extensile stress state instead of a compressive one, and a smaller specimen necessitated by the fragility of the shale. Initial tests were performed to determine if it was possible to cause the specimen to fracture in the desired orientation. These tests were performed with the lower pressure injection pumps at 25.9 MPa. This was done because of the larger volume that can be delivered with the ISCO 500 D pump vs the 100DM pump (69 MPa max pressure). As seen in Figure 17, it was necessary to decrease both the axial (necessary for the extensile state of stress) and the confining pressure (to lower the failure stress) in order to fracture the specimen with the 25.9MPa that the 500D pump could supply.

As seen in Figure 17, once the desired stress state was reached the injection pressure was increased the maximum the pump could supply, because this was insufficient to fracture the rock, the confining pressure was reduced in steps of approximately 7 MPa, first to 14, then to 6.9 MPa, at 6.9 MPa there were a series of small pressure drops which are interpreted as the fracture propagating. The large pressure drop is the fracture becoming through going, and this is confirmed by an increase in axial load due to the pressure on fracture surfaces generating an additional axial load in the sample.

Injection continued at a constant flowrate of 20 ml/min, which caused the pressure to increase, presumably because of clogging of the mesh frit and the fracture space with transported shale particles because there was no proppant in the injected fluid at this time, this fracture was generated with clean water. As the pressure peaked, the control mode was switched from constant flow to constant pressure at the maximum pump pressure of 25.9 MPa. This caused the observed spike and decrease in flowrate around 4000 seconds into the test. This was allowed to continue for a few minutes then the test was shut down by decreasing the injection pressure, the releasing confining and axial stresses.

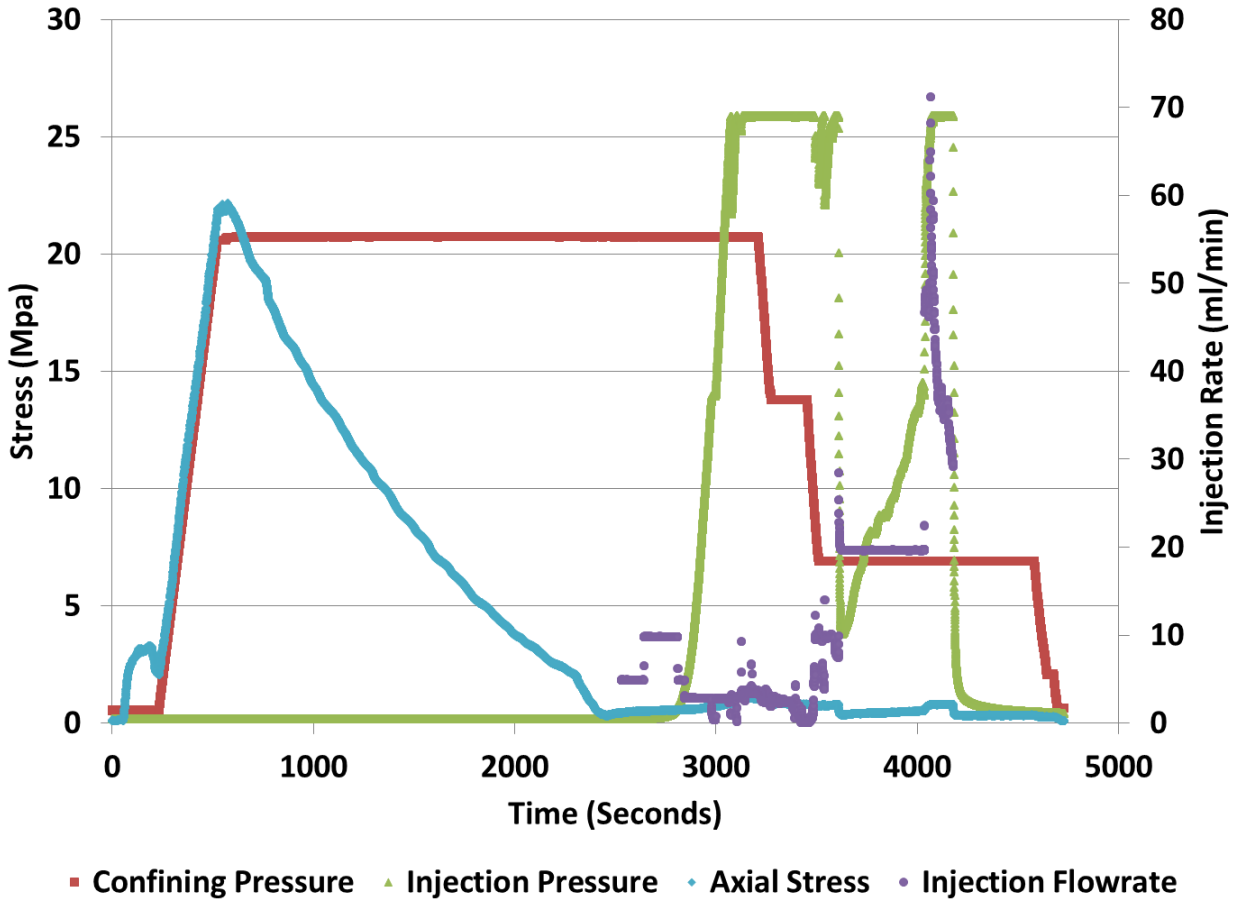

Figure 17: Plot of applied pressures and flowrate for the shale fracture test.

Although these tests did not have proppant injected, they showed very promising results. It was shown that it was possible to generate fractures that were normal to the borehole, in a specimen that was cored parallel to bedding, a result that was not found in an extensive literature search. It was observed, as seen in Figure 18, that the fracture had minimal interaction with preexisting fractures or the bedding plane. The primary fracture seen in the middle of the specimen showed little influence from the preexisting fractures, seen as shadows on the scan, most easily seen in the top left corner of the specimen, nor from bedding, which cannot be discerned on this scan, but would have caused vertical excursions of the fracture path.

Figure 19, below, shows the specimen after removal of the jacket. The generated fracture is shown by the red arrow. The darker lines on the specimen are preexisting/healed fractures, with a higher permeability than the host rock. This is apparent because they are holding/transporting the water used for fracturing. Banding on the surface of the specimen perpendicular to the coring direction is due to the coring process, not bedding, the specimen was cored parallel to bedding.

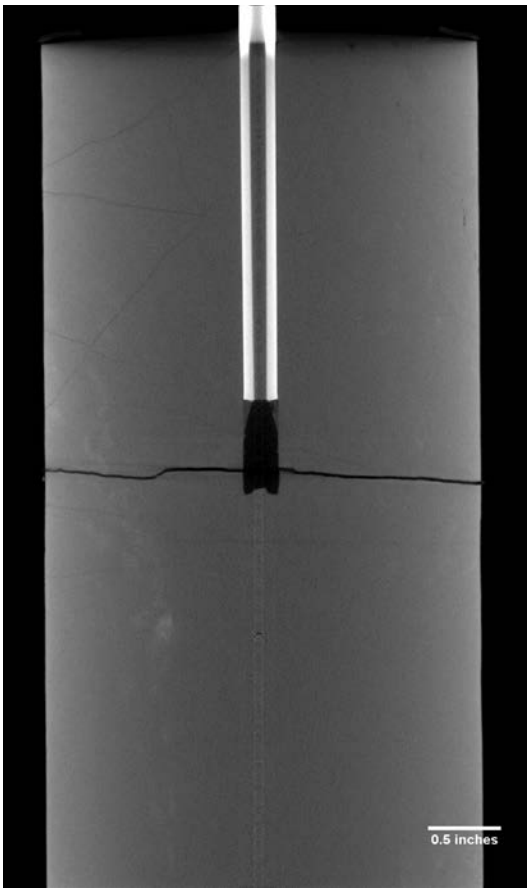

Figure 18: CT scan of the fractured Marcellus shale specimen, note the lack of interaction with preexisting fractures.

Further testing of the shale specimens was delayed to the point of incompletion due to sealing problems between both the specimen and the injection pipe, and between the injection pipe and the end cap. Initially a leak formed through the epoxy that was used to hold the pipe into the hole in the specimen. That problem was solved with a higher strength epoxy in subsequent specimens, however it became apparent that the seal between the pipe and the end cap could not withstand more than approximately 38 MPa, which resulted in failure of all of the tests that were being performed with injection pressures of approximately 69 MPa. Due to the timing of this in the project and the funds used to diagnose the problem, there was insufficient funding to have the parts remanufactured with different seals to complete testing.

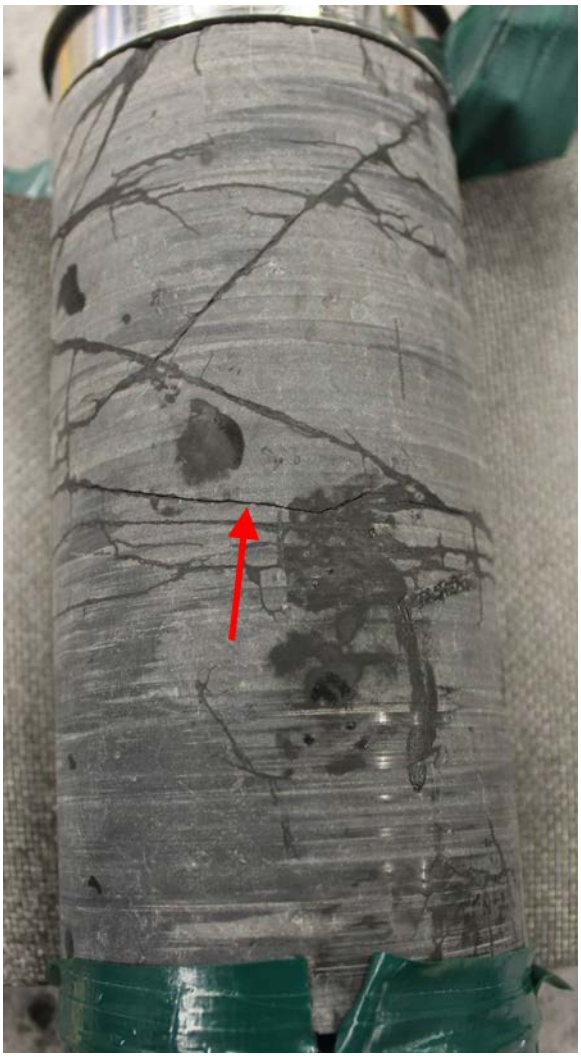

Figure 19: Fractured shale sample, not the arrow pointing at the fracture, the other lines on the sample are preexisting fractures.

4. NUMERIC EXPERIMENTS

The placement of solid proppant materials by gelling fracturing fluids is a process that is critical to stimulation of gas and oil wells in shale formations, but is not readily predicted for a variety of reasons, the foremost of which is uncertainty in the description of the solids transport. Additional complexity arises from the fact that the fracturing fluids have time- and temperature-dependent rheology, since they gel during the injection process and are subsequently broken down by chemical processes in order to flush the resulting propped fracture to leave a high conductivity path. The key capability needed is fully three-dimensional modeling of proppant transport by time- and temperature-dependent viscoelastic fluids, including the effects of convection and leak off of the fracturing fluid into the formation. Initial work to develop such a model is described here. We limit this initial modeling work to the transport of non-neutrally buoyant particles in viscous liquids through narrow, branching channels, the geometry chosen to idealize flow in a fracture. The suspension is approximated using a continuum approach. The model results are compared to a more realistic proppant system in a guar gum solution, in order to see if the model can capture key features of the flow despite simplifying assumptions made. The validation experiments and the materials used are discussed first, and the model description and comparisons follow.

4.1 Modeling Millifluidic Flow Cell

As discussed in the experimental section (section #3.2.5 Millifluidic Flow Visualization Experiments), millifluidic experiments were designed to help elucidate the flow of proppant-guar suspensions into idealized fractures. Figure 20 shows a schematic of the channel, consisting of a main channel, the inflow of which is on the left, and four branches, offset from each other, that each terminate in an outflow. The far end of the main channel from the inflow is sealed, forcing the flow to fill and exit the channels.

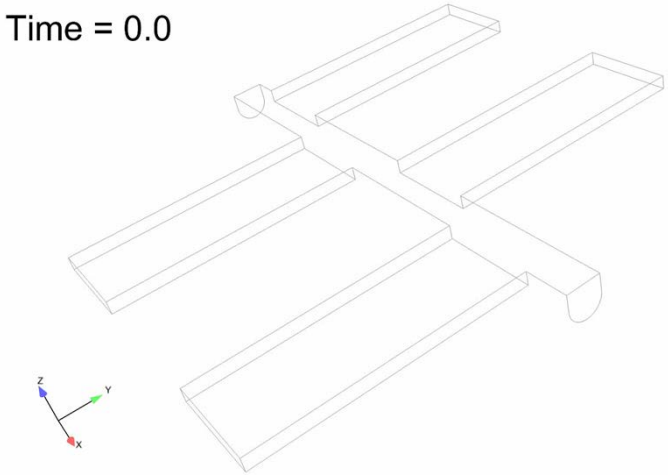

Figure 20. Geometry of millifluidic device showing its branched structure.

The fixture is initially filled with neat guar solution that has been dyed blue for contrast with the dyed yellow suspension that is later injected. The displacement of the neat material with the

"proppant" suspension is recorded with time-stamped video. Results will be shown in a later subsection.

4.1.1 Model description

The flow of a proppant system through branching, narrow channels can cause the solid particles to demix, resulting in large viscosity gradients that influence the flow. The open-source computer code developed at Sandia, GOMA (Schunk et al. 2013), is ideal for continuum-level finite element method (FEM) simulations of filler particle redistribution during flows of non-neutrally buoyant particles. The code allows nonisothermal and reacting flows, and has a variety of rheological models (Rao et al. 2002a, Rao et al. 2002b, Mondy et al. 2011, Grillet et al. 2009). In this work we examine the injection of a proppant-filled liquid into a previously liquid-filled fracture system.

4.1.2 Governing equations

The suspended particles are tracked through a concentration equation, allowing variable density and properties to exist in the domain. The equations for conservation of mass and momentum for low Re, isothermal flows with a variable density are solved:

$$\rho\frac{\partial v}{\partial t}+\rho\boldsymbol{v}\bullet\nabla\boldsymbol{v}+\nabla p-\nabla\bullet\left(\eta\left(\nabla\boldsymbol{v}+\nabla\boldsymbol{v}^{T}\right)\right)-\left(\rho_{f}-\rho_{s}\right)\phi g=0 \qquad \textbf{1}$$

$$\nabla\bullet\boldsymbol{v}=\frac{\left(\rho_{f}-\rho_{s}\right)}{\rho_{s}\rho_{f}}\nabla\bullet J \qquad \textbf{2}$$

Here the density of the fluid is designated ρ_f and that of the solid ρ_s. The overall mixture density, ρ, therefore is:

$$\rho=\left(1-\phi\right)\rho_{f}+\phi\rho_{s} \quad , \qquad \textbf{3}$$

where ϕ is the volume fractions of the solids. In the above equations $\boldsymbol{v}$ is the mass-averaged velocity, p the pressure, η the apparent viscosity of the mixture, and g the gravitational constant. The particles and suspending fluid have different densities, so the velocity field is no longer solenoidal, which introduces the particle flux $\boldsymbol{J}$ into equation 2. Letting $\dot{\gamma}$ be the magnitude of the shear-rate tensor,

$$\dot{\gamma}=\sqrt{\frac{1}{2}\left(\underset{\sim}{\dot{\gamma}}:\underset{\sim}{\dot{\gamma}}\right)} \quad \text{and} \quad \underset{\sim}{\dot{\gamma}}=\left(\nabla\boldsymbol{v}+\left(\nabla\boldsymbol{v}\right)^{\mathrm{T}}\right) \quad , \qquad \textbf{4}$$

we then can write:

$$\frac{J_{s}}{\rho_{s}}=-\left(\phi K_{c}\nabla\left(\dot{\gamma}\phi\right)+\phi^{2}\dot{\gamma}K_{\eta}\nabla\left(\ln\eta\right)\right)+f_{hindered}v_{stokes}\phi \qquad \textbf{5}$$

as derived by Phillips et al (1994) and amended for non-neutrally buoyant particles by Zhang and Acrivos (1994) and Rao et al. (2002a). The last term of equation 5 approximates the hindered settling of a suspension, which is just the Stokes' velocity of a single particle multiplied by a function of the volume fraction giving a value of less than one (2002a):

$$f_{hindered} = \frac{\eta_0 (1-\varphi)}{\eta} \quad , \qquad 6$$

where η_0 is the viscosity of the suspending liquid. The Stokes' settling velocity is defined as.

$$\boldsymbol{v}_{Stokes} = \frac{2}{9}\frac{a^2(\rho_f - \rho_s)\boldsymbol{g}}{\eta_0} \qquad 7$$

K_c and K_η are parameters that scale as the particle radius squared, a^2. We use values similar to those described by Tetlow et. al (1998):

$$K_c = \phi K_\eta \qquad K_\eta = 0.62a^2 \qquad 8$$

Finally, we relate the viscosity of the mixture to that of the suspending fluid, assuming that the particles only increase the apparent viscosity through a function of the local volume fraction and the volume fraction at maximum packing ϕ_m and a fitting exponent -q.

$$\eta = \eta_0 \left(1 - \frac{\phi}{\phi_m}\right)^{-q} \qquad 9$$

As in earlier work (Rao et al. 2002a) we use the values ϕ_m=0.68 and q=1.82. Because of the low $\phi^{initial}$ and the small amount of particle migration expected, no attempt to better fit the rheology data was taken.

Note that the hindered settling function obtains a volume fraction dependence from both the viscosity term in the denominator and the explicit volume fraction term in the numerator. Thus it ends up being similar to the well-known Richard-Zaki correlation but has a better behavior near maximum packing.

4.1.3 Mesh and boundary conditions

The mesh for the flow channel is composed of eight-node hexahedral elements (Figure 21). Gravity is in the negative z-direction. Fluid comes in from the left and flows out the ends of the branch channels. The end of the main channel opposite the inlet is given a no-flow boundary condition (BC). Because the fluid has a variable a variable density, special outflow boundary condition was needed on the pressure at the outlets of the channels. The inflow was set to a plug velocity profile in the x-direction, which then developed into a parabolic flow profiles. All variables use bilinear basis functions and Dohrmann-Bochev stabilization is used to circumvent the LBB condition.

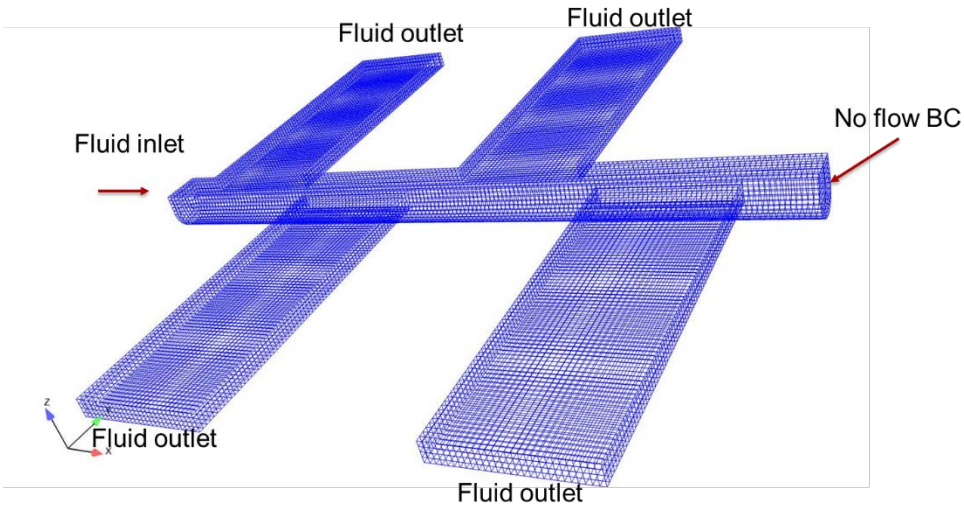

Figure 21. Finite element mesh

4.1.4 Model results compared to experiments and discussion

The initial condition of the model was a channel filled with the suspending fluid. The first simulation used a Newtonian representation of the solution with a constant η =157 Pa s. A second fluid consisting of the same Newtonian suspending fluid but with an initial volume fraction of solids equal to 0.03 is injected at a flow rate of 10ml/min, which corresponds to a linear velocity of 0.46 cm/s starting at time = 0. This suspension then displaces the neat guar over time. Figure 22 shows the results of the model compared to photographs of the experiment over the first 60s. The actual times of the experiment are in white lettering in the bottom right corner of each photograph. The times that the simulation represents are in black lettering above each simulation snapshot. The results are quite similar, despite the simplification of the rheology model.

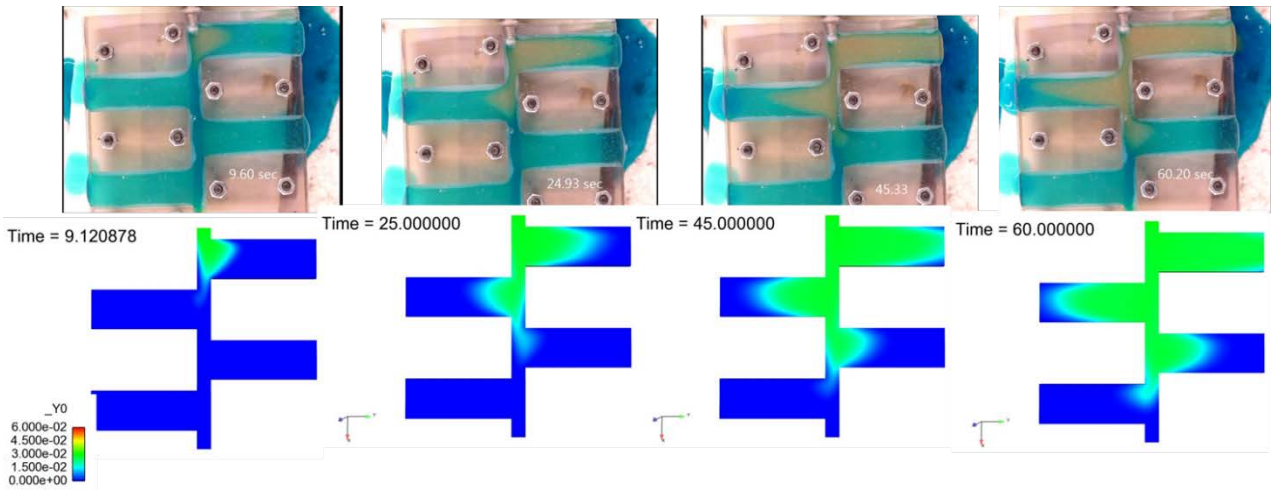

Figure 22. Flow of suspension of "proppant" into channel during the first 60s compared to predictions with a Newtonian suspending liquid.

Figure 23 shows the experimental results compared with the simulation results for times between 90 and 180 s. Here one can see that the simulation begins to somewhat over predict the extent of the penetration of the suspension into the channels. Also, more of the neat fluid remains near the bounding walls in the actual experiment. The discrepancy of the model may be due to the shear-thinning and viscoelasticity of the guar solution, something which is not currently included in the modeling effort. However, again, the qualitative results are reasonable.

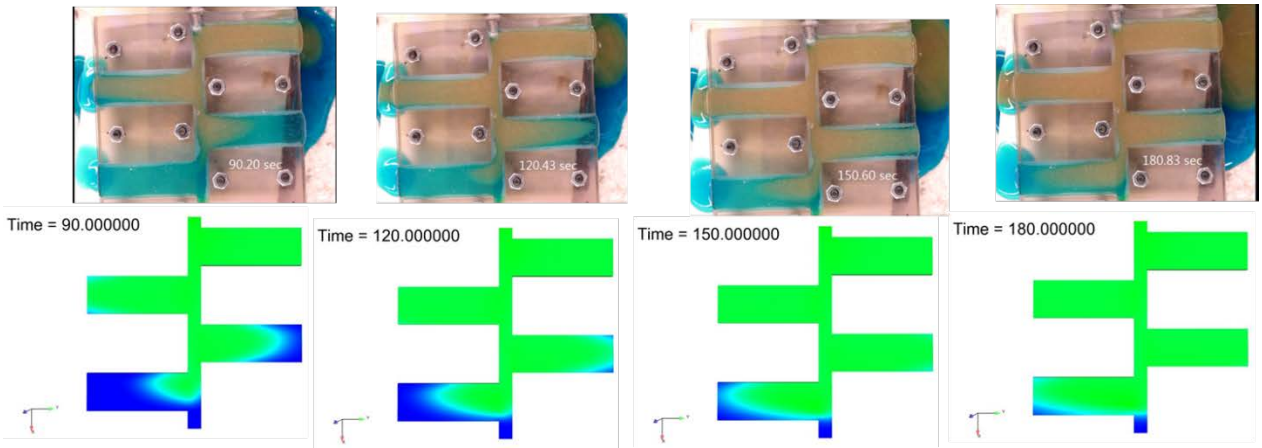

Figure 23. Flow of suspension of "proppant" into channel from about 90 to 180 s compared to predictions with a Newtonian suspending liquid.

The above figures do not show the settling of the particles. The viscoelasticity of the guar solution is designed to keep the particles in suspension. The use of the Newtonian suspending liquid allows more sedimentation, as shown in Figure 24. The sedimentation is not uniform because of the influence of the flow field. This shows the value of validated three-dimensional computational modeling if one needs to predict the placement of proppant. Unfortunately, the current experiments did not lend themselves to determining real-time values of sedimentation. In future experiments, we hope to have multiple camera views so we can see if sedimentation is occurring. In addition, we would like to have higher concentrations of proppant for the suspension to exhibit more non-Newtonian effects.

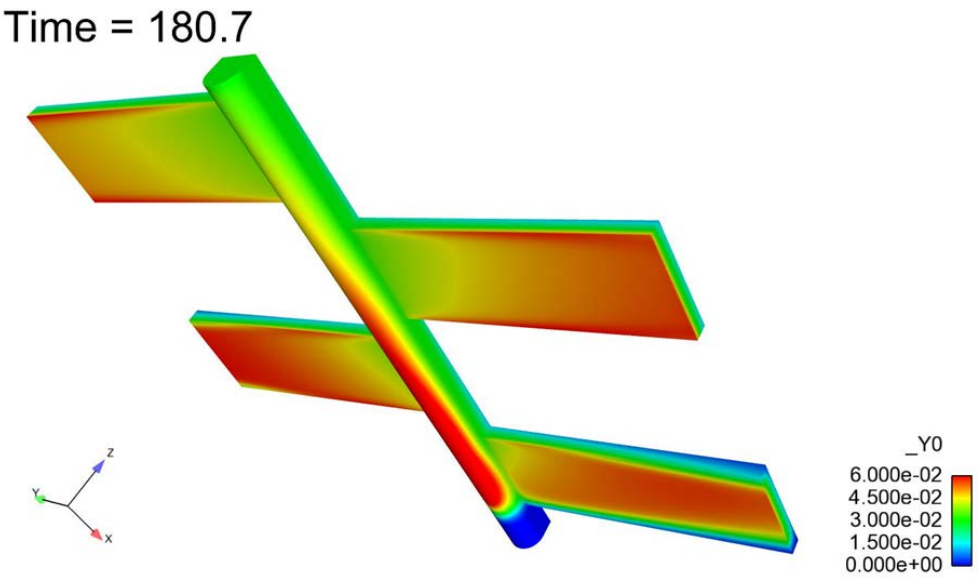

Figure 24. Looking at the bottom of the simulated channel, on can see that particle settling occurs resulting in concentration gradients.

The simulations were repeated using a model with a viscoelastic velocity field but no extra normal stress in the suspension equation. The amount of elasticity was low enough that it did not change the results substantively and they were essentially indistinguishable from those shown above.

4.1.5 Model results for SiC proppant in redesigned millifluidic device with tapered outflows compared to experiments and discussion

From our initial millifluidic experiment modeled in the previous section, we found that the clear molds made from 3D printing were inexpensive and useful for flow visualization, since they are clear and the proppant-guar interface can be easily tracked. The first device used a 3vol% solution of AlOx particles and never formed jammed particle regions or "packed". For our next experiment, we tried reducing the size of channel outflows to be smaller in some cases than the size of the particles. We then ran this new device using a higher concentration and a better behaved proppant: SiC at 10vol%.

As before, the initial condition of the model was a channel filled with the guar suspending fluid. The simulations used a Newtonian representation of the solution with a constant η =39 Pa s, since there was some uncertainty as the best value to use, especially given that the guar is actually shear thinning and may have a yield stress. (Note a viscosity of 157 Pa-s was run as well and give identical velocity and proppant profiles since the viscosity just changes the scale of the pressure.) A second fluid consisting of the same Newtonian suspending fluid but with an initial volume fraction of solids equal to 0.10 is injected at a flow rate of 10ml/min. This suspension then displaces the neat guar over time. Figure 25 shows the results of the model compared to photographs of the experiment over the first 30s. The times that the simulation represents are in black lettering above each simulation snapshot. The results are quite similar, despite the simplification of the rheology model. We are getting some substantial differences between the

model and the experiment. In the model, more of the proppant goes out the first channel than goes straight through the core. Thus at 30s, no proppant has reached the last branch in the model, though some has reached this point in the experiment. We hypothesize that this may be a result of the normal stresses from viscoelasticity of the guar solution resisting exiting the device at the first channel and instead going straight. For future work, we will investigate the effects of viscoelasticity for the millifluidic device.

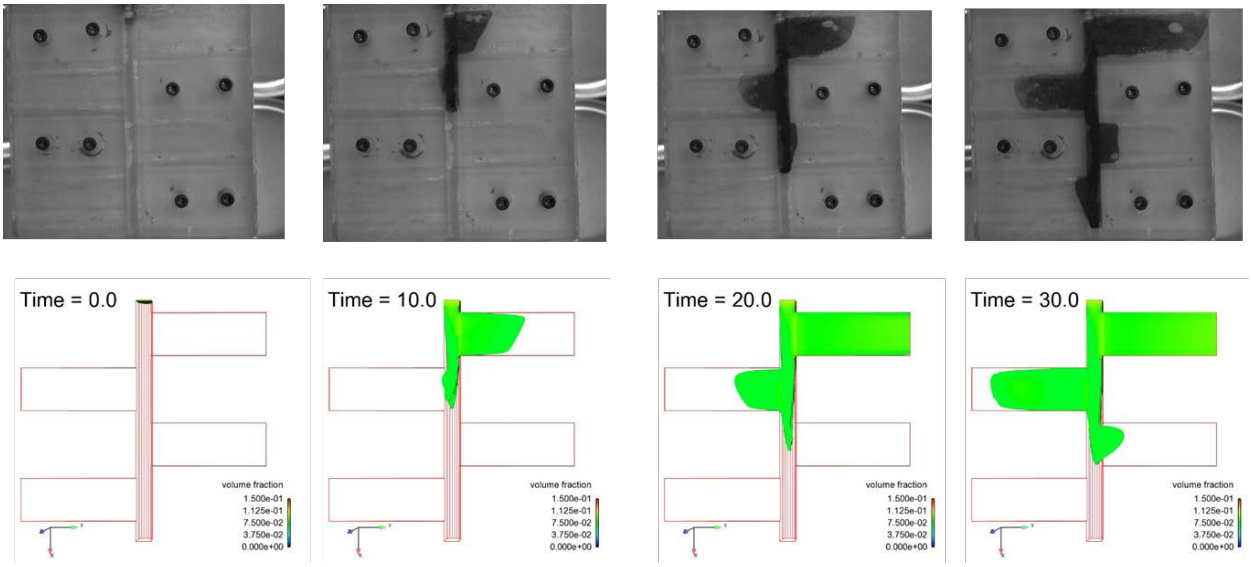

Figure 25. Flow of suspension of "proppant" into the tapered millifluidic device during the first 30s compared to predictions with a Newtonian suspending liquid with a viscosity of 39 Pa-s.

Figure 26 shows the experimental results compared with the simulation results for times between 40 - 70 s. Again one can see that the simulation continues to under predict the extent of the penetration of the suspension into the last channel. The discrepancy of the model may be due to the shear-thinning and viscoelasticity of the guar solution or possibly in small differences in the geometry between the experiment and the model. However, again, the qualitative results are reasonable. More quantitative results may have to wait advances in the constitutive models for guar-based suspensions.

Figures 25 and 26 do not show the settling of the particles. The viscoelasticity of the guar solution is designed to keep the particles in suspension, though we do not have measurements of settling rates of SiC in our guar solution. Again, because of the Newtonian suspending fluid we see a fair amount of sedimentation, as shown in Figure 27. The sedimentation is not uniform because of the influence of the flow field. The top figure uses a continuous phase viscosity of 39 Pa-s and the bottom figure uses 157 Pa-s. As expected, more settling is seen for the lower viscosity case though other flow features are similar. We are having numerical issues at the last channel out flow, where particles are being swept in. A similar effect is see in level set simulations where a hyperbolic equations is marched for long times. To ameliorate this numerical artifact, a boundary condition must be added to Goma to set the the time derivative of the volume fraction to zero.

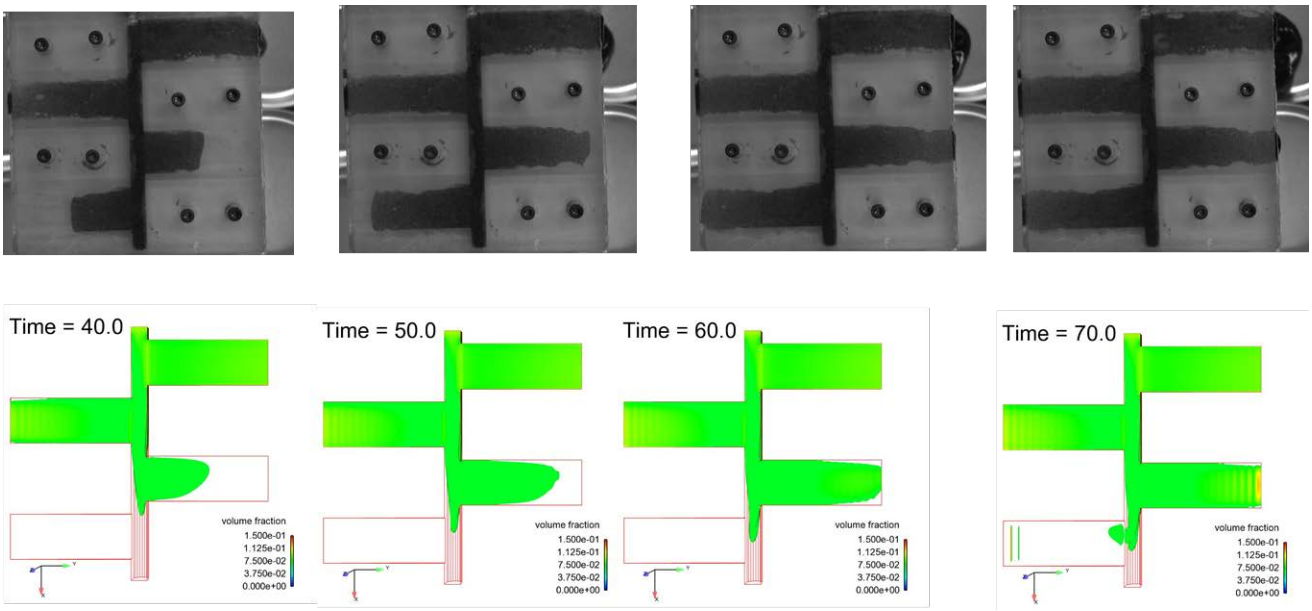

Figure 26. Flow of suspension of "proppant" into the tapered millifluidic device from 40s-70s compared to predictions with a Newtonian suspending liquid with a viscosity of 39 Pa-s.

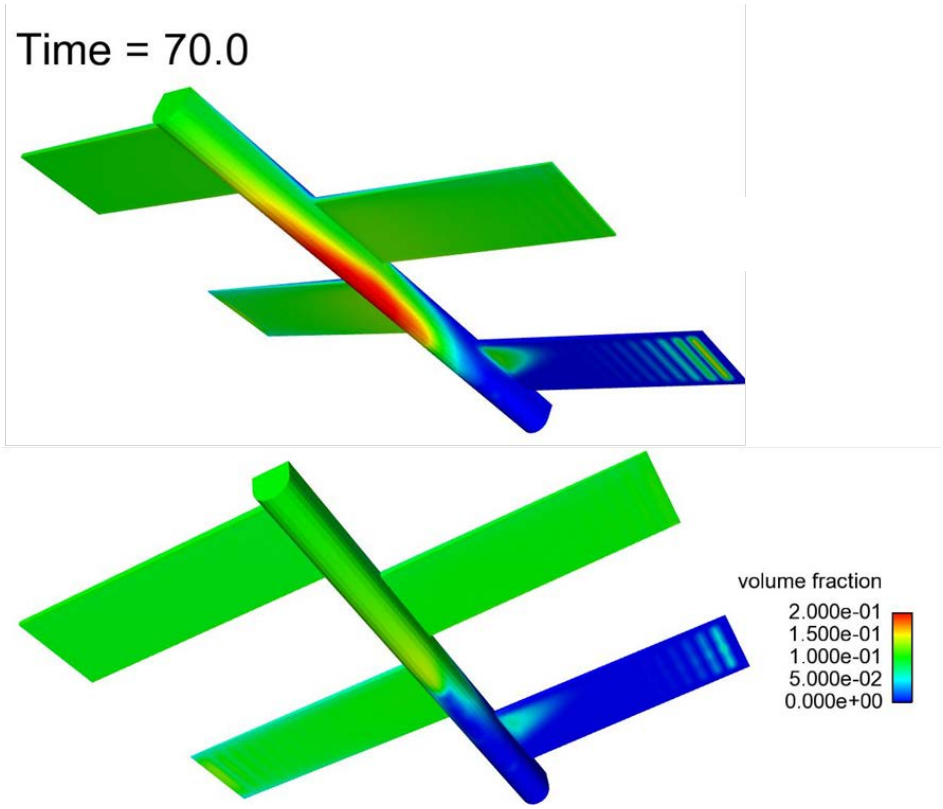

Figure 27. Bottom view of proppant distribution at 70s showing significant particle settling for the SiC. Note the numerical issues associated with the outflow in the channel furthest from the inflow. The top figure uses a continuous phase viscosity of 39 Pa-s and the bottom figure uses 157 Pa-s.

In this experiment, a second camera was added to give a side view of the millifluidic device (Figure 28). Unfortunately, because of the lack of contrast and poor lighting, little can be seen from the camera angle.

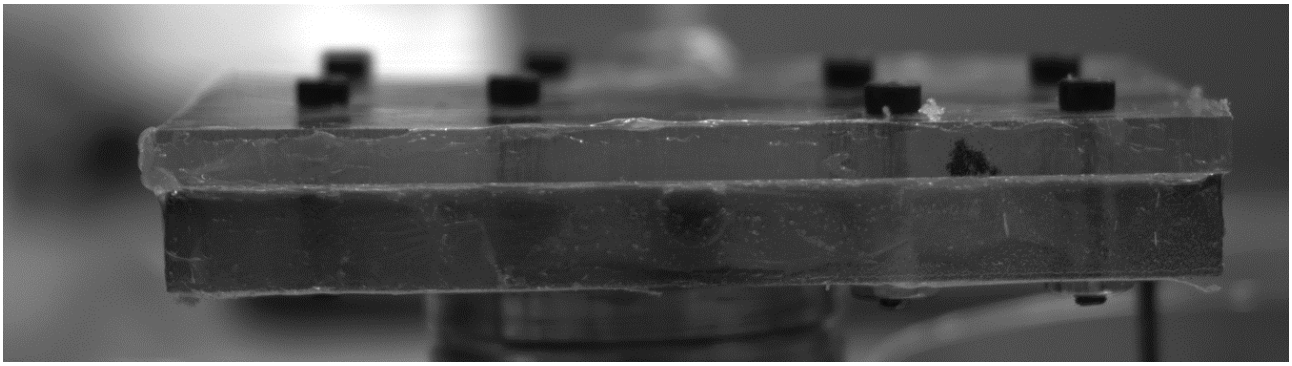

Figure 28. Side view of tapered millifluidic device at 70s.

4.2 Particle-scale simulations of proppant packs

Motivated in part by difficulties in resolving particle details from CT data of laboratory-scale fractures, we set out to generate proppant packings computationally. The manually fractured shale sample (see section 3.2.1 Manual Fracture and Flow and 3.3.1 Manual Fracture and Flow), which yielded the most detailed imaging data on individual particle positions, serves as both motivation and validation for this approach. The proppant structure shown by this manually fractured specimen corresponds to a partial monolayer of proppant particles. This structure has been hypothesized in literature to provide excellent permeability due to the availability of open flow channels (Huitt and Daren, 1960); however, due to the small number of particles, the stresses on particles experienced in field conditions would increase the likelihood of proppant failure and fracture closure (Brannon et al, 2004). Thus, there is a compromise to be made between maintaining open channels for maximizing fracture permeability and packing sufficient proppant particles to maintain a stable, open fracture. To address this, recent efforts have developed proppant mixtures and pumping schedules that purportedly generate highly heterogeneous proppant packings, e.g. the HiWAY proppant technology (Gillard et al, 2010; Medvedev et al, 2013). However, the precise structure of these proppant packs is largely unknown, and direct comparisons between traditional proppant packings, partial monolayer packings, and more recent heterogeneous packings cannot easily be made. The advantage of computationally-generated proppant pack geometries is that we can control the proppant structure and simultaneously measure the stress distribution and fracture permeability. This section describes a brief summary of efforts in this area; a much more detailed description, including a brief review of relevant literature, is included as an attached draft of a submitted journal publication**.**

The overall approach for this aspect of the work is as follows: we use discrete element method (DEM) simulations to artificially generate a series of propped fracture geometries that have variations in proppant loading and proppant structure. DEM simulations track the motion of individual particles as a function of the contact forces between them. We then mesh these packed geometries and compute their permeability using FEM simulations of Stokes flow through the particle packs. From the forces in DEM simulations we compute a single measure of mechanical

stability. We then summarize the results to relate proppant loading and structure to mechanical stability and fracture conductivity. **Error! Reference source not found.** below shows a simple schematic of this approach.

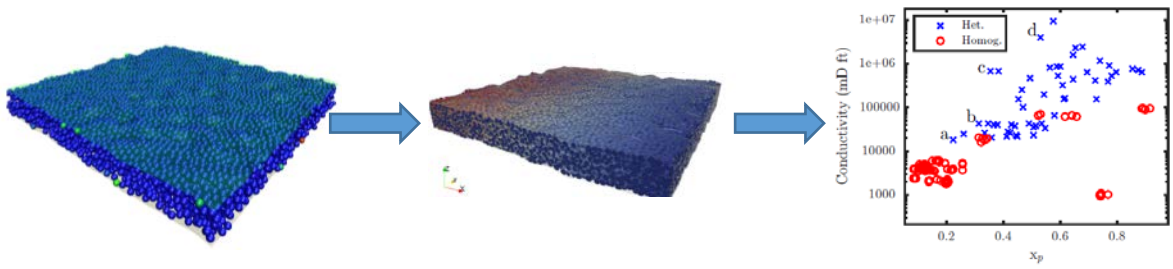

Figure 29: Illustration of overall simulation-based approach. Left: DEM simulations to generate proppant-packed fracture geometry. Middle: FEM flow simulations using explicit proppant pack geometry to compute permeability. Right: Profile of mechanical stability and fracture conductivity for many proppant structures.

4.2.2 Methods

This section is mostly duplicated from the attached journal article draft.

4.2.2.1 Discrete element method simulations for generating proppant packs

Realistic proppant injection processes involve a series of complex highly-coupled physical phenomena, including fracture initiation and propagation, time-dependent suspension flow (usually including viscoelastic effects), and large deformation/fragmentation of proppant particles and the surrounding rock formation. Accurately capturing all of these physics to model proppant injection at the particle scale is not currently feasible; we therefore use simplified particle simulations only to generate proppant packings of interest. We focus on the final (idealized) proppant pack structures for purposes of comparison among different proppant placement strategies, rather than an accurate model of the injection process or high fidelity between the resulting computational geometries and laboratory or field tests. However, we also show that our computer-generated structures are qualitatively similar to experimentally generated proppant packings.

Here the discrete elements represent individual proppant particles, and the rock formation is modeled using rigid boundaries (walls). For simplicity, all proppant particles are assumed to be spheres, which is desirable for a large number of proppants in common use. We model particle-particle and particle-wall interactions using a standard Hertzian spring-dashpot model with a shear history-dependent Coulomb friction criterion. For further details, the interested reader is referred to the work of Silbert et al (Silbert, 2001). Particles are initially randomly placed at a low volume fraction in the space between two surfaces that represent the opposing faces of the fracture. The two surfaces are then moved towards each other at constant velocity to compress the particle pack until a threshold pressure on the walls is reached. This final pressure, which we denote as P_c, is analogous to the confining pressure in the rock formation. The direction of compression is the z-direction, whereas the x and y-directions are periodic (see Figure 30: Initial

state of DEM compression simulation for generating proppant particle packs.), so that no particles are lost during the compression process and finite size effects are minimized.

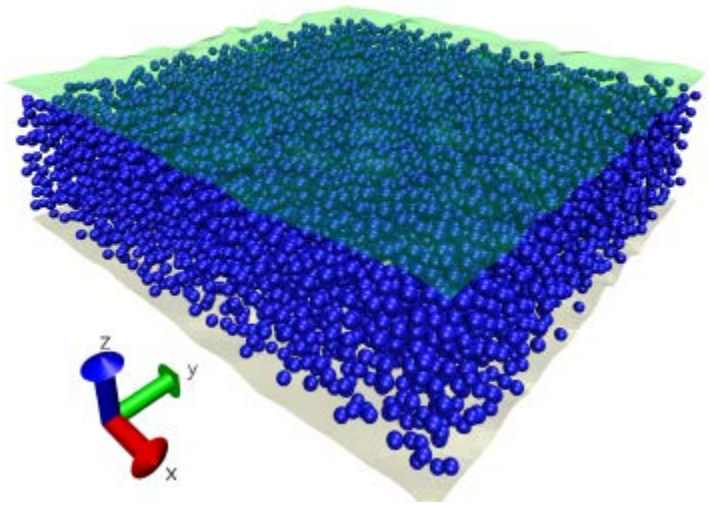

Figure 30: Initial state of DEM compression simulation for generating proppant particle packs.

By varying the initial number of particles, proppant packs with different loadings can be generated. To generate heterogeneous particle packs, particles are removed in specific patterns following the initial compression step, and additional compression is carried out until the confining pressure P_c is reached. To prevent pillars from collapsing and particles from dispersing during this stage, a cohesive force and a rolling friction force are added to the particle-particle and particle-wall interactions (in the case of pillar structures, this is an approximate way to capture the effects of fibrous materials introduced into the frack fluid, which serve a similar purpose in channel fracturing (Gillard et al, 2010). The particle pack structures that correspond to the threshold wall pressure are retained for flow simulations. All DEM simulations are carried out using the LIGGGHTS software package (Kloss, 2012) which includes capabilities for surface-triangle mesh representations of arbitrary surfaces such as the fracture walls. In addition to the normal and tangential damping of the contact interactions, viscous damping is applied to the particle translational motion; this approximates the viscous nature of the surrounding fluid, and more importantly prevents large particle displacements during the compression.

4.2.2.2 Generating fracture wall geometries for simulations

The surfaces that represent the faces of the fracture are generated to resemble realistic laboratory-scale fracture geometries such as that of the manually fracture shale specimen (see section 3.2.1 Manual Fracture and Flow) Since there is likely to be significant variation, as well as limited control and characterization of detailed fracture geometries in field operations, we do not focus on this as a major variable; however, since the fracture geometry can affect proppant packing, we briefly attempt to evaluate its relative importance. To this end, we generate a series

of model fracture surfaces as follows: points are first placed in the *xy* plane in a regular grid pattern (Figure 31a). Each point is randomly translated in the *z* direction, ensuring that the same displacements are applied to points at the *x* and *y* edges to maintain periodicity. Variations in surface tortuosity are achieved by varying the grid spacing of the original points and the mean magnitude of the random displacements; these parameters do not have an appreciable impact on the conclusions that follow (data not shown). The points are then connected by lines, from which a net surface is generated (Figure 31b). The surface is duplicated and translated in the *z* direction to create the opposing fracture face, and triangle meshes are generated for both surfaces (Figure 31c). Variations in the final proppant loading of the fracture are achieved in the DEM simulations by varying the number of particles initially placed between the two surfaces. All geometry and mesh generation is carried out in the CUBIT software package (Blacker et al, 1994). For comparison, a three-dimensional rendering from computed X-ray microtomography of a manually fractured shale sample is shown in Figure 31e.

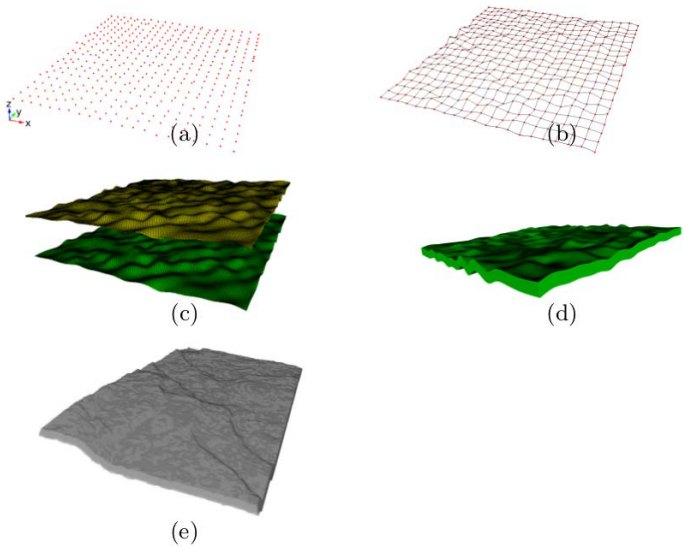

Figure 31 Process of generating fracture geometries. Points are placed in a grid-like pattern with random out-of-plane displacements (a), connected by splines to form a net surface (b), which is then duplicated to form the two faces of the fracture (c). A computer-generated fracture (without proppant) is shown (d) along with an experimentally attained laboratory-scale fracture (e)

4.2.2.3 Stress analysis of the proppant pack

The DEM simulations (see above) allow the calculation of the stress state of the proppant packs during compression: at each time step, normal and tangential forces arising from all particle-particle and particle-wall contacts are computed in the context of a Hertzian (i.e. elastic) contact model. Despite this relatively high level of detail, our model is clearly a significant simplification of the mechanics of a realistic fracture, as it ignores plastic deformation, proppant fracture and crushing, proppant embedment, and spalling of the rock formation, all of which can affect fracture conductivity. However, since we are ultimately interested only in differences among proppant packings, rather than creating a high-fidelity model of the solid mechanics, a much simpler approach is justified. We therefore only compute the distribution of forces exerted on the

proppant particles, and from that distribution compute what fraction of particles would yield under different packing conditions. In reality, high stress on a particular particle could lead to embedment or spalling of the rock formation rather than crushing of the particle, but this is highly dependent on the properties of the rock formation and the proppant. One of our goals is to present an analysis that is general in the context of proppant packing strategies, rather than specific to a particular combination of proppant and rock formation. We therefore only define mechanical stability of a proppant pack in the context of our simple model as the fraction of particles x_p experiencing loads above some critical yield value. Regardless of failure mechanism (crushing, embedment, spalling), we posit that for two different per-particle stress distributions under the same confining pressure, the case with a higher value of x_p is mechanically less stable. However, the resulting mechanical failure would likely adversely affect fracture conductivity in ways that are not captured by the model. We return to this point to qualify our conclusions about the relationship between mechanical stability and fracture conductivity for various proppant packs.

To determine a yield criterion for an individual particle in a compressed proppant pack, one approach is to apply a von Mises yield criterion. This requires detailed knowledge of the stress state of each individual particle; while analytical expressions are available for the local stress in the case of a single load applied on a sphere, no such solution exists for the general case of multiple arbitrarily oriented loads on a sphere, as is the case for the systems of interest here. In principle the stress state can be obtained numerically (e.g. finite element analysis), but this is highly demanding computationally, since it needs to be computed for each particle in each packing configuration. Given the associated computational expense as well as the problematic application of the von Mises yield criterion to particles with potentially heterogeneous structure, we use a much simpler empirical approach due to Ouwerkerk (Ouwerkerk, 1999) that was shown to yield good results. In his work, particle breakage occurs when the maximum normal force applied to a particle $F_{n,max}$ exceeds the side crushing strength (SCS), i.e. $F_{n,max} > \mathrm{SCS}$. The value of the SCS is known to vary with particle material as well as particle size; we denote the SCS for a particle of mean radius r_0 as SCS_0, which we set to a typical value, and adjust accordingly for the particle size dependence. Both analytical and empirical evidence (Jaeger, 1967) show that the SCS scales as $1/r^2$ in typical proppants, where r is the particle radius. We therefore take the particle yield criterion to be:

$$F_{n,max}\left(\frac{r}{r_0}\right)^2 > SCS_0$$

Here, r is the radius of the particle being analyzed and r_0 is the mean particle radius. The distribution of $F_{n,max}(r/r_0)^2$ over a proppant pack is of interest as an indication of the stress state of the particle pack, but can be difficult to interpret or compare among different structures. We can also reduce the distribution to a single measure as discussed above, i.e. by computing the fraction of particles x_p for which relation the yield criterion holds true.

4.2.2.4 Flow simulations using the finite element method

To compute the permeability of various proppant packs, we carry out finite element simulations of flow through the explicit proppant pack geometry. Due to the relatively small dimensions, typical Reynolds numbers satisfy $Re<0.01$, so that simple Stokes flow is adequate. The particles

in this case are static, i.e. no further rearrangement or settling due to flow can occur. The most significant challenge for these simulations is generating the mesh for the domain of interest, which is the interstitial fluid space between proppant particles. To address this, we use the conformal decomposition finite element method (CDFEM) (Noble et al 2010, Lechman et al 2012) to resolve the solid-fluid interface. This involves first generating a uniform background mesh of tetrahedral elements for the entire fracture volume, then using a geometric definition based on level set functions to describe the location of the fluid-solid interface and create new mesh nodes and surfaces accordingly. Following the DEM compression, a uniform tetrahedral mesh is generated for the volume between the two fracture surfaces based on their final location at the end of the compression simulations. Sphere regions corresponding to the locations and radii of proppant particles in the final compressed state are used to define the level set functions. The non-conformal background tetrahedral mesh is then decomposed such that new nodes are added at the zero-crossings of the level sets (i.e. the particle-fluid interfaces). For additional details regarding the CDFEM algorithm, the interested reader is referred to the work of Noble and coworkers (Noble et al 2010, Lechman et al 2012). The result is a mesh that explicitly includes surfaces that conform to the solid-fluid interface for all particles, and the fluid region is then used to solve the steady Stokes flow equations for a Newtonian fluid:

$$\mu\nabla^2\boldsymbol{v} = \nabla \mathrm{P}$$
$$\nabla \cdot \mathbf{v} = 0$$

Here, μ is the viscosity, set to unity with no loss of generality, **v** is the velocity, and *P* is the pressure. Constant pressure boundary conditions are imposed in the *x* direction, i.e. P(x=0) = 0 and P(x=L) = 1, where x=L corresponds to the outlet surface of the fracture. The *y* and *z* directions as well as the fluid-particle interfaces are treated as no-slip surfaces, i.e **v**=0 We use non-LBB compliant first-order linear interpolation functions for both the velocity and pressure fields, which requires the use of a pressure stabilization method. We employ the pressure-stabilized pressure projection method of Bochev and coworkers (Bochev, 2006). To obtain the intrinsic permeability, the flux *q* is obtained by integrating the *x*-component of velocity across the outlet surface, normalized by the total surface area available for flow:

$$q = \frac{\int_{x=L,y,z} \boldsymbol{v} \cdot \mathbf{n} \mathrm{dS}}{\int_{x=L,y,z} \mathrm{dS}}$$

The overall (intrinsic) permeability κ is obtained from re-arranging Darcy's law:

$$\kappa = -\frac{q\mu}{\Delta P/L}$$

Here, ΔP is the imposed pressure difference, and L is the fracture length in the flow direction. Finally, the fracture conductivity *k* is simply the product of the intrinsic permeability and fracture aperture, or width *w* (i.e. the separation of the two fracture surfaces in the final compressed state): k = κw.

For numerical convenience, all simulations are carried out in dimensionless units. With a view to a more applications-oriented presentation, we convert all results to units commonly used in the hydraulic fracturing literature, even if they are occasionally inconsistent. The mean particle radius r_0 defines the length scale in our systems, which we choose to be 0.5 mm; the particle mass density ρ is set to 2.0 g/cm^3, which is typical for lightweight proppants but not meant to represent a particular proppant; the side crushing strength for a particle with radius r_0 is SCS_0= 50N, and the confining pressure P_c = 5000 psi.. Permeability values are reported in Darcies (D), while conductivity values are reported in milli-Darcy feet (mD ft). The key input parameters for the simulations are summarized in Table 1.

Table 1: Summary of key simulation parameters

Parameter	Value
Confining pressure	5000 psi
Mean proppant particle radius r0	0.5 mm
Mean side crushing strength SCS0	50 N
Mass density of proppant particles	2.0 g/cm3
Young's modulus of proppant	10 GPa
Coefficient of restitution for particle collisions	0.3
Coefficient of friction for particles	0.3
Viscous drag coefficient on particles	0.0293 kg/s
Wall velocity in compression	0.10 m/s
Viscosity in FEM model	1
Pressure drop in FEM model	1

4.2.3 Results and Discussion

For the interested reader, this section is presented in much more detail in the attached journal article.

For partial monolayers and homogeneous proppant packs, the key results are shown in Figure 32(a) and (b) below. The hydraulic properties of a range of geometries are plotted as a function of proppant loading in Figure 32(a). Partial monolayers correspond to points to the left of the two dashed lines (proppant loading < 0.25 lb/ft^2). The loadings between these two lines are intermediate between monolayer and multi-layer structures, and are likely not relevant for most applications. Monolayer structures show very high fracture conductivities, which increase as the proppant loading decreases. This corresponds to sparse monolayers, which increases the availability of flow channels, thereby drastically enhancing the permeability and conductivity. However, this comes at the cost of losing mechanical strength, as shown by high values of x_p in Figure 32(b).

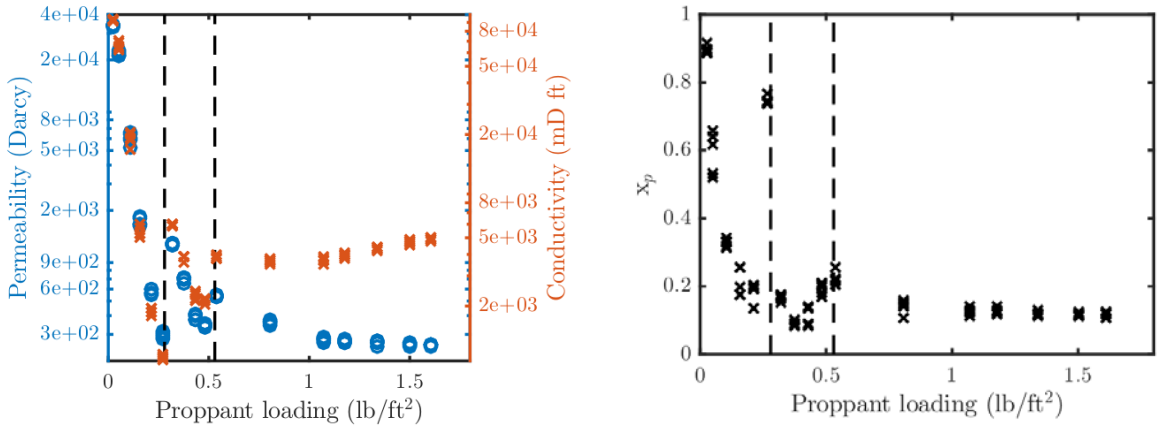

Figure 32: Summary of hydraulic and mechanical properties of partial monolayers and homogeneous proppant structures. (a) Hydraulic properties as a function of loading; partial monolayers correspond to loadings left of the dashed lines (b) Mechanical properties, as expressed by the fraction of particles x_P likely to yield (lower x_P is more stable)

Homogeneous, multi-layered packings correspond to points to the right of the dashed lines in Figure 32(a) and (b) (proppant loadings > 0.5 lb/ft^2); these show moderate conductivity values that are in good agreement with literature values for typical conventional fractures. There is a linear increase with proppant loading in this regime, which corresponds to an increase in fracture aperture; this is indeed the conventional approach to increasing conductivity, but is limited by the additional cost associated with much higher proppant loadings and pumping pressures required to achieve this increased fracture aperture. Mechanical stability is comparatively good for these structures, as expected for conventional fracturing.

We also tested unconventional, heterogeneous proppant pack structures, which resemble those hypothesized to form as a result of e.g. HiWAY channel fracturing (Gillard, 2010). Several examples are shown in Figure 33 below. Since the precise structures of the resulting proppant packs are not known, we explore a wide variety of computer-generated structures. Following the literature (Gillard, 2010; Liu, 2008), we denote two distinct classes of structures as ‘pillars’ and ‘fingers’. These are prepared by removing some particles from homogeneous proppant packs previously prepared as discussed above, and re-compressing to the target confining pressure. For pillar structures, a template of close-packed discs is used to select particles; for finger structures, the template consists of paths traced out by Brownian motion of a disc in the flow direction. Additional details are provided in the attached journal article. While these methods allow us to generate a broad range of structures, there is clearly a virtually unlimited parameter set required to fully describe all possible heterogeneous proppant structures. We therefore only explore a limited range of such parameters that provide a broad sampling of proppant loadings, flow channel sizes and flow channel shapes.

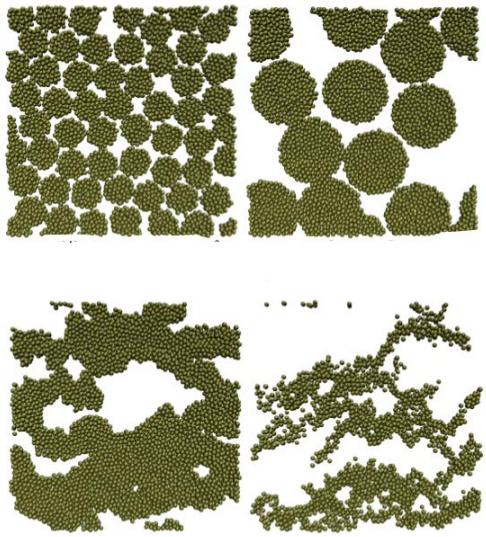

Figure 33: Examples of heterogeneous proppant pack structures. Top: pillar-like structures. Bottom: finger-like structures.

The resulting heterogeneous proppant packs clearly show much greater variation in the hydraulic and mechanical properties as compared to homogeneous proppant packings, as shown in Figure 34(a) and (b).

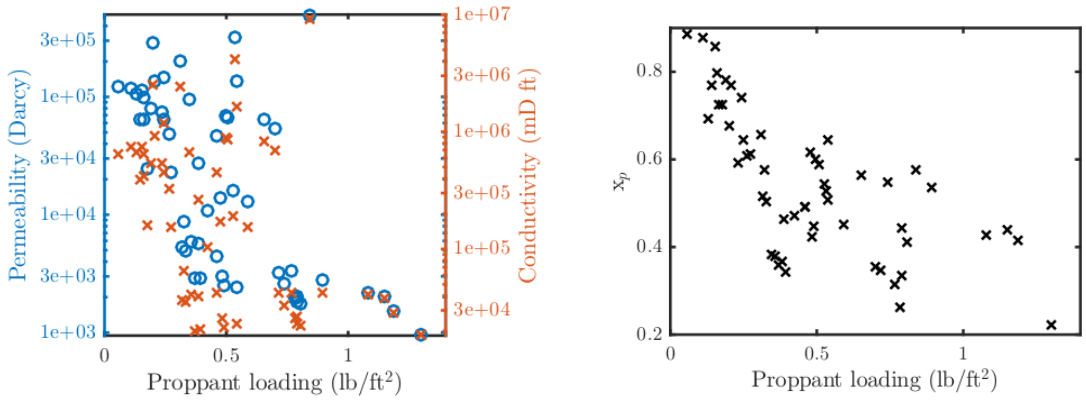

Figure 34: Summary of hydraulic and mechanical properties of heterogeneous proppant structures. (a) Hydraulic properties as a function of loading (b) Mechanical properties, as expressed by the fraction of particles x_P likely to yield (lower x_P is more stable)

Notably, the conductivities that are possible with heterogeneous structures are orders of magnitude higher than conventional homogeneous proppant packs due to the availability of open flow channels. As with partial monolayers, this comes at the cost of mechanical stability, with higher values of x_P for most such structures (see Figure 34b). However, when compared directly to the homogeneous structures, for moderate values of x_P (i.e. moderately stable structures), it appears that the extremely large gains in conductivity can still be retained. In other words, these calculations show that for certain combinations of proppants and rock formations, where both are sufficiently strong to support large stresses on the proppant particles, highly permeable

heterogeneous proppant structures may well be feasible and far superior to traditional fractures. Combined with the experimental characterization of laboratory-scale fractures, which show that heterogeneous proppant packings and in particular partial monolayers are indeed stable and feasible, this suggests a much wider range of potential applications for heterogeneous proppant placement than previously thought.

Our computational approach allows a novel quantitative determination of the regimes in which the tradeoffs between high fracture conductivity and mechanical stability can be made. Figure 35 below presents an effective performance envelope for proppant structures that includes both homogeneous and heterogeneous structures. An increase in the size of the flow channels leads to dramatic increases in conductivity, but also lower mechanical stability (higher x_p). The ideal structure would be in the upper left corner of Figure 35 (high stability, high conductivity), whereas a points near the lower-right corner are the least desirable. We have highlighted several structures that appear to extend the envelope to very high conductivities while retaining moderate mechanical stability. As expected, these structures correspond to open flow channels in the direction of flow (horizontal), see Figure 36.

Under the right circumstances, i.e. in cases where fracture conductivity is the limiting factor for hydrocarbon transport and the rock formation is sufficiently hard to resist spalling under large stresses, heterogeneous structures such as those in Figure 36 may be ideal for reservoir performance.Simulation and experimental work remains to be carried out to show how such structures can in fact be produced (e.g. variations in proppant injection schedules, frack fluid viscosities). However, the CT images of the laboratory-scale fractures discussed in earlier sections suggest that heterogeneous placement of proppant is indeed feasible even under conventional injection techniques (see especially Figure 16). Furthermore, these fractures were stable under laboratory conditions and confining pressures in the range of those found in field conditions, which demonstrates the stability of fractures propped with heterogeneous proppant structures.

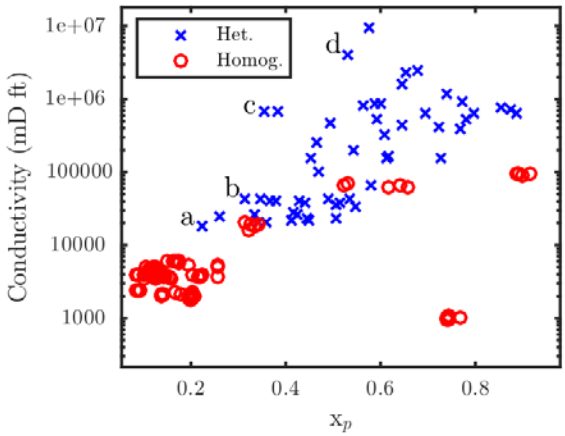

Figure 35: Fracture conductivity and mechanical stability for all proppant structures

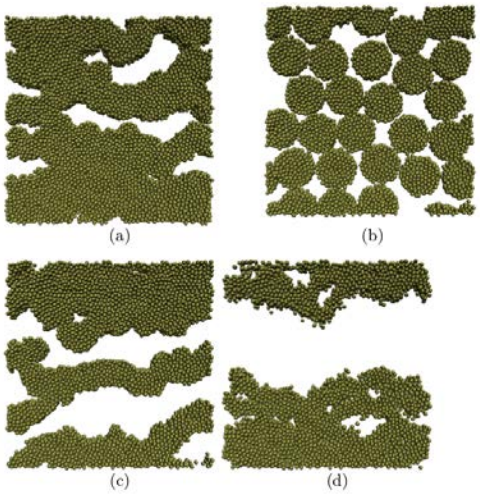

Figure 36: Selected heterogeneous packs with exceptionally high conductivity and moderate mechanical stability

4.2.4 Comparison to manually fractured shale sample

The manually fractured shale specimen discussed in section 3.3.1 Manual Fracture and Flow yielded microCT images with sufficient resolution to discern individual particles and the interstitial flow space (see Figure 11). We have therefore used these data to generate meshes for FEM flow simulations, analogous to the procedure we have used for simulation-generated data above.

The microCT images were sequentially processed using an adaptive thresholding technique, which successfully separated the void (flow) space from the particle/rock phase. In order to separate the fracture (including the particles) from the rock formation, we then applied standard edge detection and flooding image processing techniques. Finally, the most challenging processing step involved separation of individual particles. A 3D distance transform was applied to the entire particle phase, which was then thresholded to isolate the maxima, corresponding roughly to the centers of the particles. These regions were used as seeds for a 3D watershed algorithm that labeled individual regions corresponding to individual particles. All image processing steps were carried out using various features of the open-source tools OpenCV (Bradski, 2000), scikit-image (Van der Walt, 2014) and SciPy (Jones, 2001). Since the particles were known to be spherical, we replaced individual particle regions identified from the images with spheres of equivalent volumes placed at the centers of these regions. The fracture volume was converted to a more convenient CAD-based representation in a manner similar to the construction of computer-generated fracture geometries: a series of spline curves were first created along the top and bottom of the voxel region corresponding to the fracture space. These splines were then connected to create net surfaces corresponding to the two fracture surfaces, which were then swept towards each other in a direction normal to the fracture plane to create the solid volume. A uniform tetrahedral mesh was generated for this volume, and spheres corresponding to proppant particles were then used as input to the CDFEM algorithm to create mesh surfaces corresponding to the particle-fluid interfaces. The resulting mesh was then used to compute permeability from FEM flow simulations as described above. Figure 37 depicts the process of generating a mesh from the micro-CT image data and the resulting geometry.

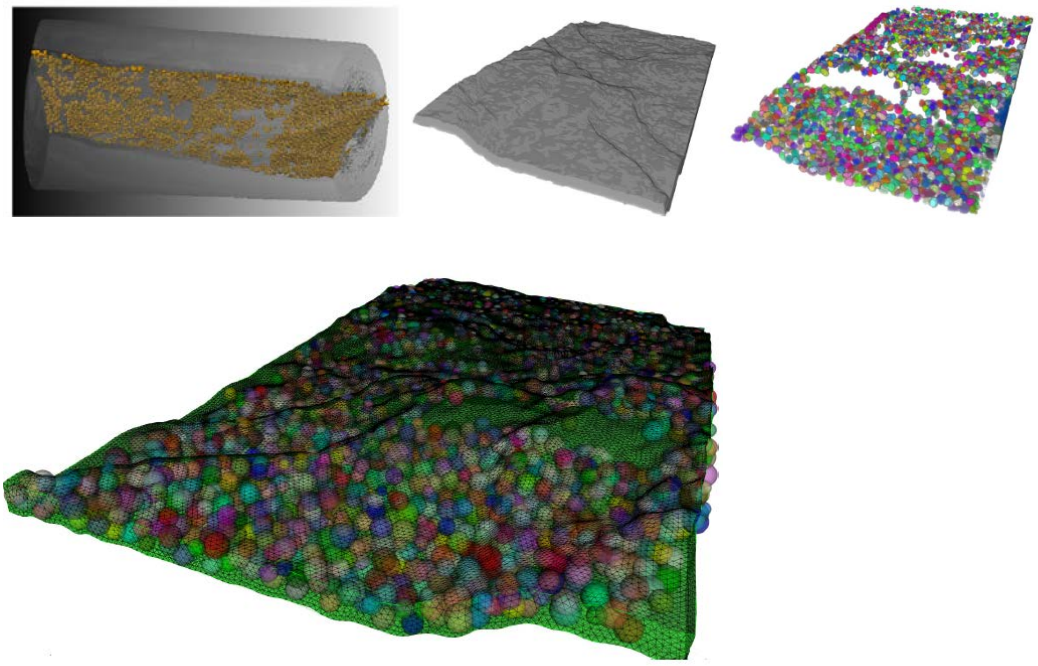

Figure 37: Generating a computational mesh with particle-level detail from micro-CT data. Top row: Image processing steps to convert micro-CT data to segmented voxel-based representations of the fracture volume and individual particles. Bottom: Meshed fracture volume including spherical particles.

A visual inspection of the resulting 3D structure shows this to be a partial monolayer structure, which validates our use of such structures in the computational scheme above. The proppant loading and porosity as computed from this structure are 0.147 lb/ft^2 and 0.561, respectively. These values correspond to a typical partial monolayer in the case of the computer-generated homogeneous packs: see Figure 32, where the closest point is a partial monolayer with a proppant loading of 0.161 lb/ft^2 and a mean porosity averaged over 5 initial conditions of 0.60. The computed conductivity values for the CT-based structure (1600 Darcy and 4580 mD ft at the smallest mesh size tested) are also similar to those obtained for the computer-generated structure (1680 Darcy and 5440 mD ft, averaged over five different initial conditions). These values are in agreement with typical literature values for partial monolayers (Huitt and Darin, 1960. As expected due to the larger flow channels in partial monolayers, they are higher than conventional homogeneous proppant packings, which have permeabilities on the order of 100 Darcy (Gillard, 2010). A direct comparison to experimental measurements of the permeability of the manually fractured shale specimen as measured in the present work was problematic due to suspected large pressure losses in the connecting lines.

5. CONCLUSIONS

This work has explored the realms of proppant host rock interaction, proppant flow, proppant packing within a fracture, and stresses required to generate fractures. In each of these areas a noteworthy step has been made in science. In regards to proppant host rock interaction progressive loading cycles with CT scans between loading cycles determined that cyclic loading of a proppant and host rock as would occur with a pulsed injection scheme results in proppant embedment into the host rock, spalling of the host rock, and reduced permeability, assuming the fracture geometry and proppant pack do not change significantly.

Proppant flow has been shown to be highly dependent on the visco-elastic properties of the carrier fluid, as well as the chemistry of the fluid, as we evidenced with the significant change in rheology with the addition of AlOx particles, which were interacting with the guar and boric acid used to thicken the solution, this was not an issue with SiC. Current codes have trouble with simulating buoyancy of particles due to yield stresses in the fluids, and it does not appear that there is a commercial code that will deal with it, this could become a realm where Sandia could become a forerunner, if effort was put into developing these codes.

Proppant packs within a fracture were examined with CT scans and it was found that homogeneous injection of proppant into a fracture, would generate heterogeneous proppant packs, this suggests that a pulsed injection process may not be necessary to develop heterogeneous proppant packs with open flow channels, which is what most oil service companies are suggesting is necessary to maximize production from wells.

The fractures generated and propped in the lab were relatively unique, in part because they were CT scanned at multiple resolutions this allows the geometry to be examined/modeled at a number of levels. Also the fractures generated in the shale specimen, that was oriented normal to the borehole is the first report of this fracture geometry being generated in the lab that could be found in the published literature.

The efforts in modeling have demonstrated the ability to generate computational meshes from CT scans. Flow patterns were analyzed in greater detail for the scanned specimens, and a wider range of comparable proppant packings were generated computationally. This resulted in a study that examined the relationships between packing structure, mechanical stability and hydraulic properties in both homogeneous and heterogeneous proppant packs.

Modeling of the flow of proppant laden particles has shown the challenges in maintaining buoyancy in particle laden fluids that are yield stress dominated. This has illustrated a large gap in modeling capability, that requires significant effort to develop, and will be necessary for any scale up of modeling results to field scales.

6. SUGGESTIONS OF FUTURE WORK

6.1 Experimental Future Work

First The hydraulic fracture tests need to be completed at higher stresses that are more representative of in situ stress conditions. This should be a relatively trivial matter once the issues with the seals on the injection lines are dealt with. This will provide a solid set of baseline experiments showing the necessary stress states, that must exist in the field to form the fracture geometry that is so often reported in by oil companies. Further to this, it would be even more educational to perform the fracturing tests under true triaxial conditions. The current system as two of the principal stresses equal to one another in an axisymmetric stress state. By performing the tests under true triaxial conditions it would be more educational as to what the stress state of the earth is in the regions where these fractures are occurring. Understanding the stress state of the earth is critical for all subterranean operations.

Injection of proppant into the fractures generated in the shale samples is also necessary as it would be more representative of the field conditions than the geometry tested in granite. It would be a much more representative flow path, and while certainly still heterogeneous, may affect the nature of the proppant pack.

Next, continued millifluidics to support verification and validation of the numerical experiments is also a critical piece of future work. The numerical models are the means to scale up the laboratory results to the field scale and as such need to be as accurate as possible. This would be driven by what is needed by the modelers, however, it is likely that more flow cell geometries, with multiple proppant concentrations would be needed. It would also likely benefit from deeper investigations into the rheology, to include Nuclear Magnetic Resonance (NMR) settling experiments, and settling in visco-elastic fluids.

Finally, Field Scale testing presents its own set of challenges, but a small scale hydraulic fracture and prop experiment could be completed with little additional equipment (Sandia owns the necessary pressurization equipment). This work could include fracture and injection of an interval followed by mine-back of the interval to determine the extent of the proppant penetration, and its distribution. This could also be coupled with near well seismic monitoring, surface tilt meters, and magnetic resistivity measurements, which would provide a full suite of experimental data to determine the extent of the fracture and proppant injection. It would also provide verification and validation of the scale up of numerical experiments.

6.2 Modeling Future Work

Future modeling work in explicit particle-scale models should focus on capturing various features of the dynamics of proppant placement. In this work we have shown which features of pre-prepared proppant structures are desirable and were able to quantify these in detail. However the question remains of how these structures can be generated in a realistic laboratory-scale or field setting. The CT image data shows that the computationally-generated structures are indeed feasible. Future modeling could focus on identifying the fracture conditions under which certain proppant structures form, and how to extrapolate or modify such conditions to different conditions, including those found in field operations. This type of modeling will require an

extension of current capabilities to possibly include explicit particle-scale models of suspensions, coupled to solid mechanics and fracture models for the rock formation. Current capabilities exist in different codes for various aspects of this problem (e.g. Goma for continuum suspension flow, LAMMPS for particle-scale models), but this proposed future work requires coupling such capabilities, which we believe to be an area ripe for future work.

The millifluidic experiments helped us visualize the particle distributions for different proppants and geometries. For future work, we would like to do more careful and reproducible rheology of the guar solution and proppant-guar suspensions. Because mixing protocols and formulations varied during the project, there was some uncertainty in critical modeling parameters like the zero-shear rate viscosity of the extent of shear-thinning and viscoelasticity for the proppant suspensions We would like to design a millifluidic device that shows jamming and propping of the fractures. This may require manufacturing the device from stronger materials that will not open up to allow particles to flow out. We would also like to design an experiment that allows for quantitative concentration determination possibly using fluorescent particles or x-ray or NMR imaging.

The suspensions models used here are obviously much simpler than the real system. For low volume fractions, they provided an adequate match with experiment. However, at higher volume fractions, we seem to be missing important physics which should be explored in future work. These include shear thinning, fluid elasticity, and possibly fluid yield stress. However, without careful rheological characterization and possibly some particle setting experiments in it hard to know what we are missing.

7. REFERENCES

1. Alramahi, B., M.I. Sundberg. 2012. Proppant Embedment and Conductivity of Hydraulic Fractures in Shales. Presented at: *46th US Rock Mechanics/Geomechanics Symposium, Chicago, IL, USA, 24-27 June.*

2. Arthur, J.D., B. Bohm, M. Layne. 2008. Hydraulic Fracturing Considerations for Natural Gas Wells of the Marcellus Shale. Presented at: *The Ground Water Protection Council 2008 Annual Forum, Cincinnati, OH, USA, 21-24 June.*

3. Baihly, J., R. Altman, R. Malpani, and F. Lao. 2010. Shale Gas Production Decline Trend Comparison Over Time and Basins. Presented at: *SPE Annual Technical Conference. Florence, Italy, 19-22 September.*

4. Blacker, T. D., W. J. Bohnhoff, and T. L. Edwards, "Cubit mesh generation environment. volume 1: Users manual," tech. rep., Sandia National Labs., Albuquerque, NM (United States), 1994.

5. Bochev, P.B., Dohrmann, C.R. and Gunzburger, M.D, 2006. Stabilization of low-order mixed finite elements for the Stokes equations, SIAM Journal on Numerical Analysis, vol. 44, no. 1, pp. 82-101

6. Bradski, G. 2000. OpenCV image processing library. *Dr Dobb's Journal of Software Tools.*

7. Brannon, H. D., M. R. Malone, A. R. Rickards, W. D. Wood, J. R. Edgeman, J. L. Bryant, *et al.*, Maximizing fracture conductivity with proppant partial monolayers: theoretical curiosity or highly productive reality?, in *SPE Annual Technical Conference and Exhibition*, Society of Petroleum Engineers, 2004.

8. Daneshy, A. 2005. Proppant Distribution and Flowback in Off-Balance Hydraulic Fractures. Presented at: *2004 SPE Annual Technical Conference and Exhibition. Houston, TX, USA, 26-29 September.*

9. Deng, S., H. Li, G. Ma, H. Huang, and X. Li, Simulation of shale–proppant interaction in hydraulic fracturing by the discrete element method, International Journal of Rock Mechanics and Mining Sciences, vol. 70, pp. 219–228, 2014.

10. Fredd, C.N., S.B. McConnell, C.L. Boney, K.W. England. 2000. Experimental Study of Hydraulic Fracture Conductivity Demonstrates the Benefits of Using Proppants. Presented at: *SPE Rocky Mountain Regional/Low Permeability Reservoirs Symposium, Denver, CO, USA, 12-15 March.*

11. Gangi, A.F. 1978. Wariation of Whole and Fracture Porous Rock Permeability with Confining Pressure. *Int. J. Rock Mech. Min. Sci & Geomech. Abstr.*15:249-257.

12. Gillard, M. R., O. O. Medvedev, P. R. Hosein, A. Medvedev, F. Penacorada, E. d'Huteau, *et al.*, A new approach to generating fracture conductivity, in *SPE Annual Technical Conference and Exhibition*, Society of Petroleum Engineers, 2010.

13. Grillet A.M.; Rao, R.R.; Adolf, D.B.; Kawaguchi, S.; Mondy, L.A. Practical application of thixotropic suspension models. Journal of Rheology, 53, 169(2009)

14. Huitt J. and S. Darin, Effect of a partial monolayer of propping agent on fracture ow capacity," *Trans., AIME*, vol. 219, p. 31, 1960.

15. Morris, J., and N. Chugunov. 2014. Comparison of Heterogeneously-Propped Hydraulic Fractures for Vertical and Lateral Wells. Presented at: *AGU Fall Meeting, 2014. San Francisco, CA, USA, 15-19 December.*

16. Ingraham, M.D., S.J. Bauer, E.C. Quintana, D. Bolintineau, R.R. Rao, J.B. Lechman. 2015. Proppant and host rock deformation in fractured shale flow through experiments. Presented at : *49th US Rock Mechanics/Geomechanics Symposium, San Francisco, CA, USA 28 June-1 July.*

17. Ingraham, M.D., D. Bolintineau, R.R. Rao, S.J. Bauer, E.C. Quintana, J.B. Lechman. 2016. Laboratory Scale Hydraulic Fracture of Marcellus Shale. Presented at : *50th US Rock Mechanics/Geomechanics Symposium, Houston, TX, USA 26-29 June.*

18. Jaeger, J. "Failure of rocks under tensile conditions," International Journal of Rock Mechanics and Mining Sciences, vol. 4, no. 2, pp. 219–227, 1967.

19. Jones, E., Oliphant, T., Peterson, P. *et al*. 2001. SciPy: Open-source scientific tools for Python. [accessed 2016-03-10].

20. Kloss, C., C. Goniva, A. Hager, S. Amberger, and S. Pirker. 2012. Models, algorithms and validation for opensource DEM and CFD–DEM., Progress in Computational Fluid Dynamics, an International Journal, vol. 12, no. 2-3, pp. 140–152.

21. Lechman, J.B., Nemer, M. B., Noble, D.R. 2012. Toward application of conformal decomposition finite elements to non-colloidal particle suspensions, International Journal for Numerical Methods in Fluids, vol. 68, no. 11, pp. 1409-1421

22. Medvedev, A. V., C. C. Kraemer, A. A. Pena, M. K. R. Panga, *et al.*, On the mechanisms of channel fracturing," in *SPE Hydraulic Fracturing Technology Conference*, Society of Petroleum Engineers, 2013.

23. Mondy, L.A., Rao, R.R., Lindgren, E., Sun, A., Adolf, D., Retallack, C., Thompson, K., Modeling Coupled Migration and Settling of Particulates in Curing Filled Epoxies. Journal of Applied Polymer Science, vol. 122 no. 3 pp. 1587-1598, 2011.

24. Noble, D.R., Newren, E. P., Lechman, J. B. 2010. A conformal decomposition finite element method for modeling stationary fluid interface problems, International Journal for Numerical Methods in Fluids, vol. 63, no. 6, pp. 725-742

25. Ouwerkerk, C. “A micro-mechanical connection between the single-particle strength and the bulk strength of random packings of spherical particles,” Powder Technology, vol. 65, no. 1, pp. 125–138, 1991

26. Phillips R.J., Armstrong R.C., Brown R.A., Graham A.L., Abott J.R. *Physics of Fluids A* vol. 4, pp. 30-40, 1992

27. Rao R.R., Mondy L.A., Sun A., Altobelli S.A. A numerical and experimental study of batch sedimentation and viscous resuspension. International Journal of Numerical Methods in Fluids vol, 39, pp. 465-4825, 2002.

28. Rao, R.R., Mondy, L.A., Baer, T.A., Altobelli, S.A., Stephens, T.S., NMR measurements and simulations of particle migration in non-Newtonian fluids. Chemical Engineering Communications vol. 189, no. 1, pp. 1-22, 2002.

29. Samuelson, M.J., J. Stefanski, and R. Downie. 2012. Field Development Study: Channel Hydrauilc Fracturing Achieves Both Operational and Productivity Goals in the Barnett Shale. In *SPE Americas Unconventional Resources Conference, Pittsburgh, PA, USA, 5-7 June*.

30. P.R. Schunk, P.A. Sackinger, R.R. Rao, K.S. Chen, A.C. Sun, M.M. Hopkins, S.R. Subia, P.L. Hopkins, H.K. Moffat, R.A. Roach, D.R. Noble, P.K. Notz, S.A. Roberts, D.A. Labreche, R.B. Secor, and E.D. Wilkes, “GOMA 6.0 - A Full-Newton Finite Element Program for Free and Moving Boundary Problems with Coupled Fluid/Solid Momentum, Energy, Mass, and Chemical Species Transport: User’s Guide,” SAND2013-1844, June, 2013.

31. L. E. Silbert, D. Ertas, G. S. Grest, T. C. Halsey, D. Levine, and S. J. Plimpton, Granular ow down an inclined plane: Bagnold scaling and rheology," *Physical Review E*, vol. 64, no. 5, p. 051302, 2001.

32. Tetlow N, Graham AL, Ingber MS, Subia SR, Mondy LA, Altobelli SA. Journal of Rheology 1998; 42: 307-327.

33. US Energy Information Administration (EIA), “Technically Recoverable Shale Oil and Shale Gas Resources: United Kingdom”, 9/2015

34. US Energy Information Administration (EIA), “Review of Emerging Resources: U.S. Shale Gas and Shale Oil Plays”, 7/2011

35. Van der Walt, S., Schonberger, J. L., Nunez-Iglesias, J., Boulogne, F., Warner, J.D., Yager, N., Gouillart, E., Yu. T. 2014. Scikit-Image: Image processing in python. *PeerJ*, vol 2., p. e453, 6

36. Walsh, J.B., Effect of Pore Pressure and Confining Pressure on Fracture Permeability. *Int. J. Rock Mech. Min. Sci & Geomech. Abstr.*18: 429-435, 1981.

37. Wen, Q., S. Zhang, L. Wang, Y. Liu, X. Li. 2006. The effect of proppant embedment upon the long-term conductivity of fractures. *J. Pet. Sci. and Eng.* 55: 221-227.

38. Zhang K, Acrivos A. Viscous resuspension in fully developed laminar pipe flows. *International Journal of Multiphase Flow*, vol. 20, pp.579-591, 1994.

APPENDIX A: PUBLISHED/SUBMITTED PAPERS

Note: Full copyrighted papers removed.

ARMA 15-0102

Proppant and host rock deformation in fractured shale flow through experiments

Ingraham, M.D., S.J. Bauer, E.C. Quintana, D. Bolintineau, R.R. Rao, J.B. Lechman
Sandia National Laboratories, Albuquerque, NM, USA

This paper was prepared for presentation at the 49th US Rock Mechanics / Geomechanics Symposium held in San Francisco, CA, USA, 28 June-1 July 2015.

ABSTRACT: A series of tests were performed on a manually fractured (subparallel to bedding) and propped (using quartz sand) shale plug to determine the extent to which the proppant fractured and the effect the proppant had on the fracture wall when subjected to reservoir conditions. The specimen was repeatedly subjected to reservoir conditions of 20.7 MPa confining pressure, 6.9 MPa differential stress and a temperature of 75°C. While at reservoir conditions the sample permeability was measured. Periodically the specimen was removed from the test system and scanned with a X-ray micro computed tomography machine to visualize the fracture and proppant. Noticeable decrease in flow was observed with subsequent testing due to fracture closure. This can be attributed to observations of clay swelling, proppant embedment/fracture, and shale wall spalling leading to a decrease in effective fracture aperture. Flow induced particle transport clogged flow paths and impeded flow. It was observed that isolated grains tended to crush whereas continuous grain patches tended to fracture with little displacement and tended towards embedment.

ARMA 16-0085

Laboratory Scale Hydraulic Fracture of Marcellus Shale

Ingraham, M.D., D. Bolintineau, R.R. Rao, S.J. Bauer, E.C. Quintana, J.B. Lechman
Sandia National Laboratories, Albuquerque, NM, USA

ABSTRACT: Performing experiments in the laboratory that mimic conditions in the field is challenging. In an attempt to understand hydraulic fracture in the field, and provide laboratory flow results for model verification, an effort to duplicate the typical fracture pattern for long horizontal wells has been made. The typical “disks on a string” fracture formation is caused by properly orienting the long horizontal well such that it is parallel to the minimum principal stress direction, then fracturing the rock. In order to replicate this feature in the laboratory with a traditional cylindrical specimen the test must be performed under extensile stress conditions and the specimen must have been cored parallel to bedding in order to avoid failure along a bedding plane, and replicate bedding orientation in the field. Testing has shown that it is possible to form failure features of this type in the laboratory. A novel method for jacketing is employed to allow fluid to flow out of the fracture and leave the specimen without risking the integrity of the jacket; this allows proppant to be injected into the fracture, simulating loss of fracturing fluids to the formation, and allowing a solid proppant pack to be developed.

Simulations of the effects of proppant placement on the conductivity and mechanical stability of hydraulic fractures

Dan S. Bolintineanu[a,*], Rekha R. Rao[a], Jeremy B. Lechman[a], Joseph A. Romero[a], Carlos F. Jove-Colon[a], Enrico C. Quintana[a], Stephen J. Bauer[a], Mathew D. Ingraham[a,**]

[a]*Sandia National Laboratories, Albuquerque, NM, USA*

Abstract

The conductivity of propped fractures in natural gas and oil reservoirs is directly related to well productivity, which motivates a fundamental understanding of the effects of proppant placement. We generate a wide range of models of proppant-packed fractures using discrete element simulations, and measure fracture conductivity using finite element flow simulations. This allows for a controlled study of proppant structure and its relationship to fracture conductivity and stress in the proppant pack. For multi-layered packings, we observe the expected increase in fracture conductivity with increasing fracture aperture, while the stress on the proppant pack remains nearly constant. In single-layered packings (i.e. proppant monolayers), there is a drastic increase in fracture conductivity as the proppant volume fraction decreases and open flow channels form, but this also corresponds to a sharp increase in the mechanical stress on the proppant pack. In several cases, heterogeneous packings that resemble those hypothesized to form during channel fracturing show both high conductivity and relatively low stress on the proppant, suggesting that in certain applications these structures are optimal. We also compare our computer-generated structures to micro-CT imaging of a manually fractured laboratory-scale shale specimen. Overall, this work provides a detailed quantitative understanding of the interplay between proppant structure, fracture conductivity and mechanical stability of proppant packs, which helps guide proppant selection and injection strategies.

1. Introduction

Hydraulic fracturing ("fracking") is a highly effective and widely used technique for stimulating production from oil and gas reservoirs, in which high pressure fluids are pumped into wellbores to initiate and expand fractures in the target rock formation. In most applications, after a fracture is generated, a suspension containing proppant particles is injected in order to keep fractures open once the hydraulic pressure is removed. Propped fractures then provide a pathway for rapid transport of hydrocarbons from the rock formation to the wellbore, which in many reservoirs, especially tight shale rocks, is the transport-limiting step. Maintaining high well productivity therefore relies on robustly propped fractures, wherein proppant placement maximizes fracture conductivity, defined as the product of the propped fracture permeability and width. Intuitively one expects a high porosity proppant pack to provide higher fracture conductivity; however, high porosity in the proppant pack also leads to mechanical failure of the proppant, and closure of the fracture. Significant efforts have therefore been made to design proppants and proppant placement strategies aimed at maximizing both of these competing objectives.

Desirable proppants typically have high mechanical strength and ductility (e.g. quartz sand, aluminum [1], reinforced resin pellets [2] or bauxite [3]) and particle properties that yield a relatively high pack porosity (e.g. smooth spherical shapes, with minimal dispersion in particle size [4], or even rod-like particles [5]). In addition to the selection of the proppant material and particle characteristics, placement of proppant in the fracture can have a significant influence on the resulting conductivity. Conventional wisdom dictates that a given proppant will result in a particle pack with a fixed permeability, and the primary way to increase fracture conductivity is to increase the fracture aperture. This in turn implies the existence of multiple proppant layers across the fracture aperture (see Figure 1a). Early work by Darin and Huitt [6] challenged this notion, and proposed the placement of proppant in 'partial monolayers' (see Figure 1b), which could provide exceptionally high porosity and ample flow paths through the proppant pack, while minimizing the quantity of proppant needed. While initially considered impractical due to difficulties in achieving such structures and the instability of the resulting fracture (e.g. closure due to proppant embedment or crushing), subsequent work suggests that this may indeed be feasible [7]. More recently, proppant injection methods have been developed that achieve highly heterogeneous proppant placement, which can lead to drastic improvements in fracture conductivity. The most notable

*Corresponding author
**Principal corresponding author

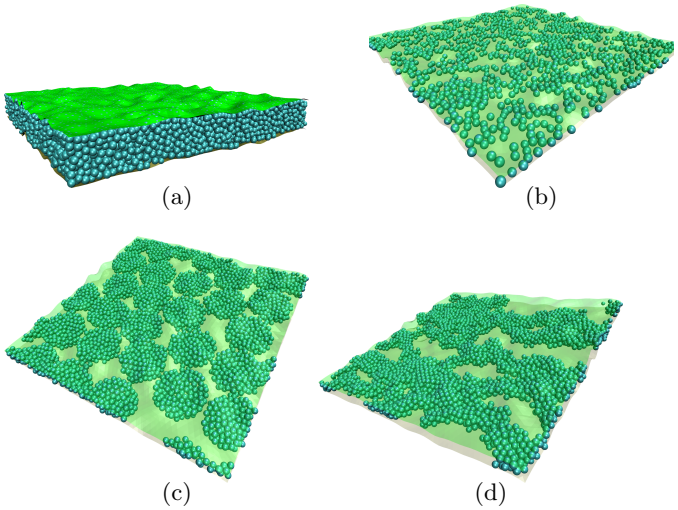

Figure 1: Examples of different types of proppant packs. (a) Homogeneous, multi-layered close packing. (b) Partial monolayers. (c) and (d) Heterogeneous pillar and finger-like structures (resembling those resulting from channel fracturing techniques [8, 9]).

among these are channel fracturing techniques, which involve alternating pulses of proppant-loaded and proppant-free fluid as well as addition of fibrous material [8, 9, 10], resulting in the formation of pillar-like proppant structures separated by open flow channels (see Figure 1c). Other heterogeneous proppant structures have been observed using reverse hybrid fracturing techniques, which involve the use of fracture fluids with highly disparate viscosities and proppant loadings (see Figure 1d) [11]. We refer to conventional proppant placements, where particles are close-packed in multiple layers or monolayers, as homogeneous packings; in contrast, non-traditional proppant structures such as those resulting from channel fracturing will be referred to as heterogeneous packings.

Advancements in fracking technologies are likely to enable additional varieties of heterogeneous proppant pack structures. These have been shown to be effective at increasing fracture conductivity in laboratory-scale experiments as well as field tests [7, 11, 8]. Such results provide useful overall measures of fracture quality, either as direct measures of conductivity (as in laboratory-scale experiments) or in the form of overall well production. However, these measures convolute several important fundamental features of the propped fracture. In field tests especially, the actual proppant placement is nearly always unknown and therefore the structural characteristics of the proppant pack cannot be conclusively related to changes in fracture conductivity and well productivity. In laboratory-scale experiments, the mechanical loading of the proppant pack is typically only assessed based on total confining pressure, which may not be predictive of long-term or field stability.

We therefore undertake a more fundamental simulation-based approach, which allows us to computationally construct a broad range of proppant pack geometries and investigate them in detail with respect to conductivity and mechanical loading characteristics. A key simplification of our approach is that we do not attempt to simulate the proppant injection and fracture generation process. Instead, we use simplified simulations only to generate static proppant pack structures; rather than concerning ourselves with how these structures can be created or how they evolve, we focus exclusively on characterizing their hydraulic and mechanical properties. Nevertheless, our proppant pack generation simulations contain sufficient detail to produce realistic proppant structures that capture the key features of the most commonly hypothesized structures. A comparison with experimental data in the literature as well as in our own work suggest that these structures are indeed realistic and achievable.

Our simulations are based on an explicit particle-scale representation, which is essential for accurate characterization in cases where the fracture aperture is comparable to the particle size, and for heterogeneous particle packings in general. Using discrete element method (DEM) simulations, we first construct various proppant pack geometries, then compute fracture conductivities using finite element method (FEM) simulations of flow through the resulting geometries. The stress state of the particle packs is assessed based on forces computed in the DEM simulations. This work is conceptually distinct from most applications of DEM to hydraulic fracturing, which use bonded particle models to study mechanics and fracture of the rock formation [12, 13, 14]; instead, we use DEM simulations only to represent proppant particles and artificially generate proppant-packed fractures, without addressing the detailed mechanics of the surrounding rock formation. A combination of these approaches, where both the proppant pack structure and the mechanics of the rock formation were studied using DEM, was recently presented by Deng et al [15]. However, their focus was on the mechanics of the rock formation for various particle types and pressures, and they only considered homogeneous, multilayered packings.

Studies in a similar vein to the present work include the work of Khanna et al [16], who used FEM simulations to study permeability in a proppant monolayer consisting of regularly spaced particles with various degrees of embedment. While the flow analysis is in principle similar, we explore a wider range of proppant structures, including multi-layered close packings, monolayers and other heterogeneous packings, and additionally investigate the stress state of the proppant packs. Experimentally, Thompson and coworkers have advanced the use of X-ray microtomography to obtain three-dimensional representations of laboratory-scale homogeneous particle packs [17, 18, 19]. Flow simulations at various stress conditions have been carried out based on the resulting geometries [20, 21, 22]. The simulations that we present here complement such work with a much broader range of simulation-generated proppant packings, and we hope will guide experimental investigations of additional packings and proppant types

of interest, as well as motivate more detailed experimental measurements of particle pack stress states.

The remainder of the paper is organized as follows: in section 2, we present details of DEM simulation methods used for proppant pack generation (2.1) and stress analysis (2.2), as well as methods for flow simulations in the resulting geometries (2.3); in section 3, we present results for a wide range of particle pack geometries, including a qualitative comparison to experiments (section 3.3). Finally, we summarize our results in section 4.

2. Methods

2.1. Discrete element method simulations for generating proppant packs

Realistic proppant injection processes involve a series of complex highly-coupled physical phenomena, including fracture initiation and propagation, time-dependent suspension flow (usually including viscoelastic effects), and large deformation/fragmentation of proppant particles and the surrounding rock formation. Accurately capturing all of these physics to model proppant injection at the particle scale is not currently feasible; we therefore use simplified particle simulations only to generate proppant packings of interest. We focus on the final (idealized) proppant pack structures for purposes of comparison among different proppant placement strategies, rather than an accurate model of the injection process or high fidelity between the resulting computational geometries and laboratory or field tests. However, we also show that our computer-generated structures are qualitatively similar to experimentally generated proppant packings.

Discrete element method simulations have been used extensively to study particulate matter [23]. Here the discrete elements represent individual proppant particles, and the rock formation is modeled using rigid boundaries (walls). For simplicity, all proppant particles are assumed to be spheres, which is desirable for a large number of proppants in common use; however, our simulations could readily be extended to non-spherical particle types, e.g. using a clustered overlapping sphere approach [24]. We model particle-particle and particle-wall interactions using a standard Hertzian spring-dashpot model with a shear history-dependent Coulomb friction criterion. For further details, the interested reader is referred to the work of Silbert et al [25]. Particles are initially randomly placed at a low volume fraction in the space between two surfaces that represent the opposing faces of the fracture. The two surfaces are then moved towards each other at constant velocity to compress the particle pack until a threshold pressure on the walls is reached. This final pressure, which we denote as P_c, is analogous to the confining pressure in the rock formation. The direction of compression is the z-direction, whereas the x- and y-directions are periodic (see Figure 3), so that no particles are lost during the compression process and finite size effects are minimized. By varying the initial number of particles, proppant packs with different numbers of layers can be generated. To generate heterogeneous particle packs (e.g. pillar structures [8]), particles are removed in specific patterns following the initial compression step, and additional compression is carried out until the confining pressure P_c is reached. Further details are provided in section 3.2. To prevent pillars from collapsing and particles from dispersing during this stage, a cohesive force [26] and a rolling friction force [27] are added to the particle-particle and particle-wall interactions (in the case of pillar structures, this is an approximate way to capture the effects of fibrous materials introduced into the frack fluid, which serve a similar purpose in channel fracturing [8]). The particle pack structures that correspond to the threshold wall pressure are retained for flow simulations (see section 2.3). All DEM simulations are carried out using the LIGGGHTS software package [28], which includes capabilities for surface-triangle mesh representations of arbitrary surfaces such as the fracture walls. In addition to the normal and tangential damping of the contact interactions, viscous damping is applied to the particle translational motion; this approximates the viscous nature of the surrounding fluid, and more importantly prevents large particle displacements during the compression.

The surfaces that represent the faces of the fracture are generated to resemble realistic laboratory-scale fracture geometries. Since there is likely to be significant variation, as well as limited control and characterization of detailed fracture geometries in field operations, we do not focus on this as a major variable. However, since the fracture geometry can affect proppant packing, we generate a series of model fracture surfaces as follows: points are first placed in the x-y plane in a regular grid pattern (Figure 2a). Each point is randomly translated in the z direction, ensuring that the same displacements are applied to points at the x and y edges to maintain periodicity. Variations in surface tortuosity are achieved by varying the grid spacing of the original points and the mean magnitude of the random displacements; these parameters do not have an appreciable impact on the conclusions that follow (data not shown). The points are then connected by lines, from which a net surface is generated (Figure 2b). The surface is duplicated and translated in the z direction to create the opposing fracture face, and triangle meshes are generated for both surfaces (Figure 2c). Variations in the final proppant loading of the fracture are achieved in the DEM simulations by varying the number of particles initially placed between the two surfaces. All geometry and mesh generation is carried out in the CUBIT software package [29]. For comparison, a three-dimensional rendering from computed X-ray microtomography of a manually fractured shale sample (see section 2.4) is shown in Figure 2e.

2.2. Stress analysis of the proppant pack

The DEM simulations (see above) allow the calculation of the stress state of the proppant packs during compression: at each time step, normal and tangential forces

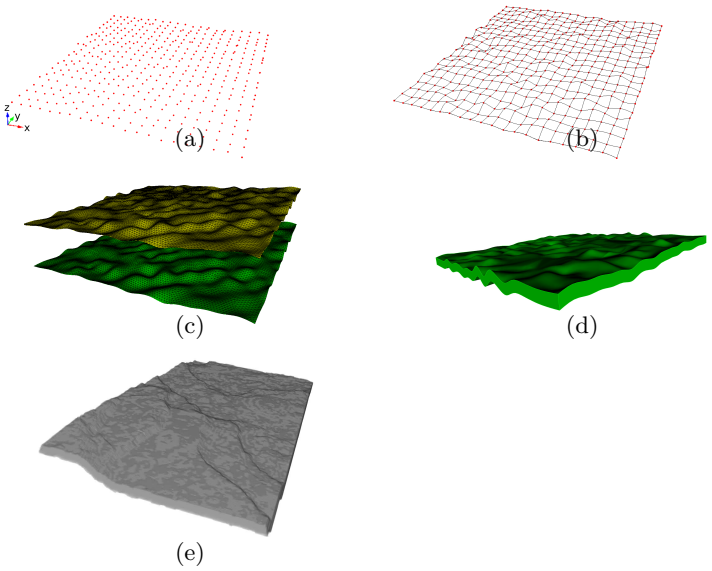

Figure 2: Process of generating fracture geometries. Points are placed in a grid-like pattern with random out-of-plane displacements (a), connected by splines to form a net surface (b), which is then duplicated to form the two faces of the fracture (c). A computer-generated fracture (without proppant) is shown (d) along with an experimentally attained laboratory-scale fracture (e)

arising from all particle-particle and particle-wall contacts are computed in the context of a Hertzian (i.e. elastic) contact model. Despite this relatively high level of detail, our model is clearly a significant simplification of the mechanics of a realistic fracture, as it ignores plastic deformation, proppant fracture and crushing, proppant embedment, and spalling of the rock formation, all of which can affect fracture conductivity. However, since we are ultimately interested only in differences among proppant packings, rather than creating a high-fidelity model of the solid mechanics, a much simpler approach is justified. We therefore only compute the distribution of forces exerted on the proppant particles, and from that distribution compute what fraction of particles would yield under different packing conditions. In reality, high stress on a particular particle could lead to embedment or spalling of the rock formation rather than crushing of the particle, but this is highly dependent on the properties of the rock formation and the proppant. One of our goals is to present an analysis that is general in the context of proppant packing strategies, rather than specific to a particular combination of proppant and rock formation. We therefore only define mechanical stability of a proppant pack in the context of our simple model as the fraction of particles x_p experiencing loads above some critical yield value. Regardless of failure mechanism (crushing, embedment, spalling), we posit that for two different per-particle stress distributions under the same confining pressure, the case with a higher value of x_p is mechanically less stable. However, the resulting mechanical failure would likely adversely affect fracture conductivity in ways that are not captured by the model. We return to this point to qualify our conclusions about the relationship between mechanical stability and fracture conductivity for various proppant packs.

To determine a yield criterion for an individual particle in a compressed proppant pack, one approach is to apply a von Mises yield criterion. This requires detailed knowledge of the stress state of each individual particle; while analytical expressions are available for the local stress in the case of a single load applied on a sphere [30], no such solution exists for the general case of multiple arbitrarily oriented loads on a sphere, as is the case for the systems of interest here. In principle the stress state can be obtained numerically (e.g. finite element analysis), but this is highly demanding computationally, since it needs to be computed for each particle in each packing configuration. Given the associated computational expense as well as the problematic application of the von Mises yield criterion to particles with potentially heterogeneous structure, we use a much simpler empirical approach due to Ouwerkerk [31] that was shown to yield good results. In his work, particle breakage occurs when the maximum normal force applied to a particle $F_{\mathrm{n,max}}$ exceeds the side crushing strength (SCS), i.e. $F_{\mathrm{n,max}} > \mathrm{SCS}$. The value of the SCS is known to vary with particle material as well as particle size; we denote the SCS for a particle of mean radius r_0 as SCS_0, which we set to a typical value, and adjust accordingly for the particle size dependence. Both analytical and empirical evidence [32] show that the SCS scales as $1/r^2$ in typical proppants, where r is the particle radius. We therefore take the particle yield criterion to be:

$$F_{\mathrm{n,max}}(r/r_0)^2 > \mathrm{SCS}_0 \tag{1}$$

Here, r is the radius of the particle being analyzed and r_0 is the mean particle radius. The distribution of $F_{\mathrm{n,max}}(r/r_0)^2$ over a proppant pack is of interest as an indication of the stress state of the particle pack, but can be difficult to interpret or compare among different structures. We can also reduce the distribution to a single measure as discussed above, i.e. by computing the fraction of particles x_P for which relation 1 holds true. An example of this analysis including the distribution of $F_{\mathrm{n,max}}(r/r_0)^2$ follows in section 3.

2.3. Flow simulations using the finite element method

To compute the permeability of various proppant packs, we carry out finite element simulations of flow through the explicit proppant pack geometry. Due to the relatively small dimensions, typical Reynolds numbers satisfy $Re < 0.01$, so that simple Stokes flow is adequate. The particles in this case are static, i.e. no further rearrangement or settling due to flow can occur. The most significant challenge for these simulations is generating the mesh for the domain of interest, which is the interstitial fluid space between proppant particles. To address this, we use the conformal decomposition finite element

method (CDFEM) [33, 34] to resolve the solid-fluid interface. This involves first generating a uniform background mesh of tetrahedral elements for the entire fracture volume, then using a geometric definition based on level set functions to describe the location of the fluid-solid interface and create new mesh nodes and surfaces accordingly. Following the DEM compression, a uniform tetrahedral mesh is generated for the volume between the two fracture surfaces based on their final location at the end of the compression simulations. Sphere regions corresponding to the locations and radii of proppant particles in the final compressed state are used to define the level set functions. The non-conformal background tetrahedral mesh is then decomposed such that new nodes are added at the zero-crossings of the level sets (i.e. the particle-fluid interfaces). For additional details regarding the CDFEM algorithm, the interested reader is referred to the work of Noble and coworkers [33, 34]. The result is a mesh that explicitly includes surfaces that conform to the solid-fluid interface for all particles, and the fluid region is then used to solve the steady Stokes flow equations for a Newtonian fluid:

$$\begin{aligned} \mu\nabla^2\mathbf{v} &= \nabla P \\ \nabla\cdot\mathbf{v} &= 0 \end{aligned} \tag{2}$$

Here, μ is the viscosity, set to unity with no loss of generality, $\mathbf{v}$ is the velocity, and P is the pressure. Constant pressure boundary conditions are imposed in the x-direction, i.e. $P(x=0)=0$ and $P(x=L)=1$, where $x=L$ corresponds to the outlet surface of the fracture. The y and z directions as well as the fluid-particle interfaces are treated as no-slip surfaces, i.e. $\mathbf{v}=0$. We use non-LBB (Ladyženskaja-Babuška-Brezzi) compliant first-order linear interpolation functions for both the velocity and pressure fields, which requires the use of a pressure stabilization method. We employ the pressure-stabilized pressure projection method of Bochev and coworkers [35]. To obtain the intrinsic permeability, the flux q is obtained by integrating the x-component of velocity across the outlet surface, normalized by the total surface area available for flow:

$$q = \frac{\int_{x=L}\mathbf{v}\cdot\mathbf{n}dS}{\int_{x=L}dS} \tag{3}$$

The overall (intrinsic) permeability κ is obtained from rearranging Darcy's law:

$$\kappa = -\frac{q\mu}{\Delta P/L} \tag{4}$$

Here, ΔP is the imposed pressure difference, and L is the fracture length in the flow direction. Finally, the fracture conductivity k is simply the product of the intrinsic permeability and fracture aperture, or width w (i.e. the separation of the two fracture surfaces in the final compressed state):

$$k = \kappa w \tag{5}$$

Parameter	Value
Confining pressure	5000 psi
Mean proppant particle radius r_0	0.5 mm
Mean side crushing strength SCS_0	50 N
Mass density of proppant particles	2.0 g/cm^3
Young's modulus of proppant	10 GPa
Coefficient of restitution for particle collisions	0.3
Coefficient of friction for particles	0.3
Viscous drag coefficient on particles	0.0293 kg/s
Wall velocity in compression	0.10 m/s
Viscosity in FEM model	1.0
Pressure drop in FEM model	1.0

Table 1: Summary of key simulation parameters

For numerical convenience, all simulations are carried out in dimensionless units. With a view to a more applications-oriented presentation, we convert all results to units commonly used in the hydraulic fracturing literature, even if they are occasionally inconsistent. The mean particle radius r_0 defines the length scale in our systems, which we choose to be 0.5 mm; the particle mass density ρ is set to 2.0 g/cm^3, which is typical for lightweight proppants but not meant to represent a particular proppant; the side crushing strength for a particle with radius r_0 is $SCS_0 = 50$N, and the confining pressure $P_c = 5000$ psi. Permeability values are reported in Darcies (D), while conductivity values are reported in milli-Darcy feet (mD ft). The key input parameters for the simulations are summarized in Table 1.

2.4. Preparation and imaging of a laboratory-scale proppant-packed shale sample

The use of simulation-based proppant packs was partly motivated by challenges associated with laboratory-scale fractured samples, in particular characterizing proppant placement following fracture in sufficient detail. However, to verify that our simulation-based structures are realistic, we compare them to a manually-fractured shale sample for which we were able to obtain micro-computed tomography (microCT) data showing proppant placement.

The manually fractured shale specimen was a core plug, nominally 25.4 mm in diameter, and 50.8 mm in length. The composition of the shale was 5-10% porosity, and 10-40% clay. The plug was fractured by hand, subparallel to bedding to create a single through-going fracture. A clean quartz 20-30 sieve proppant was distributed within the fracture space in a monolayer. The halves of the specimen were then reassembled, and held together with a piece of polyvinyl chloride tubing. The specimen was then jacketed in a UV cure polyurethane .

Micro-CT data was accomplished with a Comet MXR-451HP/11 source operated at 400 kV and 3.8 mA, coupled

with a Perkin Elmer XRD1620 Detector. The scan took approximately 150 minutes, while images were collected with North Star Imaging software. Post-processing, reconstruction, and rendering were performed with VG Studio Max . Further details on the experimental procedure were discussed by Ingraham et al [36].

3. Results and Discussion

A series of DEM simulations were carried out to generate proppant packs as discussed in section 2.1. Figure 3 shows several stages in the compression of a proppant pack from the dilute state to the final compressed state, with particles colored by their yield criterion, i.e. $F_{\mathrm{N,max}}(r/r_0)^2$ (see equation 1 and related discussion). The particle size distribution in this case is Gaussian with mean $r_0 = 0.5$mm and standard deviation $\sigma = 0.025$mm. Particles experience little or no stress until the end of the compression, where the close-packed state is reached. At this point, there is some heterogeneity in the distribution of the stress, as seen by the variability in coloring in figure 3d. This is confirmed quantitatively in figure 4. In panel (a), the confining pressure and the fraction x_P of particles likely to fail, i.e. those with $F_{\mathrm{N,max}}(r/r_0)^2 > \mathrm{SCS}_0$, are plotted as a function of simulation time. There is a sharp rise in both quantities near the end of the simulation. In panel (b), we plot the distribution of $F_{\mathrm{N,max}}(r/r_0)^2$ over the particle pack for several time steps near the end of the compression. The vertical dashed line indicates the chosen yield criterion, SCS_0; the quantity x_P is equivalent to the area under each curve that falls to the right of this line. There is a significant spread in the per-particle stress distribution, which appears to increase as the final state is reached. Furthermore, the shape of the distributions may be indicative of packing order (e.g. generation of force chains) and provide clues to the potential failure mechanism of the proppant pack; however, for the present purposes, we limit the discussion to the quantity x_P, which effectively reduces the distributions to a single parameter indicative of mechanical stability.

3.1. Homogeneous proppant packs

Multiple compression simulations were carried out to span a range of fracture apertures, ranging from partial monolayers to multiple layers. The proppant pack thickness was controlled by varying the number of particles initially placed in the dilute state. This amounts to variations in the proppant loading ρ_P, in units of lb/ft^2 (i.e. mass of proppant per unit area of fracture surface). In addition, for each value of the proppant loading, five compression simulations were carried out with different random seed values used for the initial placement of the particles. This allows us to quantify variability in the results due to the inherent variability of the particle packings.

Figure 5 shows the porosity and fracture aperture for a range of proppant loading values. The porosity here is

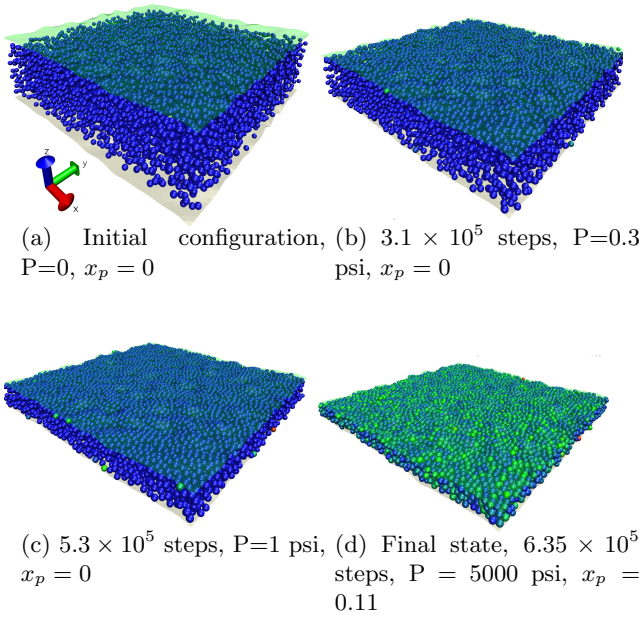

(a) Initial configuration, P=0, $x_p = 0$

(b) 3.1×10^5 steps, P=0.3 psi, $x_p = 0$

(c) 5.3×10^5 steps, P=1 psi, $x_p = 0$

(d) Final state, 6.35×10^5 steps, P = 5000 psi, $x_p = 0.11$

Figure 3: Images of a typical homogeneous proppant pack as the compression simulation progresses. Particles are colored by their stress, $F_{\mathrm{N,max}}(r/r_0)^2$, with colors scaled to the maximum value at each step (blue→green→red indicates increasing force).

calculated based on the total volume of particles and the total fracture volume, and does not account for particle-particle and particle-wall overlaps due to the Hertzian contact model. In most cases, these are at most a few percent of the particle volume, so the error is not significant. At each proppant loading, the five different data points correspond to five different proppant packs generated from different initial conditions; in most cases, the points overlap so closely that they are indistinguishable. Some variation is noted in both the porosity and fracture aperture at low proppant loadings as a function of initial conditions. These lower proppant loading values correspond to smaller total numbers of particles (effectively smaller sample sizes), which is why there is more variability in these cases and why the effect quickly disappears at larger loadings.

More importantly, the data suggest the existence of three distinct regimes of packing behavior, indicated by dashed vertical lines. In the low proppant loading regime (ρ_P 0 to ∼0.3 lb/ft^2), the packing structure corresponds to partial monolayers (e.g. see figure 1b). As particle density decreases, the porosity therefore increases very sharply. This is because the total fracture volume remains roughly constant, while any decrease in proppant loading leads to a corresponding decrease in proppant volume. The fracture aperture is approximately constant at 1.0 mm, corresponding to a single particle diameter, as expected for monolayers. There is a slight decrease in fracture aperture, particularly at very low proppant loadings, since there are fewer particles supporting the total pressure (recall that all data points correspond to the same confining pressure of 5000 psi); in the Hertzian contact model we use, this

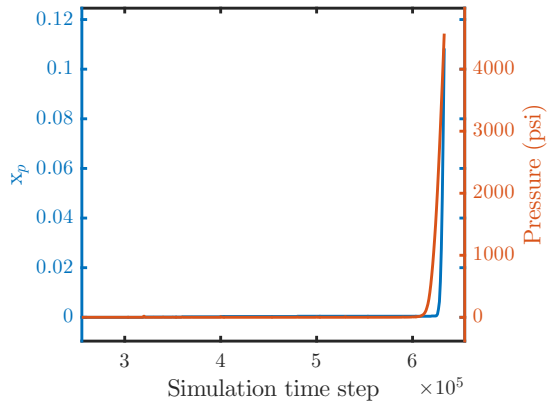

(a)

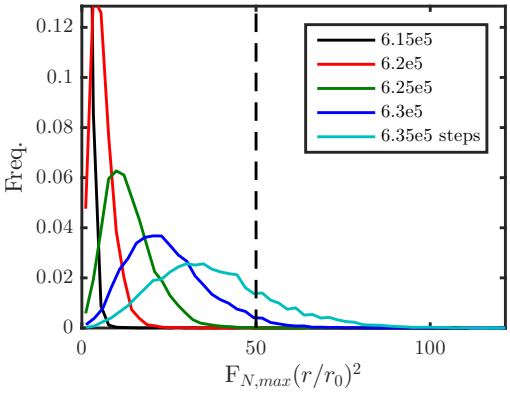

(b)

Figure 4: Key quantities during the compression process. (a) Fraction of particles x_P likely to yield (left axis) and confining pressure (right axis) as a function of simulation time. (b) Distribution of $F_{\mathrm{N,max}}(r/r_0)^2$ over all particles near the end of the simulation. The vertical dashed line represents the chosen yield criterion SCS_0.

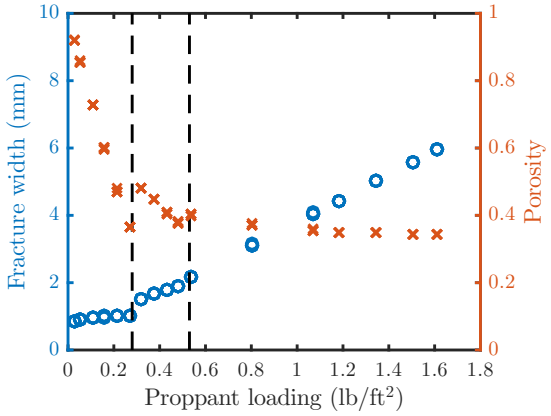

Figure 5: Fracture width (left axis) and porosity (right axis) as a function of proppant loading.

leads the confining walls to have larger contact overlap with the proppant particles, which allows the walls to approach each other more closely. At the opposite end of the proppant loading range ($\rho_P > 0.55$ lb/ft^2), the dominant proppant structures are multi-layered, close-packed homogeneous structures (e.g. see figure 1a). In this regime, the fracture aperture increases linearly, since any increase in proppant loading is directly accommodated by expanding the fracture aperture. The porosity remains approximately constant, corresponding to the close-packed porosity given the proppant size distribution; the slight decrease in figure 5 is due to higher porosity near the relatively smooth fracture walls, an effect that diminishes with increasing fracture aperture.

In the intermediate/transition regime (0.3 lb/ft$^2 < \rho_P < 0.6$ lb/ft^2), the proppant loading is too large to form single monolayers, but insufficient to form two (or more) close-packed layers, which would correspond to a fracture aperture of 2 mm or higher. At the low end of this regime (~ 0.3 lb/ft^2), there is a notable jump in porosity as the second but sparsely populated particle layer forms. The porosity decreases somewhat sharply as this layer is populated, and particles in this layer are under high compression forces as a result, as shown below. As the third layer begins to form, indicated by a fracture aperture $\geq$2 mm, there is again an increase in porosity, but the effect is smaller than before, since the larger packing can now accommodate additional particles much more easily. The effect just described all but disappears with subsequent layers, and may well be a result of the highly constrained packing protocol and limited system size employed here. In a real fracture, convection into empty regions of the large fracture, fracture expansion and/or proppant failure would likely occur to accommodate these highly stressed states. As such, this intermediate regime may not be practically relevant, but its discussion is needed to clarify some of the data that follow.

The mechanical stability of these proppant packs is analyzed by plotting the fraction of particles x_P with $F_{\mathrm{N,max}}(r/r_0)^2 > \mathrm{SCS}_0$ as a function of proppant loading (see section 2.2). The full range of proppant loadings is plotted, which shows the highly stressed states corresponding to the formation of new layers with frustrated packings in the intermediate proppant density regime ($\rho_P \sim 0.3$ lb/ft^2 to 0.55 lb/ft^2) discussed above. The low and high proppant loadings correspond to partial monolayer and homogeneous multi-layered structures, respectively. In the former case, we note a rapid increase in x_P as the proppant density decreases, which corresponds to depletion of a full monolayer to partial monolayers of increasingly higher porosity. The sharp increase in x_P is due to the fact that fewer particles are available to support the same confining pressure of 5000 psi, resulting in larger per-particle normal forces. In the case of homogeneous multi-layered proppant pack structures, there is a gradual decrease in x_P as the proppant loading, the fracture aperture and the number of layers increase. This is because a wider fracture with more

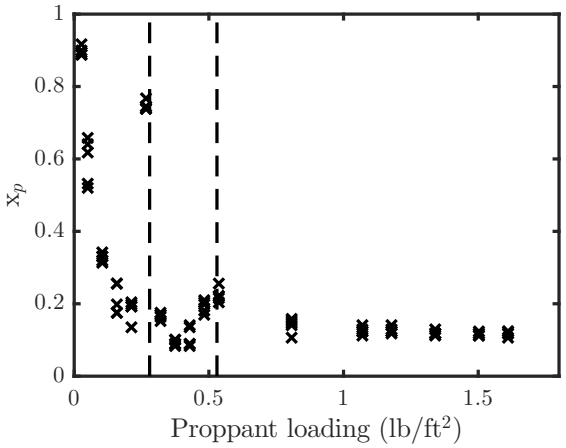

Figure 6: Fraction of particles x_P likely to yield as a function of proppant loading. x_P is defined as the fraction of particles with $F_{\mathrm{N,max}}(r/r_0)^2 > \mathrm{SCS}_0$.

proppant particles has more degrees of freedom to achieve a compliant, mechanically stable state, which in turn can accommodate the same confining pressure with smaller per-particle forces. This effect is therefore expected to saturate at large fracture apertures/loadings. Finally, the variation in x_P among different starting states is larger than the variation in porosity or fracture aperture (see figure 5). This is not surprising, since a small decrease in the fracture aperture can have a large impact on the mechanical state, as seen by the distributions of $F_{\mathrm{N,max}}(r/r_0)^2$ in figure 4b, which differ by relatively few simulation steps but have large differences in x_P. As before, the variability is more pronounced for fractures with fewer particles, i.e. lower proppant loadings, as these effectively represent smaller samples.

The proppant particle configuration corresponding to the final state in each system was used to define the input geometry for finite element flow simulations. The details of the simulation setup were discussed in section 2.3. Figure 7 shows the results of FEM simulations in two different particle packs, corresponding to a representative partial monolayer as well as a multi-layered structure.

The permeability and fracture conductivity were computed as described in section 2.3 for a range of CDFEM background mesh sizes. Mesh sensitivity results for one case are plotted in the inset of figure 7(a). A smaller mesh size corresponds to a higher fidelity between the finite element mesh and the particle geometry generated by DEM simulations, but incurs significant additional computational cost. The computed permeability in the inset of figure 7(a) does not converge perfectly with mesh size, but for all cases we have not observed differences in the computed permeability that would affect the trends or conclusions in any significant way. While additional refinements in the meshing procedure may be of interest in future work, given the small differences seen between different particle configurations for a given loading (8) and

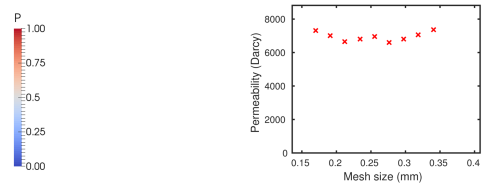

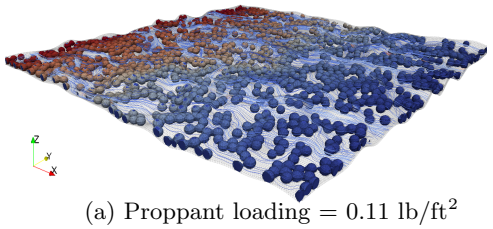

(a) Proppant loading = 0.11 lb/ft^2

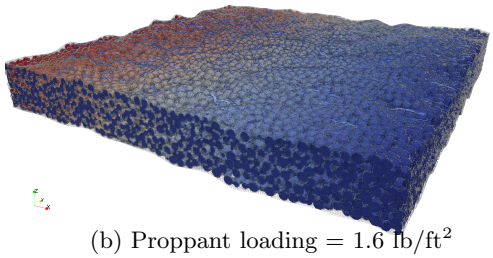

(b) Proppant loading = 1.6 lb/ft^2

Figure 7: Visualization of results of finite element simulations of Stokes flow through two particle geometries. Flow is in the x-direction, as indicated by the gradient in pressure, which corresponds to the coloring of the particles. Flow streamlines are shown for both cases, but are difficult to see in the high proppant loading case due to the dense packing. The computed fracture conductivity as a function of mesh size is shown in the inset plot for panel (a).

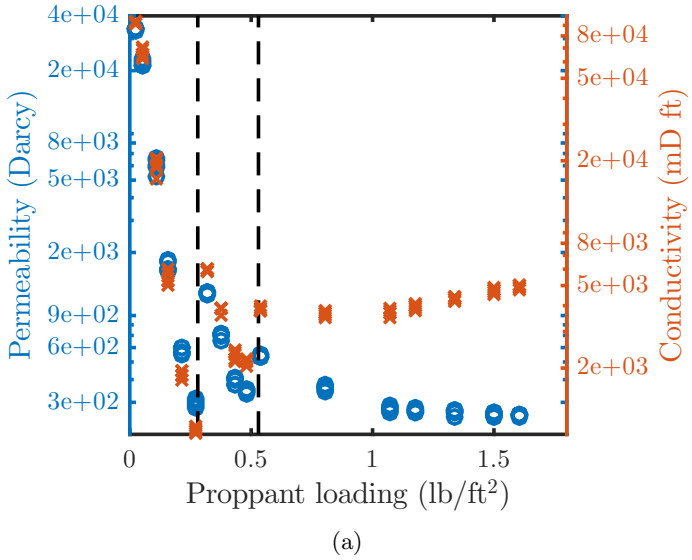

Figure 8: Permeability and fracture conductivity as a function of proppant loading.

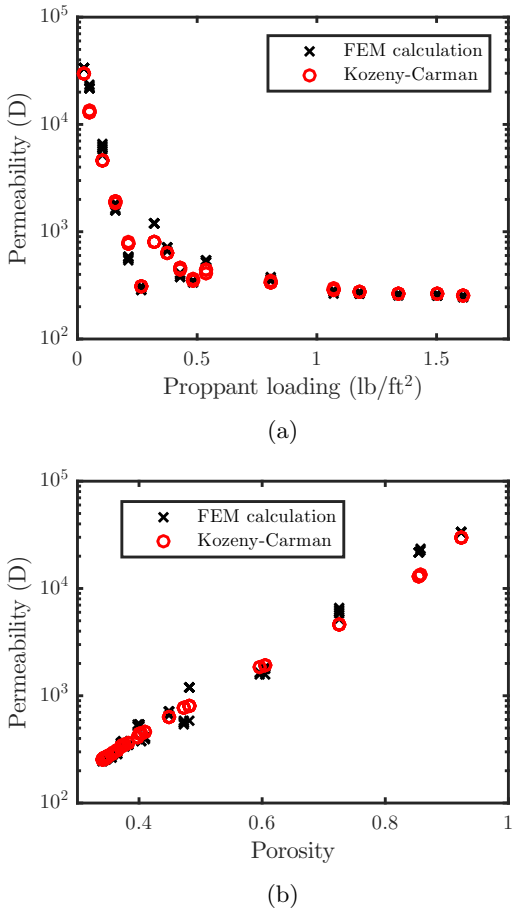

Figure 9: Comparison of FEM results to Kozeny-Carman prediction of permeability.

the strong agreement with the Kozeny-Carman relation for homogeneous packings (9), the numerical accuracy of the FEM permeability calculations is deemed to be adequate. We have therefore selected a mesh size of ∼0.2 mm for all cases, as this strikes a good balance between accuracy and computational cost. Even with this relatively modest mesh size, larger systems such as the one in figure 7 contain upwards of 30 million elements; considering that for each proppant loading there are five structures to be computed (corresponding to five different initial conditions), the FEM calculations still represent a substantial computational effort.

In figure 8, we plot the permeability and fracture conductivity as a function of proppant loading for all the structures discussed above. The permeability follows the same trends as the porosity (see figure 5) across the entire proppant loading range. This is expected, since the particle packing is random, in the sense that there is no mechanism to yield long-range correlated flow paths beyond the interparticle packing (we will return to this point when discussing heterogeneous packings shortly). Thus, permeability in these systems is primarily a function of porosity, and increases dramatically as large flow paths become available in highly depleted partial monolayers. At high proppant loadings, corresponding to multi-layer homogeneous structures, there is a slight decrease in permeability with proppant density. As in the case of porosity, this is a result of the higher interstitial space near the fracture walls, the influence of which diminishes with increasing fracture aperture. The values of permeability and conductivity in figure 8 at higher loadings are well within the range of values typically seen in laboratory and field experiments with conventional fracturing techniques [9].

Given the relatively homogeneous placing of the proppant particles, we compare the FEM results to predictions using the Kozeny-Carman equation for the entire range of proppant loading. In the present case, the Kozeny-Carman equation predicts the permeability κ_{KC} as:

$$\kappa_{KC} = \frac{\phi_S^2 D_P^2}{180} \frac{\epsilon^3}{(1-\epsilon)^2} \tag{6}$$

Here, ϕ_s is the sphericity of the particles, set to unity; D_p is the particle diameter, set to the mean value of 1.0 mm, and ϵ is the porosity. Results are plotted as a function of proppant loading and porosity in figure 9. The match between the FEM solution and the Kozeny-Carman relation is very good, with the exception of the lowest proppant density values. In this regime, the high degree of heterogeneity in the particle placement, as well as the larger overlap between the proppant particles and the fracture walls are inconsistent with the assumptions of the Kozeny-Carman equation, so the disagreement is not surprising.

To increase well productivity, it is desirable to increase fracture conductivity. As shown in figures 8 and 9, the highest conductivities by two orders of magnitude are found in high-porosity partial monolayers, at very low proppant densities. However, figure 6 clearly shows that these structures are also far more prone to failure, since the fraction of

particles that experience forces larger than the side crushing strength is high (i.e. large x_P). As such, the large conductivities of partial monolayer structures would likely be completely lost because of proppant failure and fracture closure, which our compression simulations do not account for. However, it may be possible [7] under certain circumstances (e.g. high-strength proppant/hard surrounding formation) to enhance fracture conductivity by employing similar proppant structures, although likely to a much lesser extent than the more extreme cases shown here. The primary challenge to using partial monolayer structures is therefore maintaining the mechanical integrity of the fracture - i.e. avoiding proppant crushing, embedment or spalling that could lead to fracture closure.

The conventional approach to enhancing fracture conductivity, i.e. increasing fracture aperture, is also quantitatively captured by the models. At higher proppant loadings in figure 8, the permeability decreases slightly and approaches a constant value. The same trend is seen in the porosity (figure 5). Therefore the only way to increase conductivity beyond this plateau value is to increase the fracture aperture. The linear increase in conductivity (figure 8) with proppant loading and fracture aperture reflects this expected behavior (recall that conductivity is simply the product of permeability and fracture aperture). The mechanical stability of fractures in this range is quite good, as shown by relatively low x_P values (see figure 6); there is even a slight decrease in x_P with increasing fracture aperture, but this effect is expected to saturate, as discussed previously. Increasing fracture aperture in the context of multi-layered homogeneous proppant structures appears to be a straightforward strategy to enhance fracture conductivity. However, this usually entails high pumping pressure and large amounts of proppant, both of which are costly and clearly cannot reach arbitrarily high fracture apertures.

3.2. Heterogeneous proppant packs

Motivated by the limitations of conventional proppant placement discussed above, several alternative proppant injection strategies have been developed. This section addresses a variety of heterogeneous proppant pack structures, which capture the key features of proppant packs believed to be formed by channel fracturing [8] and related techniques. These injection techniques have been discussed in the introduction, and the nature of the structures was briefly described in section 2.1 (see also figure 1c and d). In field conditions, the downhole proppant structures are largely unknown. Large-scale laboratory-scale experiments aimed at elucidating channel fracturing mechanisms [9] reveal pillar structures that are qualitatively similar to our computer-generated proppant packs, but consisting of much larger and more irregularly-shaped pillars and void spaces. The large number of particles involved in such structures is computationally prohibitive, which is another reason we use simplified models.

As with the compression protocol described for homogeneous structures above, the preparation of these more complex structures in our simulations is artificial and has little bearing to the underlying proppant injection process. We generate two types of heterogeneous proppant packings, which we refer to as pillar and finger structures (following the experimental literature [8, 11]). The distinction is not physically meaningful here, but only made for purposes of artificially generating a larger variety of proppant structures by different means. In both cases, heterogeneous proppant structures are formed by removing particles in a specific pattern from the final compressed states of homogeneous particle packs, and compressing again until the desired confining pressure of 5000 psi is reached. In the case of pillar structures, removal of particles takes place as follows: first, a two-dimensional random packing of polydisperse discs with mean radius R_p are overlayed on the homogeneous structure, parallel to the plane of the fracture. Any proppant particles with coordinates projected to the plane of the discs that are not located within $f_p R_p$ of the centers of discs are then removed, where f_p is a dimensionless factor. The parameters R_p and f_p therefore control the initial (pre-compression) size of the pillars and the separation between them. For each set of R_p and f_p values, we use homogeneous initial packings corresponding to three different proppant loadings. Finger structures are prepared as follows: starting with homogeneous compressed particle packs, a disc of radius R_f performs a random walk in the x (flow) direction along the pack. The random walk starts and ends at points randomly selected in the plane of the fracture. The process is repeated n_f times, and any particles that are have not been contacted by any of the random walks are then removed. The parameter R_f therefore controls the effective thickness of the proppant fingers, whereas the parameter n_f controls the density (and hence separation) of the fingers. Several examples of both pillar and finger structures generated in this manner are shown in figure 10.

The parameter space required to fully describe heterogeneous proppant packs such as those in figure 10 is prohibitively large - for instance, proppant pillars can have a large variety of sizes, shapes, relative orientations and separations, each of which requires a set (and distribution) of non-trivial geometric parameters. Even with the simple models that we use to construct these packings, variations in parameters such as R_f, R_P, f_P, n_f (see above for definitions), and the need for multiple realizations for each set, quickly leads to an intractably large parameter space. We therefore analyze only a limited sample of the many possible realizations of heterogeneous packings and discuss results with respect to simple measures such as net proppant loading. This also makes a comparison to the homogeneous proppant packs more straightforward. For the purposes of this analysis, we also group pillar and finger structures together, as there is no clear physical basis for treating them as separate structures.

Figures 11 to 13 show the key properties of a large va-

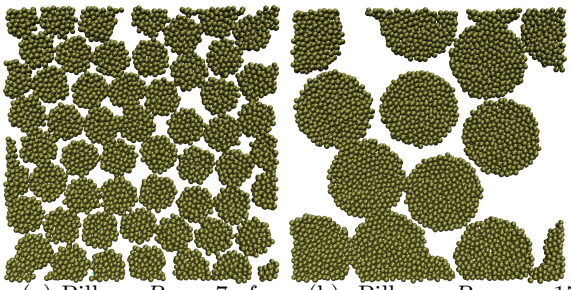

(a) Pillars, $R_P = 7$, $f_P = 1.1$

(b) Pillars, $R_P = 15$, $f_P = 1.1$

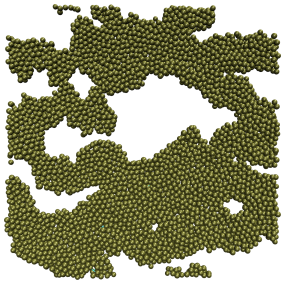

(c) Fingers, $R_f = 4$, $n_f = 6$

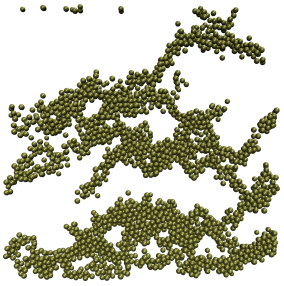

(d) Fingers, $R_f = 1$, $n_f = 9$

Figure 10: Examples of computationally generated heterogeneous proppant pack structures. See text for explanation of parameters.

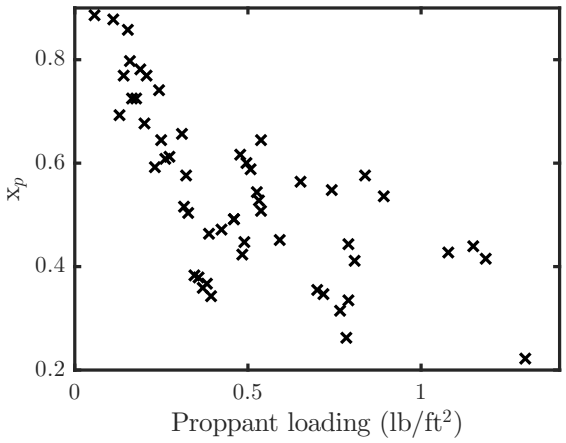

Figure 12: Fraction of particles x_P likely to yield as a function of proppant loading for all heterogeneous proppant structures. x_P is defined as the fraction of particles with $F_{\mathrm{N,max}}(r/r_0)^2 > \mathrm{SCS}_0$.

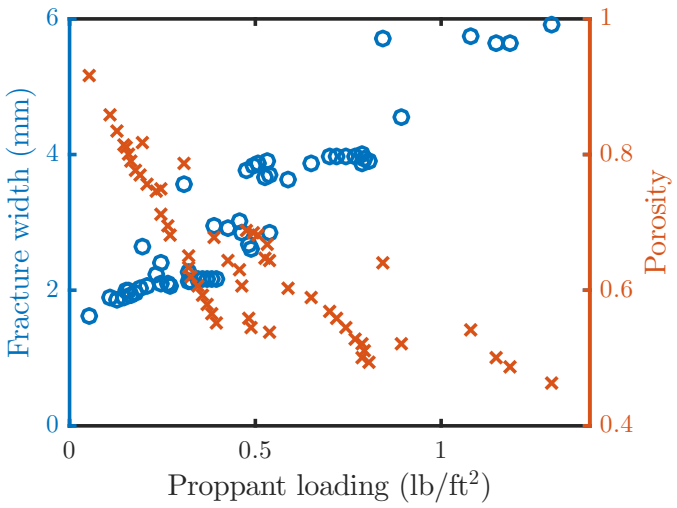

Figure 11: Width and porosity as a function of proppant loading for all heterogeneous proppant packs tested

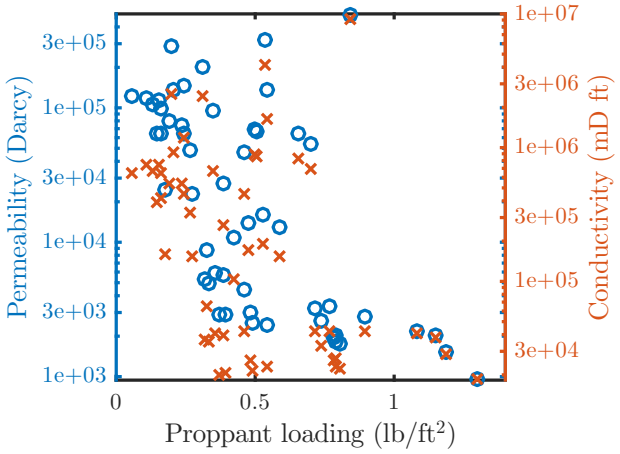

Figure 13: Permeability (left axis) and conductivity (right axis) for all heterogeneous proppant pack structures.

riety of heterogeneous proppant structures. Higher proppant loading naturally leads to larger fracture apertures and lower porosity (figure 11), but there is significantly more variability in both quantities due to the heterogeneity of proppant placement. Relatively high porosity (> 0.6) can be attained even for moderate proppant loadings (compare to figure 5). Conversely, these higher porosity structures have lower mechanical stability as indicated by larger values of x_P in figure 12. This is simply a result of fewer particles in segregated regions supporting the same confining pressure, which leads to some particles experiencing larger stresses than in homogeneous close-packed structures. As expected, increased proppant loading generally leads to better mechanical stability (lower x_P), but once again there is significant variability as compared to the homogeneous case. Finally, the fracture permeability and conductivity are plotted as a function of proppant loading for all heterogeneous proppant packs in figure 13. Due to the large number of open flow channels in these systems, the conductivity is in many cases several orders of magnitude larger than in the homogeneous case for comparable proppant loadings.

It therefore appears that heterogeneous proppant structures offer significantly higher conductivity at the cost of mechanical stability. To make a direct comparison to homogeneous packs, we plot computed fracture conductivities as a function of x_p in figure 14. This effectively represents a performance envelope for proppant structures in the context of the current analysis. The ideal regime is as far in the top left region as possible (low x_p and high conductivity), and the poorest performance corresponds to the bottom right of the plot (both high x_p and low conductivity). Clearly, homogeneous proppant packs offer the best mechanical stability, in particular the cluster of points near $x_p \sim 0.2$, conductivity $< 10^4$. These correspond to multi-layer close-packed structures (e.g. see figure 1a), where relatively modest gains in conductivity can be made primarily by increasing the fracture aperture (see figure 8 and associated discussion). As discussed earlier, the more drastic increases in conductivity of homogeneous proppant packs can be seen with the onset of partial monolayer structures at very low proppant loadings. However, this comes at a significant cost of mechanical stability, indicated by higher x_p values. The small cluster of points near $x_p \sim -0.8$, conductivity $\sim 10^3$ correspond to the intermediate regimes between the formation of single and multi-layered structures which were discussed earlier. Since these are associated with shortcomings of the artificial method we use to construct proppant packs, we will not dwell on them any further.

While heterogeneous proppant packs lack the mechanical stability of multi-layered homogeneous close-packed structures, they offer drastic gains in fracture conductivities, which in many cases are far greater than conductivity gains associated with partial monolayers. In light of the logarithmic scale of the conductivity axis in figure 14, a seemingly small vertical separation in the plot

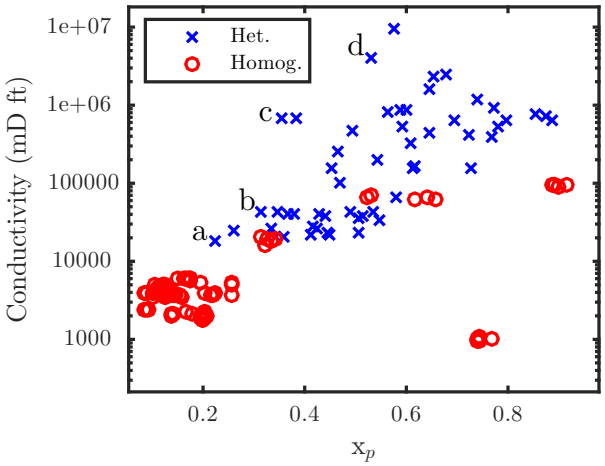

Figure 14: Conductivity as a function of x_p for both homogeneous and heterogeneous proppant pack structures.

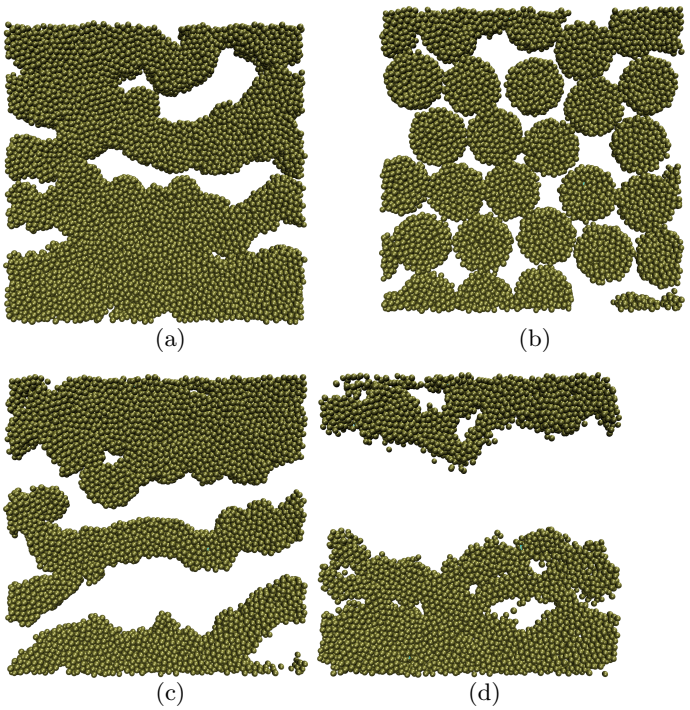

Figure 15: Select heterogeneous proppant pack structures, with subfigures corresponding to points labeled in figure 14. Flow direction is horizontal in all cases.

translates to substantial differences in conductivity. Furthermore, the cost in terms of mechanical stability (i.e. the increase in x_p) for heterogeneous structures is in many cases smaller than that associated with partial monolayers. Several structures that have desirable properties are identified in figure 14 (points marked a-d) and depicted in figure 15. The common feature of these structures is the presence of open flow paths that percolate in the flow direction. Additionally, large, multi-layered pillars/islands of proppant particles are found in all of these structures, which suggests that these structures are optimal for minimizing per-particle stress and hence improving overall mechanical stability. Open flow paths in these cases (especially structures a-c) may be partially due to the relatively small size of the computational domain; however, the key features just noted (percolating flow paths, large aggregates of proppant particles) resemble those found in laboratory-scale tests [8] and are likely responsible for the large conductivities observed in field conditions.

3.3. Flow simulations based on imaging of a laboratory-scale proppant-filled fracture

The artificial nature of our proppant structure generation protocol behooves us to compare the resulting structures to experimental data as closely as possible. Micro-CT data were obtained for a manually fractured shale specimen as described in section 2.4. The resulting images were processed to generate an FEM mesh analogous to that used for computer-generated structures. First, the fracture volume was isolated from the CT data using a combination of adaptive thresholding and edge detection image processing steps. Within the fracture volume, individual proppant particles were then segmented using a three-dimensional watershed algorithm. All image processing steps were carried out using various features of the open-source tools OpenCV [37], scikit-image [38] and SciPy [39]. The geometry of the entire fracture volume was converted from a voxel-based representation to a more convenient CAD-based representation in a manner similar to the construction of computer-generated fracture geometries: a series of spline curves were first created along the top and bottom of the voxel region corresponding to the fracture space. These splines were then connected to create net surfaces corresponding to the two fracture surfaces, which were then swept towards each other in a direction normal to the fracture plane to create the solid volume. Due to the relatively low resolution of the micro-CT images compared to the proppant particle size, the edges of particles could not be well resolved. As such, we replaced individual particle regions identified from the images with spheres of equivalent volumes placed at the centers of these regions. A uniform tetrahedral mesh was generated for the fracture volume, and spheres corresponding to proppant particles were then used as input to the CDFEM algorithm to create mesh surfaces corresponding to the particle-fluid interfaces. The resulting mesh was then used to compute

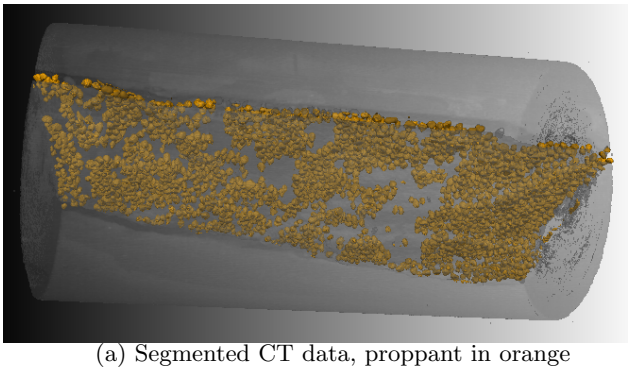

(a) Segmented CT data, proppant in orange

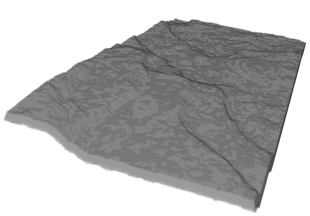

(b) Voxel-based representation of fracture volume

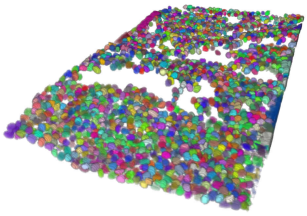

(c) Segmented individual particles

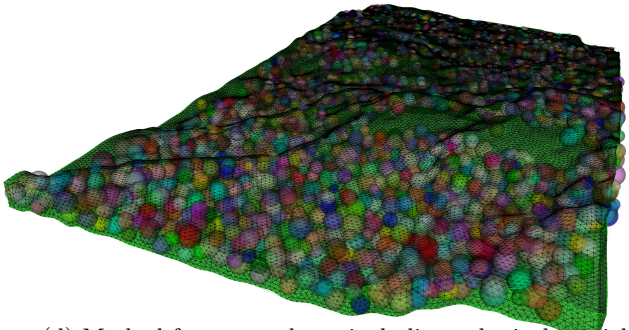

(d) Meshed fracture volume including spherical particles

Figure 16: Key steps in image processing of micro-CT data to obtain a mesh of the propped fracture geometry

permeability from FEM flow simulations as described earlier (section 2.3). Figure 16 depicts the process of generating a mesh from the micro-CT image data and the resulting geometry.

The proppant loading and porosity as computed from the solid model are 0.147 lb/ft^2 and 0.561, respectively. These values correspond to a typical partial monolayer in the case of the computer-generated homogeneous packs: see figure 5, where the closest point is a partial monolayer with a proppant loading of 0.161 lb/ft^2 and a mean porosity averaged over five initial conditions of 0.60. This is also consistent with the visual representation of the particle phase in figures 16c and d, which clearly show a partial monolayer. Furthermore, the computed conductivity values for the CT-based structure (1600 Darcy and 4580 mD ft at the smallest mesh size tested) are also similar to those obtained for the computer-generated structure (1680 Darcy and 5440 mD ft, averaged over five different initial conditions).

4. Conclusions

The computer-generated proppant-filled fractures presented in this work span a broad range of commonly known structures. They include typical homogeneous multi-layer close packings of spherical proppant particles, as well as more exotic hypothesized structures such as partial monolayers and highly heterogeneous structures resulting from novel channel fracturing techniques [8]. The homogeneous proppant packings range from partial monolayers to multi-layered close packings as the proppant loading is increased. We have quantified the porosity, fracture aperture, stress state (as measured by the fraction of particles likely to yield), permeability and fracture conductivity for a wide range of proppant loadings in each type of structure. The partial monolayer structures exhibit high conductivities ($> 10,000$ mD ft in some cases) due to their high porosity and the presence of open flow channels, but this comes at a cost of unstable packs. This suggests that these structures are impractical except perhaps in cases of extremely high-strength proppants in very hard formations. At relatively high proppant loadings, we observe conventional multi-layered close-packed structures, which have moderate conductivities ($\sim$ 5000 mD ft) and exhibit relatively low stresses. This is consistent with the pervasiveness of such structures in field operations; however, the only way to increase the conductivity of these fractures is to increase the fracture aperture, which requires higher pumping pressures and larger volumes of proppant and suspending fluid, all of which increase cost. The resulting increase in fracture conductivity is shown here to be relatively modest, since the permeability remains nearly constant (or even decreases slightly) with increased proppant loading, and the conductivity gains from increasing fracture aperture are only linear.

Recently developed proppant injection strategies such as channel fracturing [8, 9] aim to overcome the limitations of homogeneous packings by placing proppant in discrete, well-separated structures. While the exact proppant structures resulting from channel fracturing have not been characterized, we have generated a wide range of structures that capture many of the key features of those hypothesized to form in field operations and observed in laboratory-scale experiments [9]. We have carried out the same analyses for these structures as for the homogeneous packs, and have indeed found that in nearly all cases there is a drastic gain in fracture conductivity due to the formation of large open channels ($10^5 - 10^7$ mD ft in some cases, see figure 13). High conductivity persists even at relatively low proppant loadings and small fracture apertures, which suggests an additional benefit in minimizing pumping pressure and proppant volumes. However, due to the highly porous nature of these structures, the stress state is also notably higher than in conventional packings. Overall, our results suggest that heterogeneous structures that offer percolating flow channels throughout the proppant pack can provide drastic improvements in conductivity, which in some select cases comes at only a moderate cost in proppant pack stability. As such, depending on the application (i.e. pressure and mechanical properties of the formation), certain heterogeneous structures may be ideal. However, they may require stronger proppant and sophisticated injection techniques to achieve particular structural features that provide both ample flow paths and adequate mechanical stability (e.g. see figure 15).

Although our simulations make many simplifying assumptions regarding the proppant placement process, they offer a detailed and quantitative comparison among several classes of proppant structures that are important in the hydraulic fracturing literature as well as in field operations. We have verified that our computer-generated proppant structures are realistic by comparing them to micro-CT data of a manually fractured and propped shale sample. The analysis here has identified several features of proppant packs that govern the balance between structures with relatively low porosity and high mechanical strength, which mitigate proppant yield and fracture closure; and heterogeneous packings with ample flow paths, which improve permeability but are more prone to proppant failure. It is hoped that this work will motivate fundamental studies of particle packing in the context of hydraulic fracturing, in particular detailed experimental characterization of well-controlled proppant packings.

Acknowledgements

This work was supported by the Sandia Laboratory Directed Research and Development Program. The authors would like to thank Lisa Mondy for her support in obtaining funding, and in the first year of the project. Sandia National Laboratories is a multiprogram laboratory managed and operated by Sandia Corporation, a Lockheed-Martin Company, for the U. S. Department of Energy's National Nuclear Security Administration under Contract No. DE-AC04-94AL85000.

References

[1] L. Kern, T. Perkins, R. Wyant, *et al.*, "Propping fractures with aluminum particles," *Journal of Petroleum Technology*, vol. 13, no. 06, pp. 583–589, 1961.

[2] J. W. Graham, "Hydraulic fracturing using reinforced resin pellets," May 2 1972. US Patent 3,659,651.

[3] C. E. Cooke *et al.*, "Fracturing with a high-strength proppant," *Journal of Petroleum Technology*, vol. 29, no. 10, pp. 1–222, 1977.

[4] J. J. Fitzgibbon, "Sintered spherical pellets containing clay as a major component useful for gas and oil well proppants," Jan. 24 1984. US Patent 4,427,068.

[5] G. A. McDaniel, J. Abbott, F. A. Mueller, A. M. Anwar, S. Pavlova, O. Nevvonen, T. Parias, J. Alary, *et al.*, "Changing the shape of fracturing: new proppant improves fracture conductivity," in *SPE Annual Technical Conference and Exhibition*, Society of Petroleum Engineers, 2010.

[6] J. Huitt and S. Darin, "Effect of a partial monolayer of propping agent on fracture flow capacity," *Trans., AIME*, vol. 219, p. 31, 1960.

[7] H. D. Brannon, M. R. Malone, A. R. Rickards, W. D. Wood, J. R. Edgeman, J. L. Bryant, *et al.*, "Maximizing fracture conductivity with proppant partial monolayers: theoretical curiosity or highly productive reality?," in *SPE Annual Technical Conference and Exhibition*, Society of Petroleum Engineers, 2004.

[8] M. R. Gillard, O. O. Medvedev, P. R. Hosein, A. Medvedev, F. Peñacorada, E. d'Huteau, *et al.*, "A new approach to generating fracture conductivity," in *SPE Annual Technical Conference and Exhibition*, Society of Petroleum Engineers, 2010.

[9] A. V. Medvedev, C. C. Kraemer, A. A. Pena, M. K. R. Panga, *et al.*, "On the mechanisms of channel fracturing," in *SPE Hydraulic Fracturing Technology Conference*, Society of Petroleum Engineers, 2013.

[10] J. Morris, N. Chugunov, G. Meouchy, *et al.*, "Understanding heterogeneously propped hydraulic fractures through combined fluid mechanics, geomechanics, and statistical analysis," in *48th US Rock Mechanics/Geomechanics Symposium*, American Rock Mechanics Association, 2014.

[11] Y. Liu, P. B. Gadde, M. M. Sharma, *et al.*, "Proppant placement using reverse-hybrid fracs," *SPE Production & Operations*, vol. 22, no. 03, pp. 348–356, 2007.

[12] B. Cook, M. Lee, A. DiGiovanni, D. Bronowski, E. Perkins, and J. Williams, "Discrete element modeling applied to laboratory simulation of near-wellbore mechanics," *International Journal of Geomechanics*, vol. 4, no. 1, pp. 19–27, 2004.

[13] B. Damjanac, I. Gil, M. Pierce, M. Sanchez, A. Van As, J. McLennan, *et al.*, "A new approach to hydraulic fracturing modeling in naturally fractured reservoirs," in *44th US Rock Mechanics Symposium and 5th US-Canada Rock Mechanics Symposium*, American Rock Mechanics Association, 2010.

[14] H. Shimizu, S. Murata, and T. Ishida, "The distinct element analysis for hydraulic fracturing in hard rock considering fluid viscosity and particle size distribution," *International Journal of Rock Mechanics and Mining Sciences*, vol. 48, no. 5, pp. 712–727, 2011.

[15] S. Deng, H. Li, G. Ma, H. Huang, and X. Li, "Simulation of shale–proppant interaction in hydraulic fracturing by the discrete element method," *International Journal of Rock Mechanics and Mining Sciences*, vol. 70, pp. 219–228, 2014.

[16] A. Khanna, A. Kotousov, J. Sobey, and P. Weller, "Conductivity of narrow fractures filled with a proppant monolayer," *Journal of Petroleum Science and Engineering*, vol. 100, pp. 9–13, 2012.

[17] K. E. Thompson, "Computing particle surface areas and contact areas from three-dimensional tomography data of particulate materials," *Particle & Particle Systems Characterization*, vol. 24, no. 6, pp. 440–452, 2007.

[18] K. E. Thompson, C. S. Willson, C. D. White, S. Nyman, J. P. Bhattacharya, and A. H. Reed, "Application of a new grain-based reconstruction algorithm to microtomography images for quantitative characterization and flow modeling," tech. rep., DTIC Document, 2008.

[19] P. Bhattad, C. Willson, and K. Thompson, "Segmentation of low-contrast three-phase x-ray computed tomography images of porous media," *Advances in Computed Tomography for Geomaterials: GeoX 2010*, pp. 254–261, 2010.

[20] N. Lane and K. Thompson, "Image-based pore-scale modeling using the finite element method," *Advances in Computed Tomography for Geomaterials: GeoX 2010*, pp. 295–303, 2010.

[21] P. Sanematsu, Y. Shen, K. Thompson, T. Yu, Y. Wang, D.-L. Chang, B. Alramahi, A. Takbiri-Borujeni, M. Tyagi, and C. Willson, "Image-based stokes flow modeling in bulk proppant packs and propped fractures under high loading stresses," *Journal of Petroleum Science and Engineering*, vol. 135, pp. 391–402, 2015.

[22] A. T. Borujeni, M. Tyagi, C. D. White, *et al.*, "Effects of stress-dependent hydraulic properties of proppant packs on the productivity indices of the hydraulically fractured gas reservoirs," in *SPE/AAPG/SEG Unconventional Resources Technology Conference*, Society of Petroleum Engineers, 2014.

[23] P. A. Cundall and O. D. Strack, "A discrete numerical model for granular assemblies," *Geotechnique*, vol. 29, no. 1, pp. 47–65, 1979.

[24] X. Garcia, J.-P. Latham, J. Xiang, and J. Harrison, "A clustered overlapping sphere algorithm to represent real particles in discrete element modelling," *Geotechnique*, vol. 59, no. 9, pp. 779–784, 2009.

[25] L. E. Silbert, D. Ertaş, G. S. Grest, T. C. Halsey, D. Levine, and S. J. Plimpton, "Granular flow down an inclined plane: Bagnold scaling and rheology," *Physical Review E*, vol. 64, no. 5, p. 051302, 2001.

[26] K. Johnson, K. Kendall, and A. Roberts, "Surface energy and the contact of elastic solids," *Proceedings of the Royal Society of London A: Mathematical, Physical and Engineering Sciences*, vol. 324, pp. 301–313, 1971.

[27] J. Ai, J.-F. Chen, J. M. Rotter, and J. Y. Ooi, "Assessment of rolling resistance models in discrete element simulations," *Powder Technology*, vol. 206, no. 3, pp. 269–282, 2011.

[28] C. Kloss, C. Goniva, A. Hager, S. Amberger, and S. Pirker, "Models, algorithms and validation for opensource dem and cfd–dem," *Progress in Computational Fluid Dynamics, an International Journal*, vol. 12, no. 2-3, pp. 140–152, 2012.

[29] T. D. Blacker, W. J. Bohnhoff, and T. L. Edwards, "Cubit mesh generation environment. volume 1: Users manual," tech. rep., Sandia National Labs., Albuquerque, NM (United States), 1994.

[30] K. L. Johnson and K. L. Johnson, *Contact mechanics*. Cambridge university press, 1987.

[31] C. Ouwerkerk, "A micro-mechanical connection between the single-particle strength and the bulk strength of random packings of spherical particles," *Powder Technology*, vol. 65, no. 1, pp. 125–138, 1991.

[32] J. Jaeger, "Failure of rocks under tensile conditions," *International Journal of Rock Mechanics and Mining Sciences*, vol. 4, no. 2, pp. 219–227, 1967.

[33] D. R. Noble, E. P. Newren, and J. B. Lechman, "A conformal decomposition finite element method for modeling stationary fluid interface problems," *International Journal for Numerical Methods in Fluids*, vol. 63, no. 6, pp. 725–742, 2010.

[34] J. B. Lechman, M. B. Nemer, and D. R. Noble, "Toward application of conformal decomposition finite elements to non-colloidal particle suspensions," *International Journal for Numerical Methods in Fluids*, vol. 68, no. 11, pp. 1409–1421, 2012.

[35] P. B. Bochev, C. R. Dohrmann, and M. D. Gunzburger, "Stabilization of low-order mixed finite elements for the Stokes equations," *SIAM Journal on Numerical Analysis*, vol. 44, no. 1, pp. 82–101, 2006.

[36] M. Ingraham, S. Bauer, E. Quintana, D. Bolintineau, R. Rao, J. Lechman, *et al.*, "Proppant and host rock deformation in fractured shale flow through experiments," in *49th US Rock Mechanics/Geomechanics Symposium*, American Rock Mechanics Association, 2015.

[37] G. Bradski, "OpenCV image processing library," *Dr. Dobb's Journal of Software Tools*, 2000.

[38] S. van der Walt, J. L. Schönberger, J. Nunez-Iglesias, F. Boulogne, J. D. Warner, N. Yager, E. Gouillart, T. Yu, and the scikit-image contributors, "scikit-image: image processing in Python," *PeerJ*, vol. 2, p. e453, 6 2014.

[39] E. Jones, T. Oliphant, P. Peterson, *et al.*, "SciPy: Open source scientific tools for Python," 2001–. [Online; accessed 2016-03-10].

DISTRIBUTION

1	MS0359	D. Chavez, LDRD Office	1911 (electronic copy)
1	MS0555	E. Quintana	1529 (electronic copy)
1	MS0735	E. Webb	6910 (electronic copy)
1	MS0735	M. Lee	6914 (electronic copy)
1	MS0836	J. Lechman	1516 (electronic copy)
1	MS0836	R. Rao	1516 (electronic copy)
1	MS1033	M. Ingraham	6914 (electronic copy)
1	MS1033	S. Bauer	6914 (electronic copy)
1	MS1314	D. Bolintineanu	1516 (electronic copy)
1	MS0899	Technical Library	9536 (electronic copy)


Sandia National Laboratories